ORIENTATION AND ROTATIONAL DIFFUSION OF FIBERS IN SEMIDILUTE SUSPENSION

A Thesis
Presented to
The Academic Faculty

by

Asif Salahuddin

In Partial Fulfillment
of the Requirements for the Degree
Doctor of Philosophy in the
George W. Woodruff School of Mechanical Engineering

Georgia Institute of Technology
August 2011

ORIENTATION AND ROTATIONAL DIFFUSION OF FIBERS IN SEMIDILUTE SUSPENSION

Approved by:

Dr. Cyrus Aidun, Advisor
George W. Woodruff School of
Mechanical Engineering
Georgia Institute of Technology

Dr. Victor Breedveld
School of Chemical and Biomolecular
Engineering
Georgia Institute of Technology

Dr. S. Mostafa Ghiaasiaan
George W. Woodruff School of
Mechanical Engineering
Georgia Institute of Technology

Dr. Richard F. Salant
George W. Woodruff School of
Mechanical Engineering
Georgia Institute of Technology

Dr. Richard Vuduc
Computational Science and
Engineering
Georgia Institute of Technology

Date Approved: May 31 2011

To

Ma and Baba

ACKNOWLEDGEMENTS

I would like to express my gratitude to my PhD advisor, Prof. Cyrus Aidun, for his instrumental role in my scholarly development. His continuous encouragement shaped up my trajectory in this field of research. I am grateful to my committee members as well. I ended up with the best possible final product as a result of my committee's helpful advice. My excellent colleagues at Georgia Tech have always provided the right academic atmosphere, where intellectual growth is admired. My thanks specially go to Dr. Jingshu Wu, my former colleague in Prof. Aidun's group, for sharing his valuable experiences in code development with lattice–Boltzmann method. I am indebted to the Institute of Paper Science and Technology (IPST) for granting me the Paper Science and Technology Fellowship. I would also like to thank the National Science Foundation's support through TeraGrid grant to our research group which provided computing resources for this research. I appreciate the help of my committee member Prof. Vuduc, who granted me additional computing resources in School of CS&E.

I must remember my parents for being patient, and keeping faith in me; and not least, I am grateful to my wife, whose steadfastness during the last few years provided a day to day structure upon which such a prolonged effort could be made. And my little bundle of joy, my daughter, how could I see the light at the end of the tunnel, if it were not coming from your eyes?

TABLE OF CONTENTS

LIST OF TABLES

LIST OF FIGURES

LIST OF SYMBOLS OR ABBREVIATIONS

$\mathcal{A}$	Sixth-order orientation moment
$\mathbb{A}$	Fourth-order orientation moment
$\mathbf{A}$	Second-order orientation moment
$\dot{\mathbf{A}}$	Material derivative of $\mathbf{A}$
a	Radius of fiber
ARD	Anisotropic Rotational Diffusivity
AWDM	Anisotropic Weak Rotational Diffusivity Model
C	3-Dim. spatial rotational diffusivity tensor
C	Orbit Constant unbounded (between 0 to ∞)
C_b	Orbit Constant within finite bound (between 0 to 1)
$\langle C_b \rangle$	Ensemble average of orbit constant
C_I	Folgar–Tucker constant (Scalar interaction coefficient)
CR	Contraction ratio
c_s	Pseudo speed of sound
c_v	Solid volume fraction
d	Diameter of fiber
$\mathbf{D}^r$	2-Dim. surface rotational diffusivity tensor (defined on the unit sphere)
$\mathbf{E}$	Strain rate tensor
EBF	External Boundary Force
$\mathbf{e}_k$	Discrete velocity vector for LBM
$\hat{\mathbf{e}}_1$	Unit vector on flow (x) direction
$\hat{\mathbf{e}}_2$	Unit vector on velocity gradient (y) direction
$\hat{\mathbf{e}}_3$	Unit vector in vorticity (z) direction
$\mathbf{F}^{con}$	Contact force

$\mathbf{F}^{ele}$	Electrical force
$\mathbf{F}^{fsi}$	Force per unit volume acting on solid
$\mathbf{F}^{gra}$	Gravitational force
$\mathbf{F}_i$	Total force on ith fiber
$\mathbf{F}^{lub}$	Lubrication force
f_k	Distribution function of LBM
f_k^{eq}	Equilibrium distribution function of LBM
$\boldsymbol{g}$	Force per unit volume acting on fluid
h_{in}	Inlet height of the contracting section of converging–diverging channel
h_o	Throat height of the converging–diverging channel
$\mathbf{I}$	Identity tensor
$\boldsymbol{\mathcal{I}}_i$	Inertial tensor of the ith fiber
k_B	Boltzmann's constant
L	Length of fiber
$\mathcal{L}$	Velocity gradient tensor
LBM	Lattice Boltzmann Method
L_c	Length of the contracting section of the converging–diverging channel
LFT	Long Fiber Thermoplastic
M_i	Mass of the ith fiber
MPI	Message Passing Interface
n	Number of fibers per unit volume (Number density)
N_1^B	First normal stress difference with Batchelor's theory
N_2^B	Second normal stress difference with Batchelor's theory
N_1^*	First normal stress difference with LBM–EBF simulation (direct computation)
N_2^*	Second normal stress difference with LBM–EBF simulation (direct computation)
$\mathcal{O}(\ )$	Order of
OpenMP	Open Multi-Processing

$\mathbf{p}$	Unit vector along the fiber axis
$p\left(C_b\right)$	Differential orbit constant distribution function
Pe	Peclet number
$\dot{\mathbf{p}}^h$	Drift velocity of fiber
$\dot{\mathbf{p}}^J$	Rotation rate of fiber with Jeffery's solution
P_L	Intensity of concentration variations
$\bar{P}_L$	Average Intensity of concentration variations
$p\left(\phi\right)$	Differential ϕ distribution function
$\mathbf{q}^d$	Diffusive flux vector
$Q(\epsilon)$	Correction factor for finite aspect-ratio fiber
R	Diffusivity ratio
r_e	Equivalent aspect-ratio of fiber
Re	Macroscopic Reynolds number
Re_p	Particle Reynolds number
$\mathbf{r}_{im}$	Position vector of hinge m in fiber i
$\mathbf{r}_{jk}$	Position vector of hinge k in fiber j
r_p	Aspect-ratio of fiber
SFT	Short Fiber Thermoplastic
T	Orbit period
$\mathtt{T}$	Transpose operator
$\mathcal{T}$	Absolute temperature in degrees Kelvin
t	Time
$\mathbf{t}$	Projection tensor
$\mathbf{T}_i$	Total torque of the ith fiber
$\mathbf{u}$	Fluid velocity
$\mathbf{U}_f$	fluid velocity at fluid–solid boundary
$\mathbf{U}_i$	Velocity of the ith fiber

$\mathbf{V}_{im}$	Velocity of hinge m in fiber i
$\mathbf{V}_{jk}$	Velocity of hinge k in fiber j
$\mathbf{V}^{lub}_{im-jk}$	Relative velocity component for lubrication force calculation
$\mathbf{W}$	Vorticity tensor
w_k	lattice–Boltzmann direction weights
$\boldsymbol{x}$	Position vector
$\boldsymbol{x}^l_{ij}$	Position vector for the jth node on ith fiber
β_1	Empirical constant in the isotropic part of Koch model
β_2	Empirical constant in the anisotropic part of Koch model
Γ	Fluid–solid boundary
γ	Shear strain
$\dot{\gamma}$	Shear rate
δ	Dirac delta function
Δt^{LBM}	Unit timestep of LBM
Δx^{LBM}	Unit grid size of LBM
ϵ	Small positive number in fiber–fiber contact modeling
ε	Knudsen number
θ	Azimuthal angle between fiber axis, and the vorticity (z) axis
λ	Shape factor of fiber
μ_{eff}	Effective viscosity
μ_{fiber}	Dynamic viscosity parameter in Batchelor's theory
μ^B_{rel}	Relative viscosity with Batchelor's theory
μ^*_{rel}	Relative viscosity with LBM–EBF simulation (direct computation)
μ_{sp}	Specific viscosity
ν	Kinematic viscosity
Ξ	Computational domain
Ξ'	Computation subdomain for spatial averaging excluding fibers near the wall

ρ	Density of fluid
$\boldsymbol{\sigma}$	Suspension stress tensor
$\boldsymbol{\sigma}^B$	Suspension stress tensor with Batchelor's theory
τ	lattice–Boltzmann relaxation time
τ_c	Characteristic time scale for relaxation of $C_b(t)$
ϕ	Projection angle of fiber in xy-plane
Ω	Orientation probability distribution function
$\boldsymbol{\omega}$	Angular velocity of a fiber
$\boldsymbol{\omega}_i$	Angular velocity of the ith fiber
∇	Gradient operator in physical space
∇_p	Gradient operator in orientation space
$\langle\cdot\rangle$	Ensemble average

SUMMARY

The dynamics of fiber orientation is of great interest for efforts to predict a suspension's microstructure and its material properties. The primary variables controlling the rigid fiber orientation are recognized to be the number of fibers per unit volume n, the aspect-ratio of the fiber, $r_p \equiv \frac{L}{d}$, (where L and d are the length and diameter of the fiber, respectively) and the hydrodynamics of the processing flow. In a semidilute suspension (where $nL^3 >> 1$, but $nL^2d < 1$) of low Reynolds number, the succession of the hydrodynamic interactions among fibers causes small changes in fibers' orientations. This change in the orientation of one fiber because of the presence of its neighbors can be accounted for with a rotary diffusion process. In this research a fiber–level simulation method is undertaken to advance the current understanding of the rotational diffusion mechanism for non-colloidal, rigid and rod-like fibers suspended in a creeping Newtonian fluid flow. The fiber–level simulation is based on a hybrid approach, in which the lattice–Boltzmann method (LBM) is coupled with the external boundary force (EBF) method. It should be noted that this LBM–EBF method has already been developed and validated [126, 127, 128] for fiber suspension flow, and thus the primary interest of this research is to utilize this computational perspective to answer some outstanding inquiries on the fiber orientation and the complex rotational diffusion process. However, this PhD work suggests a modification to the existing LBM–EBF approach in order to improve the numerical consistency of the method in terms of recovering the exact macroscopic hydrodynamics from the mesoscale.

Unlike some previous fiber–level simulations reported by other research groups, the LBM–EBF simulations correctly predict the orbit constant distribution of fibers

in a sheared semidilute suspension flow. It is seen that the peaks of the orbit constant, C_b-distributions fall within a range of $0.15 < C_b < 0.4$, which is consistent with the experimental results of Stover et al. [115]. An anisotropic, weak rotary diffusion model 'A.W.D.M.' is tested and shown to predict the C_b-distribution very well, but it can not describe the violation of the Stokes flow symmetry in semidilute suspension. The rotational diffusion mechanism is then characterized with an anisotropic rotary diffusion model (Koch model), which has a three dimensional spatial tensor ($\mathbf{C}$) form. A scalar measure of the rotational diffusion, C_I, termed as the scalar Folgar–Tucker constant, or the scalar interaction coefficient, is extracted from the Koch model, $\mathbf{C}$. The study provides substantial numerical evidence that the range of C_I ($0.0038 \sim 0.0165$) obtained by Folgar & Tucker [43] in a semidilute regime is actually overly diffusive, and that the correct magnitude is $\mathcal{O}(10^{-4})$. The study also reveals that C_I increases either with the decrease of r_p (keeping nL^3 constant) or with the increase of nL^3 (keeping r_p constant) in the semidilute regime. This trend is explained by reasoning that the interactions among fibers become more frequent with either of these scenarios mentioned above, consequently increasing the deviations of fibers' orbits from the initial Jeffery's solution [59] and ultimately causing an increase in C_I. This PhD work also branches out to incorporate the Koch model in the second-order evolution equation for $\mathbf{A}$ ($\mathbf{A}$ is a second-order orientation tensor). The solution of the evolution equation with the Koch model demonstrates unphysical behavior in low concentrations. The most plausible explanation for this behavior is attributed to the errors in closure approximation.

The direct LBM–EBF measurement of the rheological properties of sheared semidilute suspension reveals the limitations of the hydrodynamic theory (Batchelor's theory [12] with Shaqfeh & Fredrickson's [104] correction) by accounting for the transmission of stress due to a small but detectable amount of nonhydrodynamic mechanical fiber–fiber interactions present in the semidilute regime. There is an increase in the

relative viscosity of the suspension due to this nonhydrodynamic effect. Similarly a direct measurement of the first normal stress difference proves that the Carter's formula [24] for predicting the first normal stress difference fails in the semidilute regime. But with an increase of volume concentration, Carter's formula becomes more accurate.

While a bulk of the simulations presented in this PhD work are performed in the simple shear flow situation, the investigation is extended to the characterization of the fiber orientation in a complex flow geometry, which has the linearly contracting shape of a paper machine 'headbox'. It is found that the rotational diffusion due to hydrodynamic interactions among fibers is the predominant term over strain rate in the semidilute regime for a low Reynolds number flow and results in a decreasing trend of rotational Peclet number, Pe along the contraction centerline.

CHAPTER I

INTRODUCTION

1.1 Motivation

Control and prediction of the orientation distribution of particulate suspension have significance in many fields of physics, biology and engineering. The particles may be spheres, flakes, fibers or more complicated geometries with characteristics lengths ranging from nanometers to centimeters, and they may be suspended in Newtonian or non-Newtonian fluids. The work presented here focuses on suspension of non-colloidal (non-Brownian) rigid rod-like fibers in a Newtonian fluid.

In many fiber suspension processes, it is necessary to control the microstructure (i.e. the fiber position and orientation). For example, the fiber orientation distribution affects the making of fiber-reinforced thermoplasts and matrix metal composites. Control of the fiber orientation in these products can yield low cost and high performance in industrial and aerospace applications. Fibers in the shell layer of a molding cavity experience high shear strain where simple shear flow is observed. The predictions of fiber orientation in simple shear flow is very important in that respect. The physical properties of polymer composites, such as elastic modulus, strength, thermal expansion, thermal conductivity, and electrical conductivity, depend on the amount, type, size, and the orientation of the reinforcing fibers. During processing fibers move and rotate with the flow of the polymer matrix, which inevitably changes their orientation state and affects the composite properties.

In paper manufacturing, a homogeneous suspension of wood pulp is desired in a paper machine headbox. A significant amount of paper is used as a substrate for high quality printing. The interactions among the printing plate, ink and substrate

in the printing press can create numerous print quality problems. Variations in the surface pore structure and the surface fiber orientation distribution can cause *print mottle*, a printing defect involving uneven print density across the printed sheet and *gloss mottle*, a point to point difference in gloss. *Curl* is another example of a defect in the final paper product which degrades quality by causing differential dimensional changes between layers in a sheet produced by different moisture expansions from differences in the fiber orientation. These kinds of defects can be minimized and the properties of the final product can be controlled through a proper understanding of the mechanisms which affect the orientation behavior of fibers in suspension. For example, during passage through a paper machine headbox, fibers are aligned by the accelerating flow in the contraction. The degree of fiber alignment affects the strength properties of paper. The alignment in machine direction can be both beneficial and problematic depending on the application — in high-speed printing, the paper requires high tensile strength only in the direction of travel (machine direction) through the printing press, and therefore, high fiber alignment is preferable; whereas, in paper sack production the paper is required to be equally strong in all directions, thus uniform fiber orientation is preferred. The effect of fiber orientation on paper properties, both in the plane of the paper, and in the paper thickness direction, is reviewed by Loewen [74].

Understanding the behavior of fiber suspensions in industrial unit operations is challenging because of the many variables that affect macroscopic properties such as fiber length, concentration, shape, fiber flexibility, fluid–fiber and fiber–fiber interactions. The most common approach to evaluating the physical outcome of the variation of these parameters may be to conduct trials under controlled process conditions using real or pilot scale equipment, and to measure the effects on product structure with the help of various structure characterization techniques. In fact a number of important phenomenological relationships between the process variables

and the product structure have been identified experimentally. But the difficulty of systematically varying the system variables, and the inability of most experimental techniques to provide adequate resolution at the length-scale in question, present limitations to experimental studies.

Although the theoretical literature on fiber suspensions achieved reasonable success in predicting the suspension properties corresponding to a given suspension structure, the mechanisms which control the structure itself are yet to be plainly understood. Over the last few years, direct particle–level numerical simulation techniques (alternatively called 'fiber–level' simulation techniques if the solid phase is composed of discrete fiber shapes) have made promising advances towards understanding the relationship between particle properties and interactions, recreating the microstructures of suspension systems and the underlying particle orientations, and predicting the macroscopic behavior of suspension (Yamamoto & Matsuoka [129]; Yamane et al. [130]; Fan et al. [40], Joung et al. [60]; Sundararajakumar & Koch [117]; Ross & Klingenberg [99], Skjetne et al. [110], Switzer & Klingenberg [119]; Lindström & Uesaka [71]; Aidun et al. [5], MacMeccan et al. [77], Wu & Aidun [126, 127, 128]). In direct particle–level numerical simulation the equations of motion of each particle are solved numerically, subject to the forces and torques identified, and thus the particle's position and orientation evolve in time to produce a prediction of suspension microstructure. Based on their potential to predict the time-dependent and steady-state structures of suspensions, particle–level simulations are emerging to complement the theoretical and the experimental approaches in future research. The method is sufficiently general to include various features such as different particle shapes (elongated and flexible fibers, red blood cells etc.) as well as different forces (hydrodynamic forces, colloidal forces and friction, gravitational and lubrication forces to name a few).

1.2 Scope

The primary purpose of this research is to answer some outstanding questions concerning the dynamic processes controlling fiber orientation in the semidilute suspension of a Newtonian fluid. This thesis presents numerical evidence to characterize a rotational diffusion process in a semidilute suspension of hydrodynamically interacting fibers. The hydrodynamic interactions can give rise to a rotational diffusion mechanism, causing the orientation distribution of fibers to evolve. There are many open questions about the rotational diffusion process and its effect on fiber orientation distribution: should it be isotropic or anisotropic in nature? Is there any model available that can characterize this dynamic process properly? How does this rotational diffusion change with the variation of aspect-ratio of fibers or with the variation of solid volume concentration of the suspension? How do the orientation moments evolve under the influence of an anisotropic rotational diffusion in a simple shear flow? And if a complex flow situation is considered, such as the flow through a paper machine headbox, then what is the interplay between the strain rate and an hydrodynamically induced rotational diffusion along the length of the channel?

Considering these unanswered questions, the fundamental focus of this research is to: (i) understand the dynamics of fiber orientation in in the semidilute suspension, (ii) directly predict orbit distribution of fibers at steady state with numerical simulation, (iii) characterize the rotational diffusion mechanism by the combined use of appropriate models and simulation data in parameter two space ($c_v \times r_p$), (iv) characterize the rotational diffusion in a complex flow situation – flow through a paper machine headbox.

A fiber–level hybrid lattice–Boltzmann method is used in this research to simulate the flow of moderate to large aspect-ratio, rigid, rod-like fibers in the semidilute suspension in Stokes regime. This hybrid method combines Newtonian dynamics for solid particles (fibers) with a lattice–Boltzmann method for the fluid, and the motion

of suspended particles (fibers) is simulated accurately in that way. The steady-state orbit distribution of fibers in semidilute suspension is determined with this simulation. It is to be noted that, the numerically simulated fiber orientation information can be used to test different phenomenological or mechanistic rotational diffusion models proposed in the literature. Commonly, a rotational diffusion model is used with an evolution equation (Fokker-Planck type equation) [43, 2] to predict fiber orientation in suspension. On the contrary, the fiber–level simulation approach used in this research, does not depend on solving an evolution equation to predict the fiber orientation evolution in time. Therefore, this direct numerical method is an ideal tool to characterize the behavior of rotational diffusion process with the combined use of models and the fiber orientation information collected from the simulation; and in turn it can validate the applicability of a previously untested rotational diffusion model in the Fokker-Planck type evolution equation. If proven appropriate, then a rotational diffusion process inside a complex flow geometry can be successfully analyzed with the numerical simulation and a suitable model.

A secondary focus of this research is to study the rheological properties of semidilute suspension with hybrid lattice–Boltzmann simulation as well. The corresponding results using hydrodynamic theories have been judged against those directly measured numerical values and against some available experimental results from literature. The purpose of this study is to identify the effect of nonhydrodynamic fiber–fiber interactions on those rheological properties.

To systematically address the above issues, this thesis is structured as follows: In § 2 we familiarize the readers with the relevant parameters required to describe a suspension system. Then a single fiber motion, and the concepts of orbit constant and rotational diffusion process are explained. § 3 describes the computational hybrid lattice–Boltzmann method (LBM–EBF) that has been implemented in this research. An improvement on the current LBM–EBF method is proposed in that chapter for

future implementation purposes. § 4 – § 7 contain the results of the simulations of fiber suspension flow performed in this research. Each one of these chapters is self-contained, including a discussion of the relevant background material, and a brief description of the models involved, along with a discussion of the simulation results. § 4 – § 6 discuss the results for suspensions under simple shear flow. It should be mentioned that a part of § 5 branches out to show the solution of the evolution equation of fiber orientation, and it also discusses the implementation of a spherical harmonics based approach, to determine the orientation moments under the effect of an anisotropic diffusion. The methods for these implementations are adopted from relevant research groups, but nonetheless add fundamental understanding of the effect of a rotational diffusion process on fiber orientations. Some of the results are compared with LBM–EBF results to judge the prospect of the fiber–level simulations in predicting orientation properties in real molding processes. § 7 presents the results of LBM–EBF simulation for a complex flow geometry, namely a paper-machine headbox. The main conclusions from this research are summarized in § 8. Also presented in this chapter are recommendations for future work.

CHAPTER II

SINGLE FIBER MOTION AND ROTARY DIFFUSION PROCESS IN A SUSPENSION

Before we move on to describe the single fiber motion in a Newtonian fluid and rotary diffusion of rigid fibers in the semidilute suspension, it is important first to describe the parameters relevant to the suspension system and also describe the different suspension regimes. In § 2.1 we make this effort.

2.1 Parameters to describe the suspension system

For neutrally buoyant monodisperse rigid fibers in shear flow, where the fibers' aspect ratio, $r_p > 1$ ($r_p = L/d$, where L and d are length and diameter of the fiber respectively), the system can be described by the fluid density, ρ, the fluid viscosity, μ, the shear rate, $\dot{\gamma}$, the fiber radius, a, the aspect ratio, r_p, and the thermal energy, $k_B\mathcal{T}$. The related nondimensional parameters are the solid volume fraction, c_v (for cylindrical fibers, $c_v = \frac{n\pi d^2 L}{4}$, where n is the fiber number density), the particle Reynolds number, $Re_p = \frac{\rho\dot{\gamma}a^2}{\mu}$, the Peclet number, $Pe = \frac{\dot{\gamma}}{D_r}$, where D_r is the Brownian diffusivity. In many cases of practical interest, the size of the suspended particles is on the order of microns, and the particle Reynolds number is effectively zero. It can be seen that the Peclet number determines the relative importance of advection relative to diffusion. For Peclet number, $Pe \to \infty$, there is no Brownian motion, and the suspension is non-colloidal. A phase diagram of suspension rheology with the changes of Re_p and Pe (based solely on dimensional analysis) can be found in Stickel & Powell's [112] paper. A spherical particle diameter of 10 μm is often used to mark the point where Brownian motion becomes negligible [20]. It is worth mentioning

here that, the Re_p used in this numerical study is very small ($\mathcal{O}(10^{-4})$ to $\mathcal{O}(10^{-5})$); therefore, inertia is negligible. The lowest fiber length used in the simulation is 0.648 mm; therefore, the suspension is non-colloidal and Brownian motion is negligible.

Fiber suspensions are broadly divided into three regimes; dilute, semidilute, and concentrated regimes [36]. The spherical volume circumscribing a fiber scales like nL^3, and is referred to as the *interaction volume*, because fibers within this volume interact hydrodynamically. In the dilute regime, nL^3 is much less than unity (only one fiber in a volume of $V = L^3$), and therefore, each fiber can rotate freely with occasional interactions between fibers. The volume fraction satisfies, $c_v = n\pi\, d^2 L/4$. Since there is only one fiber in volume V, this leads to $c_v < d^2 L/V$, or $c_v < d^2/L^2$, or $c_v r_P^2 < 1$. The semidilute regime is defined by $nL^3 >> 1$ but $nL^2 d < 1$. In the semidilute regime each fiber is confined in the volume $d^2 L < dL^2$, so the concentration in the semidilute regime satisfies $1 < c_v r_p^2 < r_p$. The spacing between two neighboring fibers in the semidilute regime is greater than the fiber's diameter, but less than the fiber's length. As a consequence, each fiber effectively has many other fibers, on the order of $\mathcal{O}\left(nL^3\right)$, in its interaction volume. Finally, in the concentrated regime, $nL^3 > r_p$ or $c_v > d/L$ and the average distance between two neighboring fibers is less than its diameter, a fiber can only rotate independently about its symmetry axis. A cooperative effort of all surrounding fibers is necessarily required for any motion of the fiber.

2.2 Single fiber motion

Jeffery [59] solved for the motion of an isolated ellipsoid suspended in a Newtonian fluid. The description of fiber suspension rheology and in particular most current approaches of fiber orientation modeling are based on his theory. The theory gives an expression for the angular velocity, $\boldsymbol{\omega}$, of an ellipsoidal particle in an incompressible infinite Newtonian suspending fluid with no external forces or torques. It was

Hand [49] who showed that the Jeffery's equation is a special case of a more general equation obtained by Ericksen [38]. The general equation of Ericksen [38] is based on an invariant based theory of anisotropic fluid (TIF theory) for the evolution of a unit vector, $\mathbf{p}$, denoting a preferred direction at each material point of the fluid. Considering the unit vector, $\mathbf{p}$ (see figure 1) as the main axis of revolution of the ellipsoidal particle, and considering the cylindrical shape to be an approximation to the ellipsoid, the motion of the fiber may be expressed with the following Jeffery-Ericksen equation:

$$\dot{\mathbf{p}} = \boldsymbol{\omega} \times \mathbf{p} = \mathbf{W} \cdot \mathbf{p} + \lambda(\mathbf{E} \cdot \mathbf{p} - \mathbf{E} : \mathbf{ppp}) \tag{1}$$

where $\dot{\mathbf{p}}$ is material derivative of $\mathbf{p}$, $\lambda = \frac{r_p^2-1}{r_p^2+1}$ is the shape factor of the fiber. For long and slender fibers, $\lambda \to 1$. $\mathbf{W} = \frac{1}{2}(\mathcal{L} - \mathcal{L}^T)$ is the vorticity tensor, and $\mathbf{E} = \frac{1}{2}(\mathcal{L} + \mathcal{L}^T)$ is the strain rate tensor; i.e. the skew-symmetric and symmetric parts of the velocity gradient, $\mathcal{L}(= \nabla \mathbf{u})$ respectively. The ∇ (no subscript) represents the gradient operator in physical space, and $\mathbf{u}$ is the fluid velocity vector. Equation (1) may be interpreted physically as stating that $\mathbf{p}$ rotates with the fluid, as indicated by the term $\mathbf{W} \cdot \mathbf{p}$, and partially strains with the fluid, as given by $\lambda \mathbf{E} \cdot \mathbf{p}$. Since $\mathbf{p}$ is of unit length, the component of the motion which results in a change of length must be subtracted, giving rise to the final term, $-\lambda \mathbf{E} : \mathbf{ppp}$. The $\dot{\mathbf{p}}$ is a linear function of velocity gradient $\mathcal{L}$, and invariant under the transformation $\mathbf{p} = -\mathbf{p}$.

It should be mentioned that, two angles θ and ϕ in a spherical coordinate system (figure 1) are related to the unit vector $\mathbf{p}$ by:

$$\mathbf{p} = \left\{ \begin{array}{c} p_1 \\ p_2 \\ p_3 \end{array} \right\} = \left\{ \begin{array}{c} \sin\phi \sin\theta \\ \sin\theta \cos\phi \\ \cos\theta \end{array} \right\} \tag{2}$$

2.2.1 The concept of orbit constant (C_b)

Jeffery [59] found that in simple shear flows, an ellipsoidal body rotates indefinitely about the vorticity axis along one of an infinite number of periodic, closed orbits, with the choice of orbit being dependent solely on the initial condition. It was later discovered by Bretherton [21] that this is true for almost any rigid body of revolution, including circular cylinders, and the orbit period will become:

$$T = 2\pi \left(r_e + 1/r_e\right)/\dot{\gamma} \tag{3}$$

The major modification is that the particle aspect-ratio r_p is replaced with an effective aspect-ratio, r_e. Cox [31] found the semiempirical relation:

$$r_e = 1.24 r_p \left(\ln r_p\right)^{-1/2} \tag{4}$$

The spherical co-ordinate system used to describe fiber orientation is defined in figure 1. The differential equations governing the time evolution of θ and ϕ are:

$$\dot{\theta} = \frac{\dot{\gamma}\left(r_e^2 - 1\right)}{\left(r_e^2 + 1\right)} \sin\theta \cos\theta \sin\phi \cos\phi \tag{5}$$

$$\dot{\phi} = \frac{\dot{\gamma}}{\left(r_e^2 + 1\right)} \left(r_e^2 \cos^2\phi + \sin^2\phi\right) \tag{6}$$

Eqn. (6) indicates that the angular velocity about the vorticity axis (z), depends solely upon ϕ, and is independent of θ. Moreover, for $r_e > 1$ the angular velocity is greatest when the fiber is at right angles to the fluid motion ($\phi = 0$), and it is least when it points to the direction of motion ($\phi = \pi/2$). It is important to note that, because of the finite thickness of the fiber, the angular velocity never becomes zero. It follows directly from eqn. (6) that:

$$\frac{\omega\left(\phi\right)_{max}}{\omega\left(\phi\right)_{min}} = r_e^2 \tag{7}$$

where $\omega\left(\phi\right) = d\phi/dt$. This motion leads to a definite pattern of fiber orientation.

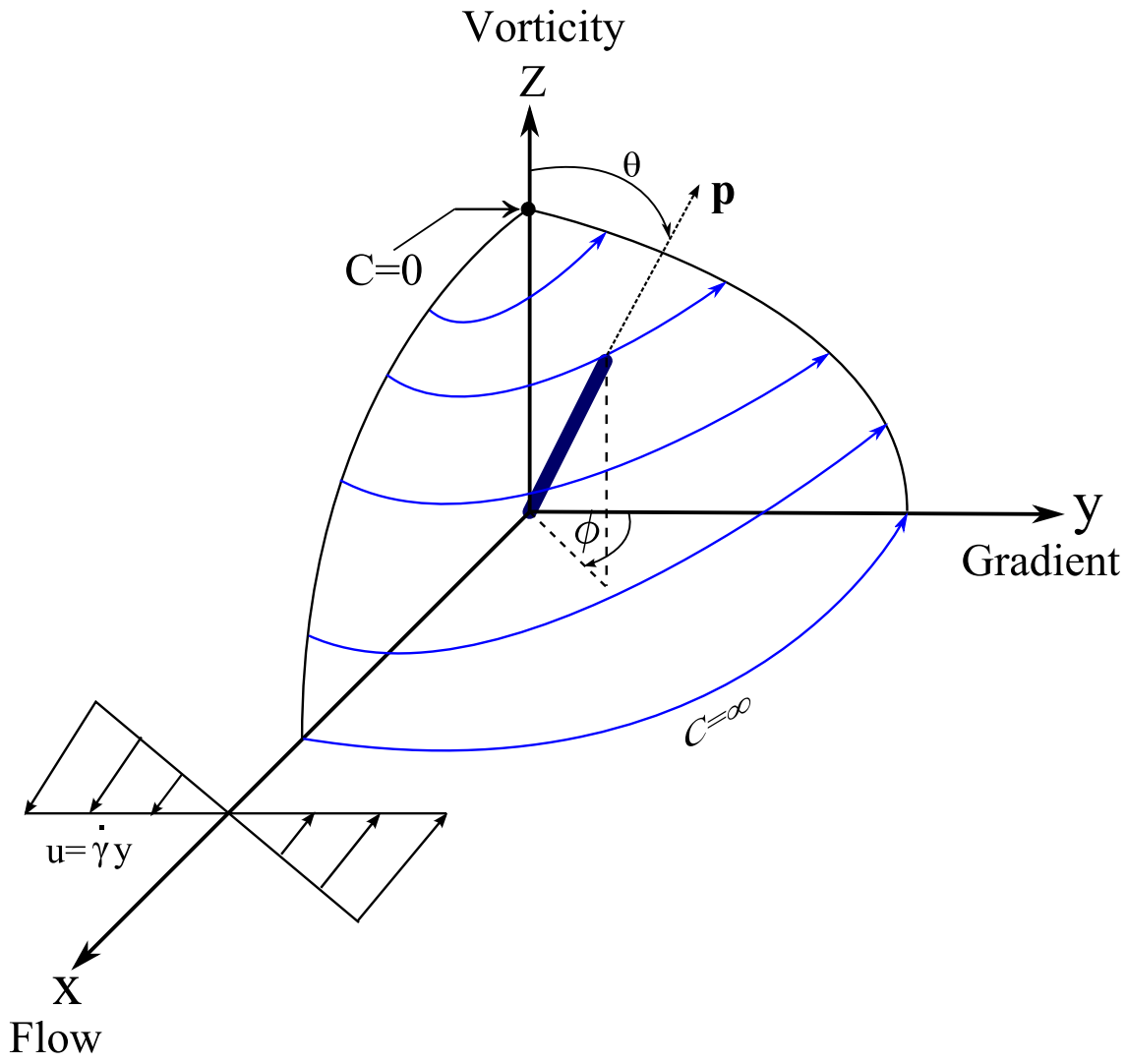

Figure 1: The co-ordinate system with a fiber centered at the origin. The unit vector, **p** is parallel to the fiber's axis. Typical orbits for a slightly prolate spheroid are shown with solid blue lines.

Leal & Hinch [70] showed that integration of the time evolution for θ and ϕ yields:

$$\tan\theta = \frac{Cr_e}{\left(r_e^2\cos^2\phi + \sin^2\phi\right)^{1/2}} \tag{8}$$

$$\tan\phi = r_e \tan\left(\frac{2\pi t}{T} + \kappa\right) \tag{9}$$

where κ is the phase angle. As is evident from eqn. (9), the motion is periodic. Since, from eqn. (8), corresponding to a given C, θ is uniquely defined by ϕ, the orbit described by the end of the fiber relative to its center is regular. Thus the fiber describes periodic motion in a regular orbit. This motion is precessional, analogous to that of a disturbed gyroscope. An important feature of a Jeffery's orbit is that a fiber spend a relatively long time aligned with the neutral plane of the flow, and then quickly rotates one-half revolution until it once again become aligned with the neutral plane, and so on. The orbits of the ends of the particle (fiber) are a symmetrical pair of spherical ellipses; their eccentricity is defined by:

$$C = \tan\theta_0 \sqrt{\cos^2\phi_0 + \frac{1}{r_e^2}\sin^2\phi_0} \tag{10}$$

where C is the orbit constant, and subscript '0' denotes the initial orientation. In the absence of particle interactions or inertial effects, C indefinitely remains constant for the individual fiber during its motion. The value $C = 0$ corresponds to perfect alignment of the fiber with the vorticity direction of the flow, and the cylinder rotates around its own axis, whereas $C = \infty$ corresponds to rotation in the flow gradient plane. In this case the rotating fiber describes a *disc*. When representing the orbit-constant distribution, it is advantageous to characterize the orbits with an orbit constant $C_b = C/(1 + C) \in [0, 1]$. Some other alternative orbit parameters of finite bounds can be found in [8].

2.3 Rotary diffusion process

Jeffery's solution gives the physical behavior of dilute inertialess suspension flows in which $nL^3 << 1$. However, in the semidilute regime, the fibers are hydrodynamically

coupled, and Jeffery's solution may not predict the orientation of the fibers in such suspension systems. The hydrodynamic interactions among fibers cause small changes in orientation of the fibers. This change in the orientation of one fiber because of the presence of its neighbors can be accounted for with a rotary diffusion process [70, 51, 52, 43, 105, 64].

It is important to be introduced to the ideas of the orientation space and of the orientation probability distribution function, Ω, before defining the rotary diffusion process. Since $\mathbf{p}$ is a unit vector, the space of all possible orientations is the surface of a unit sphere, which is known as the orientation space. At a given point $\mathbf{r}_c$, and at a given time t, the orientation probability distribution function Ω is defined over the orientation space such as:

$$\Omega \equiv \Omega\left(\mathbf{p}, \mathbf{r}_c, t\right) \tag{11}$$

Now, the rotary diffusion can be identified as a process which is defined only on the unit spherical surface (orientation space) traced by all possible fiber orientations, and not in the direction that the fiber is pointing. It can neither translate a fiber nor change the length of a fiber. The rotary diffusion can be a second-order tensor, $\mathbf{D}^r$, but with isotropic diffusion (in which case, changes in orientation due to interactions are equally likely in all directions), the rotary diffusivity is a scalar, D^r, and it becomes analogous to a Brownian rotary diffusivity. The criteria for rotary diffusion are [113]:

I. Any specific interaction only causes a small change in the orientation of a fiber.

II. These interactions must be frequent compared to Jeffery's orbit period, eqn. (3).

The first criterion ensures the proportionality between the flux and gradient of the probability distribution function, Ω, in orientation space. The diffusive theory would calculate an incorrect flux were a single interaction moved a fiber from one point to another in orientation space where the orientation-distribution function had a

different slope. The second criterion stands because, for a diffusive process, the evolution of a distribution function must be the result of many interactions.

The most common rotational diffusion model available is the phenomenological standard Folgar–Tucker model [43]. This model supplements the Jeffery's rotation rate with an isotropic, orientation diffusion process. This model can inappropriately decrease fiber alignment by compensating for factors also responsible for fiber dispersion [65]. Ranganathan & Advani [98] proposed an isotropic, orientation-dependent diffusivity (by modifying the standard Folgar–Tucker model) in which the interaction coefficient was inversely proportional to the average inter-fiber spacing. Hinch & Leal [70] accounted for a very weak isotropic diffusion but failed to reproduce Anczurowski & Mason's [9] experimental orbit constant distribution of fibers in dilute suspension. Rahnama et al. [97] reasoned that in an anisotropic flow field, the diffusion must be anisotropic, so they modified Hinch & Leal's [70] solution to propose an orientation-dependent, weak anisotropic diffusivity. Koch [65], Phan-Thien et al. [89], Phelps & Tucker [92] later proposed more complex and robust anisotropic diffusion models. The rotational diffusion models are visited in greater detail in § 4 and in § 5.

By using fiber–level simulation to predict fiber orientation information, we can analyze the rotational diffusion process and have a better understanding of the dynamics of the orientation behavior of the fibers in suspension. The next chapter discusses the lattice–Boltzmann method (LBM), and its coupling with the External Boundary Force (EBF) method to perform the fiber–level simulation.

CHAPTER III

COMPUTATIONAL METHODOLOGY

In this chapter, first and foremost, the motivation to use the lattice–Boltzmann method to study fiber suspension is discussed. Then, the important features of the hybrid technique that is used here – called 'LBM–EBF' [126, 127, 128] is presented. Along with that a numerical improvement over the existing LBM–EBF method is proposed.

Dynamic simulation of particle suspensions can be categorized into three modeling methods distinguished by the length scale on which the phenomena are represented [125].

The first category is a '*microscopic method*' on molecular scale; the conventional molecular dynamics (MD) approach was pioneered by Alden & Wainwright [6]. In this method, Newton's equations of motion are simulated with particles in vacuum interacting through Lennard-Jones, hard-sphere, and electrostatic types of inter-particle forces. Every particle follows the exact same rules of motion, and the method becomes easy to implement and to parallelize. However, the process is computationally intensive, since the equations of motion have to be solved for a large number of particles at each instant of time.

The second category, the '*macroscopic method*' addresses a higher level of length scale; here we can account for the interaction of, for example, entire protein or polymer molecules or large colloidal particles, or even larger fibers, beads, rods, coal particles, etc., with a continuum solvent of small molecules or particles. The physics

in this scale acts through macro-particle interactions through continuum-scale inter-particle forces, such as London-van der Waals, screened electrostatic, Derjaguin-Landau-Verwey-Overbeek (DLVO), and through hydrodynamic forces transmitting via the continuum fluid. The fluctuating thermal forces from the surrounding fluid will influence the motion of sufficiently small particles; this is known as the familiar phenomena of Brownian motion. The macroscopic method uses Navier–Stokes equations for incompressible fluid flow to model the particle suspension as a continuum media, and then the particle suspension is discretized by mesh generation. The outcome of the model is a system of nonlinear equations, which is solved using conventional numerical methods such as finite element (FE) or finite-difference methods. This macroscopic method has been used successfully to model particle suspensions such as with colloidal particles and sedimentation [54]. However, it is computationally expensive in systems with fine resolution meshes, particularly for three-dimensional cases. Now for a small particle the Reynolds number at this macroscopic length-scale, the large particles interact through continuum-level forces (hydrodynamic forces), and these forces are governed by linear Stokes equations. The highly regarded '*Stokesian Dynamics*' approach of Brady & Bossis [19] were developed based on those conditions. Some advantages of this method are its robustness, proven agreement with experimental results and relative computational efficiency.

While Stokesian Dynamics is accurate and efficient, it is also computationally intensive. Ideally, $\mathcal{O}(N^2)$ operations are required to determine the interaction among N particles, whereas many-body interactions or lubrication forces both require $\mathcal{O}(N^3)$ operations [19]. Recently, Sierou & Brady [107] developed a more efficient method, within the framework of Stokesian Dynamics, called Accelerated Stokesian Dynamics. In this method the calculations scale as $\mathcal{O}(N \ln N)$ as has been observed for simulations on the scale of 1000 particles for 100 strain units to compute long-time self diffusivities of particles [108]. The integral form of the Stokes equation can be

solved using boundary element methods that allow the simulation of deformable and non spherical particles; however these techniques are even more computationally demanding than Stokesian Dynamics.

The third category is the '*mesoscopic method*' and it includes the lattice–Boltzmann method (LBM). The idea of the LBM method is put forward in § 3.1.

3.1 The lattice–Boltzmann method

The lattice–Boltzmann method (LBM) is categorized as a '*mesoscopic method*'. The mesoscopic length scale is an intermediate length scale which can be described as being between the size of a quantity of atoms (molecule) and materials measuring microns (bulk material). Instead of solving the Navier–Stokes equations on the macroscopic level, the lattice-Gas (microscopic) and lattice–Boltzmann (mesoscopic) approaches consider a set of equations derived from statistical physics. The simple idea behind LBM is to look at the (average) momentum and interactions among fluid particles, and not at the time and space-development of the fluid. In contrast to the numerical simulation of the Boltzmann equation itself, this is done for a simplified (time and space-discrete) scheme. Unlike Stokesian Dynamics and boundary element methods, the hydrodynamic interactions are not assumed to be fully developed; instead the interactions are allowed to propagate on time scales below those of particle motion – resulting in spatial locality and scaling linearly ($\mathcal{O}(N)$ dependence) with the number of particles, N. The LBM is a powerful technique to simulate fluid flow, and to model colloidal and noncolloidal suspensions of rigid fibers of various shapes.

The pioneering works on the implementation of LBM to study suspension flow have been extensively published in literature by Ladd [67, 68], Ladd & Verberg [69]; Aidun & Lu [4] and Aidun et al. [5]. Several factors explain the usefulness of LBM to use in the fiber–level simulation and to study suspension flow. First, LBM provides straightforward and easy-to-implement boundary conditions necessary to couple the

fluid and suspended particles (fibers). Second, the linear scaling of the computation with number of particles (fibers), N as discussed above saves computational cost. The local nature and regular lattice grid facilitate easy and efficient parallel execution of LBM on distributed memory clusters, in contrast with competing numerical methods such as Stokesian Dynamics. Furthermore, the study of inertial effects [32, 94] is also possible, since, LBM reproduces the full Navier–Stokes equations. A comprehensive review (over the past decade) of application of LBM for complex flows has been published by Aidun & Clausen [3] which highlights the relative merit and disadvantages of the method, and also discusses different hybrid LBM techniques.

3.2 Hybrid approach: LBM with EBF

This research employs a novel hybrid lattice–Boltzmann method [126, 127, 128] that extends the LB method developed by Aidun and coworkers [4, 5, 32, 33]; this is used because it offers encouraging improvements over the traditional LBM with standard bounce-back (SBB) conditions, and because it incorporates a fiber model, that is specially suitable for high aspect-ratio cylindrical fibers. This LBM–EBF method emerged out of the necessity that in the conventional LBM (with SBB), fluid and solid domains share one regular Eulerian grid, which requires a costly scanning procedure at each timestep in order to define a solid boundary. Usually, the solid boundary resides at the midpoints of the lattice-links connecting the boundary nodes, and thus at each timestep the boundary shape may change slightly. This approximation error is not present in the LBM–EBF method, since it involves two independent but overlapping grid systems; the Eulerian grid represents the fluid domain, and the particles (fibers in this research) are mapped on Lagrangian grids. The solid boundary represented by the Lagrangian grid nodes is the actual and precise boundary of the fiber moving continuously through the fluid domain, as shown in figure 2. Also, the SBB is not ideal for resolving the narrow thickness of a high aspect-ratio fiber, but the fiber

model serves that purpose in a computationally efficient way by meshing the surface of a fiber with Lagrangian solid nodes (discussed in § 3.2.5).

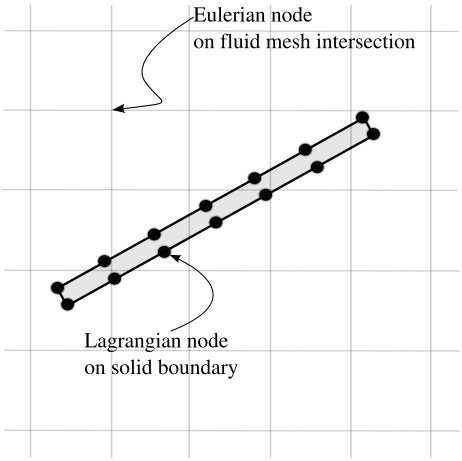

Figure 2: Schematic of LBM–EBF boundary illustration: The gray lines show the Eulerian fluid mesh. The deep black rectangle defines the solid (fiber) boundary. The solid boundary nodes (black filled circles) are located exactly on the fluid–solid boundary, Γ.

Wu & Aidun [126] validated the LBM–EBF method with single fiber simulations by verifying the accuracy of fluid–solid interactions, and by regenerating the motion of a flexible fiber with an elastic solid model. Many-fiber simulations were also performed [126, 127] to validate the solid–solid interactions through lubrication and contact models, and to validate the hydrodynamic coupling through the lattice–Boltzmann fluid. Both the accuracy and stability of the method were clearly demonstrated with those simulation results. The most important aspects of the LBM–EBF framework are outlined next. Also, importantly, an improvement over the previous LBM–EBF approach in terms of using the correct body force term in the LB equation is proposed in this PhD work.

3.2.1 The lattice–Boltzmann equation

The core concept behind the LB method is the solution of the Boltzmann equation on a regular lattice using discrete velocities. At every time step, fluid particles propagate to neighboring lattice nodes and undergo a collision operation that redistributes the momentum. Local mass and momentum for given nodes are obtained by summing the particle mass and momentum on the links coming from the nodes. The state of the fluid at node $\boldsymbol{x}^e$ (the superscript 'e' is used to symbolize eulerian fluid grid) at time t is described by the evolution of the distribution function, $f_k(\boldsymbol{x}^e, t)$. The evolution of this function $f_k(\boldsymbol{x}^e, t)$ is given by the single component LB equation with Bhatnagar-Gross-Krook (BGK) collision operator [16] as follows:

$$f_k(\boldsymbol{x}^e + \boldsymbol{e}_k, t+1) = f_k(\boldsymbol{x}^e, t) + \frac{1}{\tau}[f_k^{eq}(\boldsymbol{x}^e, t) - f_k(\boldsymbol{x}^e, t)]. \tag{12}$$

Here $f_k^{eq}(\boldsymbol{x}^e, t)$ is the equilibrium distribution function at $(\boldsymbol{x}^e, t)$, τ is the single relaxation time constant, and $\boldsymbol{e}_k$ is the discrete velocity vector. The fluid density, ρ, and the macroscopic fluid velocity, $\boldsymbol{u}(\boldsymbol{x}^e, t)$, are obtained from the first two moments, given by:

$$\rho(\boldsymbol{x}^e, t) = \sum_k f_k(\boldsymbol{x}^e, t) \tag{13a}$$

$$\rho(\boldsymbol{x}^e, t)\boldsymbol{u}(\boldsymbol{x}^e, t) = \sum_k f_k(\boldsymbol{x}^e, t)\boldsymbol{e}_k \tag{13b}$$

The most common lattice model for a two–dimensional case is D2Q9 model which uses nine discrete velocity directions, while the model for a three–dimensional case is D3Q19, which uses a cubic lattice having nineteen discrete velocity directions [5] for the fluid particles moving along the horizontal, vertical and diagonal links. The form of the equilibrium distribution function must be chosen so that fluid mass and momentum are conserved, and consequently, the resulting continuum equations describe the hydrodynamics of the fluid being simulated. The correct form of equilibrium distribution also ensures that the fluid is isotropic and Galilean invariant. The form

of equilibrium distribution function for incompressible flow is given by:

$$f_k^{eq} \approx w_k \rho \left[1 + \frac{(\boldsymbol{e}_k \cdot \boldsymbol{u})}{c_s^2} + \frac{(\boldsymbol{e}_k \cdot \boldsymbol{u})^2}{2c_s^4} - \frac{u^2}{2c_s^2} + \frac{(\boldsymbol{e}_k \cdot \boldsymbol{u})^3}{2c_s^6} - \frac{(\boldsymbol{e}_k \cdot \boldsymbol{u})u^2}{2c_s^4} \right] + \mathcal{O}(u^4) \quad (14)$$

where the weighting coefficients, w_k, are determined from the specific discrete velocity sets. In the two-dimensional D2Q9 model, $w_0 = 4/9$ for fluid particles at rest, $w_{1-4} = 1/9$ for fluid particles moving in non-diagonal directions, and $w_{5-8} = 1/36$ for diagonal directions; and for the three-dimensional D3Q19 model, $w_0 = 1/3$, $w_{1-6} = 1/18$ (non-diagonal directions), and $w_{7-18} = 1/36$ (diagonal directions). The pseudo speed of sound is $c_s = \sqrt{1/3}$, and the kinematic viscosity is $\nu = (2\tau - 1)/6$.

3.2.2 External Boundary Force method

The external boundary force method of Goldstein et al. [45] was advanced through the idea that the fluid simply *sees* a solid body through the forces of pressure (normal force) and shear that exist along the solid surface. Other surface effects might occur as well for non-isothermal and non-equilibrium flows. So in the overall fluid equations a force density can be added to account for the body's effect in fluid; i.e. an external force field can be applied rather than imposing certain boundary parameter values. Unlike the traditional Immersed-Boundary (IB) method [86, 87, 41], the Lagrangian nodes in the EBF method are not free to advect with the local fluid velocity. Instead, a momentum deficit is calculated between the solid and fluid velocities using the same weighting functions found in the IB method.

In the LBM–EBF method, the solid–fluid boundary, Γ, separates the solid and the fluid domain. The $\boldsymbol{x}$ with components (x, y, z) is used as the position vector in the fixed Cartesian coordinate system. The position vector for the jth node on ith fiber is given by $\boldsymbol{x}_{ij}^l$ in the solid domain, the position vector for the fluid nodes is represented by $\boldsymbol{x}^e$ in fluid domain, where superscripts l and e symbolically distinguish the position vector for solid nodes and fluid nodes, respectively. The $\boldsymbol{F}^{fsi}(\boldsymbol{x}, t)$ and $\boldsymbol{g}(\boldsymbol{x}, t)$ represent the force per unit volume acting respectively on the solid and the

fluid points $\boldsymbol{x}$ on Γ at time t. The Navier–Stokes, and the continuity equations with the external boundary force can be written as:

$$\left.\begin{aligned} &\rho\left(\frac{\partial \boldsymbol{u}}{\partial t}+\boldsymbol{u}\cdot\boldsymbol{\nabla}\boldsymbol{u}\right)=-\boldsymbol{\nabla}p+\mu\nabla^2\boldsymbol{u}+\boldsymbol{g}(\boldsymbol{x},t)\\ &\boldsymbol{\nabla}\cdot\boldsymbol{u}=0 \end{aligned}\right\}, \tag{15}$$

In this equation, $\boldsymbol{g}(\boldsymbol{x},t)=0$ when $\boldsymbol{x}\notin\Gamma$. In most situations the boundary nodes will not coincide with the fluid nodes, and thus an interpolation scheme is required. At each timestep(t) – the EBF method uses a discretized interpolation scheme to compute the external boundary force, $\boldsymbol{g}(\boldsymbol{x}^e,t)$ on the fluid boundary node, $\boldsymbol{x}^e$; the fluid velocity, $\boldsymbol{U}_f(\boldsymbol{x}^l_{ij},t)$ on solid boundary node $\boldsymbol{x}^l_{ij}$; and the fluid–solid interaction force $\boldsymbol{F}^{fsi}(\boldsymbol{x}^l_{ij},t)$ on the solid boundary node, $\boldsymbol{x}^l_{ij}$. This scheme uses a discrete Dirac delta function in the three dimensional domain [87]; the function is given by:

$$\delta(\boldsymbol{x})\equiv\begin{cases} \frac{1}{64h^3}(1+cos(\frac{\pi x}{2h}))(1+cos(\frac{\pi y}{2h}))(1+cos(\frac{\pi z}{2h})), & if|\boldsymbol{x}|\le 2h,\\ 0, & otherwise \end{cases} \tag{16}$$

where $h\equiv\Delta x^{LBM}$ is the unit lattice length in LBM calculation. Wu & Aidun [128] reported that, for linear velocity distributions, the interpolation (eqn. (16)) can give an exact solution. For smooth velocity distributions (continuous first order derivative), the interpolation has second order accuracy.

Now, with $\boldsymbol{F}_i(t)$ as the combination of the fluid–solid interaction force, external forces such as gravitational force, and interparticle forces such as electrical, lubrication or contact force on the ith fiber, and with $\boldsymbol{T}_i(t)$ as the total torque on the ith fiber, the Newtonian dynamics equations for that fiber are given by:

$$\left.\begin{aligned} &M_i\frac{\mathrm{d}\boldsymbol{U}_i}{\mathrm{d}t}=\boldsymbol{F}_i\\ &\boldsymbol{\mathcal{I}}_i\frac{\mathrm{d}\boldsymbol{\omega}_i}{\mathrm{d}t}+\boldsymbol{\omega}_i\times(\boldsymbol{\mathcal{I}}_i\cdot\boldsymbol{\omega}_i)=\boldsymbol{T}_i \end{aligned}\right\}, \tag{17}$$

where M_i and $\boldsymbol{\mathcal{I}}_i$ are respectively the mass and the inertial tensor of the ith fiber. The velocity, $\boldsymbol{U}_i$, and angular velocity, $\boldsymbol{\omega}_i$, are computed by a fourth-order accurate Runge–Kutta integration of eqn. (17).

As mentioned before, the fiber boundary nodes are subjected to the fluid–solid interaction force, $\mathbf{F}^{fsi}$, the external force which could include the gravitational force, $\mathbf{F}^{gra}$, and interparticle (electrical $\mathbf{F}^{ele}$, contact $\mathbf{F}^{con}$ or lubrication $\mathbf{F}^{lub}$) forces. In the present simulations, the fibers are considered to be neutrally buoyant. A lubrication force with an additional contact model is used to prevent fiber overlap. § 3.2.6 describes the form of this force in detail.

3.2.3 Improved body force model for EBF forcing term in LBM

The LBM method is widely successful in simulating many problems including magnetohydrodynamics [27], multiphase flow [42, 103, 118], colloidal [68] suspensions, and non-colloidal suspensions with rigid or deformable particles/capsules [77, 126, 127, 128]. An attraction of the method is its ability to simulate these quite diverse fluid flow systems by simply including the appropriate body force modeling terms into the LB equation [101, 103]. The LBM is very promising in its intuitive way to insert new physics at the mesoscale, as the LB method describes the fluid flow physics from a mesoscopic point of view. But it is important for the body force model, constructed at this scale, to follow the same stature of consistency of the LB method to represent macroscopic flow physics.

Now, there are situations where the body force term has spatial and/or time variations, which calls for a more cautious modeling effort [69, 47, 22, 48], than it is required for the modeling of a constant body force term such as gravity e.g. [50, 132]. A body force incorporating physical phenomena such as a surface tension force (as in multiphase flow) [3, 103, 93], applied electric potential in electro-osmotic flows, or centrifugal and coriolis terms appearing in the Navier–Stokes equations in a non-inertial reference frame are some examples of such body forces, whose modeling requires special exercise.

The external boundary force (EBF) method [45], that Wu & Aidun coupled with

LBM for the direct numerical analysis of three-dimensional rigid (or deformable) particles suspended in fluid, uses a novel technique to impose the no-slip boundary condition at the fluid–solid interface for stationary or moving boundaries. Hence, this surface body force is an instance of a body force which has spatial and temporal variations in the fluid domain (non-existent in the absence of moving and/or deformable solid boundary), and likewise requires heed to model properly in the mesoscale. In the previous implementation [126, 127, 128] of LBM–EBF, a simple forcing term (following the works of He et al. [50] and Succi [116]) was included in the LB BGK equation, which was not sufficient to recover the exact Navier–Stokes equations. Here, an improvement over that scheme is proposed.

A number of LB body force models were proposed in the literature [69, 47, 22, 134, 28, 78, 75] to deal with cases as described in the previous examples, but not all of them were entirely successful to eliminate the presence of non-hydrodynamic error terms at the macroscopic level. Through the review of Silva & Semiao [109], it is found that, only Guo et al.'s [47] LB body force model unequivocally recovers the macroscopic isothermal and incompressible continuity, and Navier–Stokes equations as the asymptotic solution of the LB BGK equation with a forcing term. In their method, the discrete lattice effects (finiteness of the lattice sets), and the contribution of the body force to the momentum flux are both considered. This method was thought to be acceptable for both steady and unsteady flow situations. Until recently, Silva & Semiao [109] introduced an additional constraint to the construction of the LB body force model: the time regime of the aimed hydrodynamic solution. Based on the Chapman–Enskog analysis, they derived the LB body force model that recovers the correct steady-state hydrodynamic equations with a body force. Silva & Semiao demonstrated that, their model is different from the Guo et al. [47] model (which is consistent only for time-dependent hydrodynamics). However, since the EBF force is space- and time-dependent, which gives a time dependent solution, the modification

required in the previous LBM–EBF implementation would be based on Guo et al.'s work [47] here.

3.2.3.1 ***Introduction of a body force term in the lattice–Boltzmann equation***

In the presence of a body force density $\boldsymbol{g}(\boldsymbol{x}^e, t)$, the LB equation eqn. (12), with a body force term can be written as:

$$f_k(\boldsymbol{x}^e + \boldsymbol{e}_k, t+1) = f_k(\boldsymbol{x}^e, t) + \frac{1}{\tau}[f_k^{eq}(\boldsymbol{x}^e, t) - f_k(\boldsymbol{x}^e, t)] + g_k(\boldsymbol{x}^e, t) \tag{18}$$

Here, the kinetic source term $g_k(\boldsymbol{x}^e, t)$ aims at reproducing the effect of a body force at the hydrodynamic level. The single particle distribution function zeroth order velocity moment is given by eqn. (13a), but the single particle distribution function first order velocity moment eqn. (13b) needs to be changed to include the hydrodynamic body force, $\boldsymbol{g}(\boldsymbol{x}^e, t)$ (proposed in the works of Ginzbourg & Adler[44] and Ladd [67]) as follows:

$$\rho(\boldsymbol{x}^e, t)\boldsymbol{u}(\boldsymbol{x}^e, t) = \sum_k f_k(\boldsymbol{x}^e, t)\boldsymbol{e}_k + a\boldsymbol{g}(\boldsymbol{x}^e, t) \tag{19}$$

The forcing term g_k can be written in a power series in the velocity space [69] such as:

$$g_k = w_k \left[A + \frac{\boldsymbol{B} \cdot \boldsymbol{e}_k}{c_s^2} + \frac{\boldsymbol{C} : (\boldsymbol{e}_k \boldsymbol{e}_k - c_s^2 \boldsymbol{I})}{2c_s^4} \right] \tag{20}$$

where A, $\boldsymbol{B}$ and $\boldsymbol{C}$ are functions of $\boldsymbol{g}$ to be determined by requiring that the moments of g_k are consistent with the hydrodynamic equations. The first three moments of g_k yield [132, 69, 47]:

$$\sum_k g_k = A \tag{21a}$$

$$\sum_k \boldsymbol{e}_k g_k = \boldsymbol{B} \tag{21b}$$

$$\sum_k \boldsymbol{e}_k \boldsymbol{e}_k g_k = c_s^2 A \boldsymbol{I} + \frac{1}{2}\left[\boldsymbol{C} + \boldsymbol{C}^{\mathrm{T}}\right] \tag{21c}$$

3.2.3.2 ***Recovery of hydrodynamic equations with a forcing term***

The Chapman–Enskog analysis is an asymptotic multitime scale expansion technique used to verify the consistency of a kinetic model to reproduce macrohydrodynamic behavior. Through this analysis, Silva & Semiao [109] obtained sufficient conditions for the order of truncation of the power series expansion of the LB body force model, eqn. (20), as well as the definition of its coefficient values, eqns. (21a) to (21c) for both the time-dependent and time-independent solutions respectively which can recover the Navier–Stokes equations in its true form. Silva & Semiao showed that, the body force term for a time-independent solution is different from the body force term proposed by Guo et al. [47], which was generally accepted as correct for both the steady and the unsteady-state flow regimes. Guo et al.'s proposed form of the body force term would be shown to be appropriate for the external boundary force method and it is important to note here that it is consistent only when a time-dependent solution is sought.

Listed below are the four essential steps of the Chapman–Enskog expansion, which was followed by Silva & Semiao [109] to derive the body force terms that reproduce consistent macrohydrodynamics physics:

1. Taylor expansion of the first term on the left-hand side of the LB equation, eqn. (18).

2. Multitime scale expansion of f_k about $f_k^{(0)}$ in terms of the Knudsen number, ε, and employment of a similar reasoning to the LB body force term, g_k [95]. Two distinctive time scales are considered in order to distinguish inviscid from viscous phenomena.

3. Expansions from steps 1 and 2 are introduced into the LB equation, eqn. (18), and the resulting equations are merged in terms of ε^0, ε^1 and ε^2 hierarchy.

4. Zeroth and first order velocity moments are computed for the equations derived in the step 3.

    4.1 Sufficient conditions are set to recover the inviscid hydrodynamic equations with a body force term by applying zeroth and first order velocity moments to the ε^1 hierarchy equation derived in step 3.

    4.2 Sufficient conditions are set to recover the correct hydrodynamics at viscous time scale with a body force term by applying zeroth and first order velocity moments to the ε^2 hierarchy equation derived in step 3.

The final result of Chapman–Enskog analysis established that the LB body force model for a time-independent solution (for a steady body force which can be spatially uniform/non-uniform) must be given by:

$$g_k = \left(1 - \frac{1}{2\tau}\right) \frac{w_k \boldsymbol{g} \cdot \boldsymbol{e}_k}{c_s^2} \tag{22}$$

And the LB body force model for a time-dependent solution (for an unsteady body force which can be spatially uniform/non-uniform) must be given by:

$$g_k = \left(1 - \frac{1}{2\tau}\right) w_k \left[\frac{\boldsymbol{e}_k - \boldsymbol{u}}{c_s^2} + \frac{(\boldsymbol{e}_k \cdot \boldsymbol{u})}{c_s^4} \boldsymbol{e}_k\right] \cdot \boldsymbol{g} \tag{23}$$

The body force term given in eqn. (23) was originally derived by Guo et al. [47]. Through the Chapman–Enskog analysis, Silva & Semiao [109] showed that, using this model, eqn. (23), in the LB equation would produce non-hydrodynamic error terms in a steady macroscopic solution; but this model unerringly recovers the macroscopic isothermal and incompressible continuity and Navier–Stokes equations for time-dependent flows.

Through the above analysis, the appropriate value of the coefficient 'a' to be used in single particle distribution first order velocity moment, eqn. (19), is shown to be $\frac{1}{2}$; this value remains the same in eqn. (19) for either of the body force models chosen.

Silva & Semiao used a D2Q9 model for the Chapman–Enskog expansion; but the body force models are applicable in D3Q15, D3Q19 and D3Q27 models as well, provided the results obtained from the fourth order tensorial moment are identical to that of D2Q9 model.

Guo et al. [47] carried out a numerical test for an unsteady flow (two-dimensional Taylor vortex flow) where the body force depends on both space and time. They validated their theoretical finding by showing that their method is the most accurate for this unsteady flow where the force changes in both space and time. Silva & Semiao [109] performed numerical experiments (steady Taylor Green vortex flow, and the extended Poiseuille flow) to compare their theoretical body force model with other proposed models available in previous literature. They showed that, for a steady-state solution, their model is the most accurate one. It is interesting that, although the model proposed by Guo et al. [47] is not consistent for steady-state hydrodynamics, that model still yielded the least error as compared to errors incurred by some other existing models. Silva & Semiao demonstrated that the most simple body force model [50, 116]: $g_k = \dfrac{w_k \boldsymbol{g} \cdot \boldsymbol{e}_k}{c_s^2}$ and $\rho(\boldsymbol{x}^e, t)\boldsymbol{u}(\boldsymbol{x}^e, t) = \sum_k f_k(\boldsymbol{x}^e, t)\boldsymbol{e}_k$ (i.e. $a = 0$ in eqn. (19)) recovers more non-hydrodynamic spurious terms at the macroscopic level, and also yields the less accurate LB steady-state hydrodynamics solutions. Unfortunately, due to its simplicity, this model is by far the most used irrespective of the nature of macroscopic solution aimed for. Since discrete lattice effect is not considered in this simple model, an inexact mass balance equation is recovered, which is identified to be the most dominant source of error. In previous LBM–EBF implementations, this model was used.

3.2.3.3 ***The correction of EBF forcing term in LBM to recover the true hydrodynamic equations***[1]

In the discretized LBM–EBF formulation, $\boldsymbol{g}$ is evaluated on the fluid boundary node by interpolation to find $\boldsymbol{g}(\mathbf{x}^e, t)$, since the fluid node might not coincide with the solid node. Previously [128, 126], the LB equation included the simple form of the body force term [50, 116]: $g_k = \dfrac{w_k \boldsymbol{g} \cdot \boldsymbol{e}_k}{c_s^2}$, and the single particle distribution first order velocity moment was given by: $\rho(\boldsymbol{x}^e, t)\boldsymbol{u}(\boldsymbol{x}^e, t) = \sum_k f_k(\boldsymbol{x}^e, t)\boldsymbol{e}_k$. It must be emphasized that, there is a typographical error in the body force term shown in the LB equation (in eqn. (14) of Wu & Aidun [128] or in eqn. (13) of Wu & Aidun [126]). In those published papers, the body force term was given as: $\frac{3}{2} w_k \boldsymbol{g} \cdot \boldsymbol{e}_k$; whereas, the body force term actually implemented in the LBM–EBF code was: $3 w_k \boldsymbol{g} \cdot \boldsymbol{e}_k$ for $c_s = \sqrt{1/3}$ (following the methods of He et al. [50] and Succi [116]). This simple model would recover larger nonhydrodynamic error terms in macroscopic solution as pointed out in § 3.2.3.2 of this study. Therefore, to be suitable for an improvement of the inclusion of external body force (EBF) term in LBM equation, the ability to accurately deal with the unsteady and non-uniform force imposed on the fluid by the solid must be provided by the scheme chosen; and as such the LBM–EBF method can be improved by using the body force model of Guo et al. [47] which can recover the exact Navier–Stokes equations.

So following the work of Guo et al. [47], the LB equation with the correct body force term which can account for the presence of an external boundary force density $\boldsymbol{g}(\boldsymbol{x}^e, t)$ in the fluid domain in the LBM–EBF method, is shown to be:

$$\begin{aligned} f_k(\boldsymbol{x}^e + \boldsymbol{e}_k, t+1) = f_k(\boldsymbol{x}^e, t) + \frac{1}{\tau}[f_k^{eq}(\boldsymbol{x}^e, t) - f_k(\boldsymbol{x}^e, t)] \\ + \left(1 - \frac{1}{2\tau}\right) w_k \left[\frac{\boldsymbol{e}_k - \boldsymbol{u}}{c_s^2} + \frac{(\boldsymbol{e}_k \cdot \boldsymbol{u})}{c_s^4}\boldsymbol{e}_k\right] \cdot \boldsymbol{g} \end{aligned} \tag{24}$$

[1]It should be mentioned that all the numerical results on rheology and fiber orientation presented in this PhD research are from using the previous LBM–EBF [128, 126, 127] approach; since, the improvement that is proposed here is performed at the final stage of the PhD research.

And the single particle distribution first order velocity moment should be given by: $\rho(\boldsymbol{x}^e, t)\boldsymbol{u}(\boldsymbol{x}^e, t) = \sum_k f_k(\boldsymbol{x}^e, t)\boldsymbol{e}_k + \frac{1}{2}\boldsymbol{g}(\boldsymbol{x}^e, t)$.

So to summarize the findings, it is proposed that the body force model of Guo et al. [47] is the most relevant and accurate method to be used for the external boundary force term g_k in the LB equation, since it can recover the exact Navier–Stokes equations for fluid flows subjected to a spatially varying, unsteady body force. Also, the typographical error in the body force model (as appeared in previously published LBM–EBF papers [126, 128]) is duly recognized and pointed out in this work; and the limitations of the previously implemented simple body force model (by He et al. [50] and Succi [116]) are discussed in the light of the works of Guo et al. [47] and Silva & Semiao [109].

3.2.4 Computational domain and boundary conditions

The LBM–EBF simulations are conducted to create a simple shear flow, which is common in many experimental setups, and is very important for rheological flows of industrial interests. In Cartesian co-ordinates (figure 1), indices 1, 2, 3 denote flow direction, x; gradient direction, y; and vorticity direction, z, respectively. Computations are carried out in a box-shaped domain Ξ defined by:

$$\Xi = \{\boldsymbol{x} : x_i \in [a_i, b_i], i = 1, 2, 3\} \tag{25}$$

where a_i and b_i are the lower and upper bounds of Ξ respectively, for each Cartesian co-ordinate component. With respect to the co-ordinate system shown in figure 1, $x_1 = x$, $x_2 = y$ and $x_3 = z$. The boundary $\partial\Xi$ is a union of the six planes:

$$\partial\Xi_{i1} = \{\boldsymbol{x} : \boldsymbol{x} \ \in \ \Xi \wedge x_i = a_i\}, \ i = 1, 2, 3 \tag{26a}$$

$$\partial\Xi_{i2} = \{\boldsymbol{x} : \boldsymbol{x} \ \in \ \Xi \wedge x_i = b_i\}, \ i = 1, 2, 3 \tag{26b}$$

Typical experimental investigations of sheared fiber suspensions use two laterally

moving solid walls to maintain the shear. This arrangement is captured in the LBM–EBF simulation by assigning moving solid wall boundary conditions to two opposing sides of the box-shaped computational domain, and by assigning periodic boundary conditions to the rest of boundary planes. Ξ is defined in eqn. (25) with:

$$a_1 = 0,\ b_1 = l_1, \tag{27a}$$

$$a_2 = 0,\ b_2 = l_2, \tag{27b}$$

$$a_3 = 0,\ b_3 = l_3 \tag{27c}$$

where l_2 is the gap height between the two walls in the gradient, y-direction, l_1 is the length in the flow, x-direction, and l_3 is the depth of the domain in the vorticity, z-direction. The boundary conditions for $\partial\Xi_{21}$ and $\partial\Xi_{22}$ (for the walls) are given by:

$$\mathbf{u}^{\partial\Xi_{21}} = -\frac{1}{2} l_2 \dot{\gamma} \hat{\mathbf{e}}_1,\ \ \mathbf{u}^{\partial\Xi_{22}} = \frac{1}{2} l_2 \dot{\gamma} \hat{\mathbf{e}}_1 \tag{28}$$

In order to minimize the duration of the transient at the onset of shear, sometimes, the initial condition of the fluid velocity is set to:

$$\mathbf{u}_0 = \dot{\gamma} y \hat{\mathbf{e}}_1 \tag{29}$$

In the simulations: $l_2 \geq 5L$, $l_1 = 4L$ and $l_3 = 4L$; where L is the length of the fiber. The upper limit of l_2 was used for simulations done in the lower bounds in the semidilute regime in order to include a sufficient number of fibers for statistical averaging. Petrich et al. [88] provided experimental evidence that $l_2 \geq 3L$ is sufficient to eliminate the wall effects from measurements of the first normal stress difference and viscosity. In this study, all spatial averages, including those of rheological properties, average orbit constant, the intensity of concentration variations are taken over the subdomain:

$$\Xi' = \{\boldsymbol{x} :\ 0 + L \leq x_2 \leq l_2 - L, \boldsymbol{x} \in \Xi\} \tag{30}$$

This subdomain is chosen in order to avoid wall effects, which occur at distances less than one fiber length from the wall [114]. A study of wall effects is presented

in § 4.2. The periodicity length in the flow direction l_1 is also kept large enough in the simulations so that a fiber passes a sufficient number of other fibers at a distance shorter than L.

The LB operators are modified in order to fit the periodic boundary conditions and no–slip wall boundary conditions; the modifications are described in Aidun et al. [5] and Ding & Aidun [33].

The initial orientation of the fibers is created by producing fiber position and orientation pairs from a combined spatial and orientation distribution. All instances of fibers intersecting the wall are excluded. Ideally, the generated distribution should be isotropic and spatially uniform. However, in some instances the initial distribution favored orientation closer to the flow-vorticity plane, which may affect the asymptotic orientation to some extent. To quantify this possibility, all the fibers are placed randomly in the flow-gradient plane as an initial condition. The resulting steady-state viscosity is compared with that of the case where the fibers are initially oriented in slightly preferred directions closer to the flow-vorticity plane. Any notable distinction between these two cases is not observed as the viscosity values varied within 5%.

3.2.5 Meshing of fibers in Lagrangian grid

For high aspect-ratio rigid rod-like fibers, it is adequate for computational accuracy to use Lagrangian boundary nodes only on the surface of the cylindrical body, and no internal nodes need to be placed inside the fiber volume. $(M \times N)$ number of boundary nodes are placed on each fiber, where M is the total number of hinges (m) (imaginary circles with circumference of $2\pi d$) along the fiber which span from the bottom periphery of the cylindrical fiber to its top periphery; N is the number of boundary nodes placed on each hinge in such a way that it cuts the circumference of the imaginary circle into N number of equal arcs as shown in figure 3. In the simulations, the value of N used is 4. The fiber is modeled as a chain of $(M-1)$ rods,

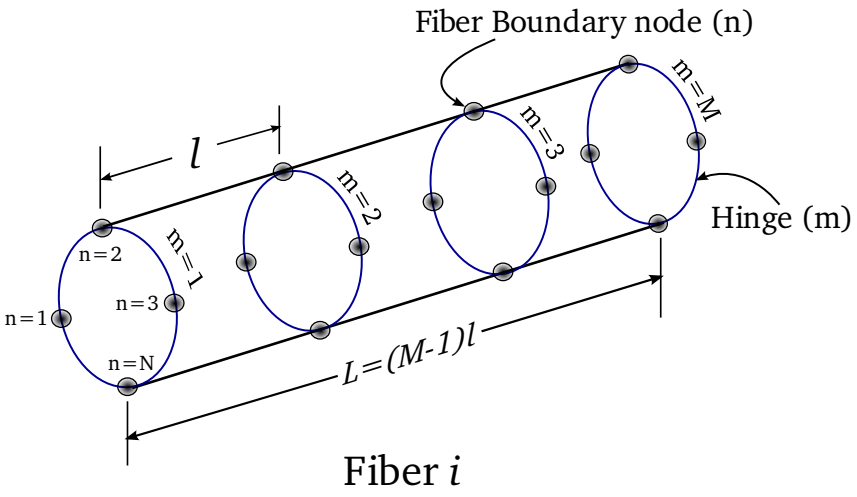

Figure 3: The fiber is modeled as a chain of rods connected with a total M number of hinges. The boundary nodes (n) on the circumference of each hinge are shown with grey circles.

and has an equilibrium length, l and a diameter, d. The fiber length is $L = (M-1)l$. As an example, in a sample simulation, $(M \times N = 11 \times 4)$ number of boundary nodes is used to model a fiber with aspect-ratio, $r_p = 20$. The effective volume of each hinge is $dQ \equiv \dfrac{L\pi d^2}{4M}$. When the fiber is flexible, the rods can bend and twist about the hinges, and the equilibrium lengths can be changed due to the forces applied on the boundary nodes. When dealing with rigid fibers, the hinges are assumed stiff. It should be noted that, in the LBM–EBF method, subgrid modeling is possible, and the diameter of a fiber is kept less than one lattice–Boltzmann length unit, i.e. $d < \Delta x^{LBM}$ for better accuracy and stability.

3.2.6 Fibers near contact

The accuracy of the LBM–EBF method, for resolving forces between fibers approaching very close to each other, depends upon the lubrication force model implemented. A lubrication force model similar to the form used by Yamane et al. [130], and Joung et al. [60] is used in the LBM–EBF as well. Let $\mathbf{V}_{im}$ and $\mathbf{V}_{jk}$ be the velocities of hinge

m in fiber i and hinge k in another similarly meshed fiber j, respectively (note, i can be equal to j for flexible fibers). The relative velocity component, $\mathbf{V}^{lub}_{im-jk}$, between these hinges is:

$$\mathbf{V}^{lub}_{im-jk} = \frac{\mathbf{r}_{im} - \mathbf{r}_{jk}}{|\mathbf{r}_{im} - \mathbf{r}_{jk}|} \left\{ \frac{\mathbf{r}_{im} - \mathbf{r}_{jk}}{|\mathbf{r}_{im} - \mathbf{r}_{jk}|} \cdot (\mathbf{V}_{im} - \mathbf{V}_{jk}) \right\} \tag{31}$$

where $\mathbf{r}_{im} - \mathbf{r}_{jk}$ is the position vector from hinge k to hinge m, and $|\mathbf{r}_{im} - \mathbf{r}_{jk}|$ is the length of the vector. The lubrication force density between hinges im and jk to the leading order is given by:

$$\mathbf{F}^{lub}_{im-jk} = -\frac{9\mu \mathbf{V}^{lub}_{im-jk}}{2d(|\mathbf{r}_{im} - \mathbf{r}_{jk}| - d)} \tag{32}$$

Then the lubrication force density applied on hinge im is :

$$\mathbf{F}^{lub}_{im} = \sum_{jk} \mathbf{F}^{lub}_{im-jk} \tag{33}$$

To avoid fibers crossing and to remove singularities when hinges overlap ($|\mathbf{r}_{im} - \mathbf{r}_{jk}| - d = 0$), the use of lubrication force, $\mathbf{F}^{lub}$, is restricted in the range of $d + \epsilon \leq |\mathbf{r}_{im} - \mathbf{r}_{jk}| \leq 1.25d$. Here, ϵ is a very small positive number to ensure a stable numerical simulation. If the gap is smaller than ϵ, the translational and rotational velocities are reset to make sure the relative velocity component along the direction with minimum distance between the surfaces is equal to zero.

One limitation of the current contact model is that it treats different kinds of contacts in the same manner. A category of contacts can be the group of cases where an interaction interface is close to a point, whereas another category can be the group of cases where a region of contact is a straight line or a curved line (for a flexible fiber). The types of relative motion can also vary. In some cases, the relative motion is normal to the surface, and in some cases surfaces are in shear. The relative position and motion could be the combination of these example cases. In different cases, the models for interaction forces should be different. But at present, the criteria for the onset of contact are the same – the lubrication force and the contact force

only depend on the shortest distance and the relative velocity between two contacting fibers. The current contact model also does not include multi-body contacts.

3.2.7 Computational resources

To simulate a reasonably large number, $\mathcal{O}(10^3)$, of fibers in the computational box, the calculations are conducted (with the application of OpenMP directive) on 4-processor workstation consisting of 2 GHz AMD Opteron 8350 ('Barcelona') quad-core processor (16 cores total). A typical run occupying 4-cores with approx. 2000 fibers (with e.g. $37 \times 2 \times 2$ Lagrangian nodes on each fiber surface) in an Eulerian fluid domain of $64 \times 64 \times 48$ lattice nodes usually takes order of weeks in clock time to reach a pseudo-steady state. Some of the runs are conducted utilizing the TeraGrid Cyber infrastructure facility. The maximum number of fibers simulated in this study is 10500.

Figure 4 shows an example of the time evolution of 995 fibers in the computational domain under a simple shear flow for different amounts of shear strain, $\gamma = \dot{\gamma}t$.

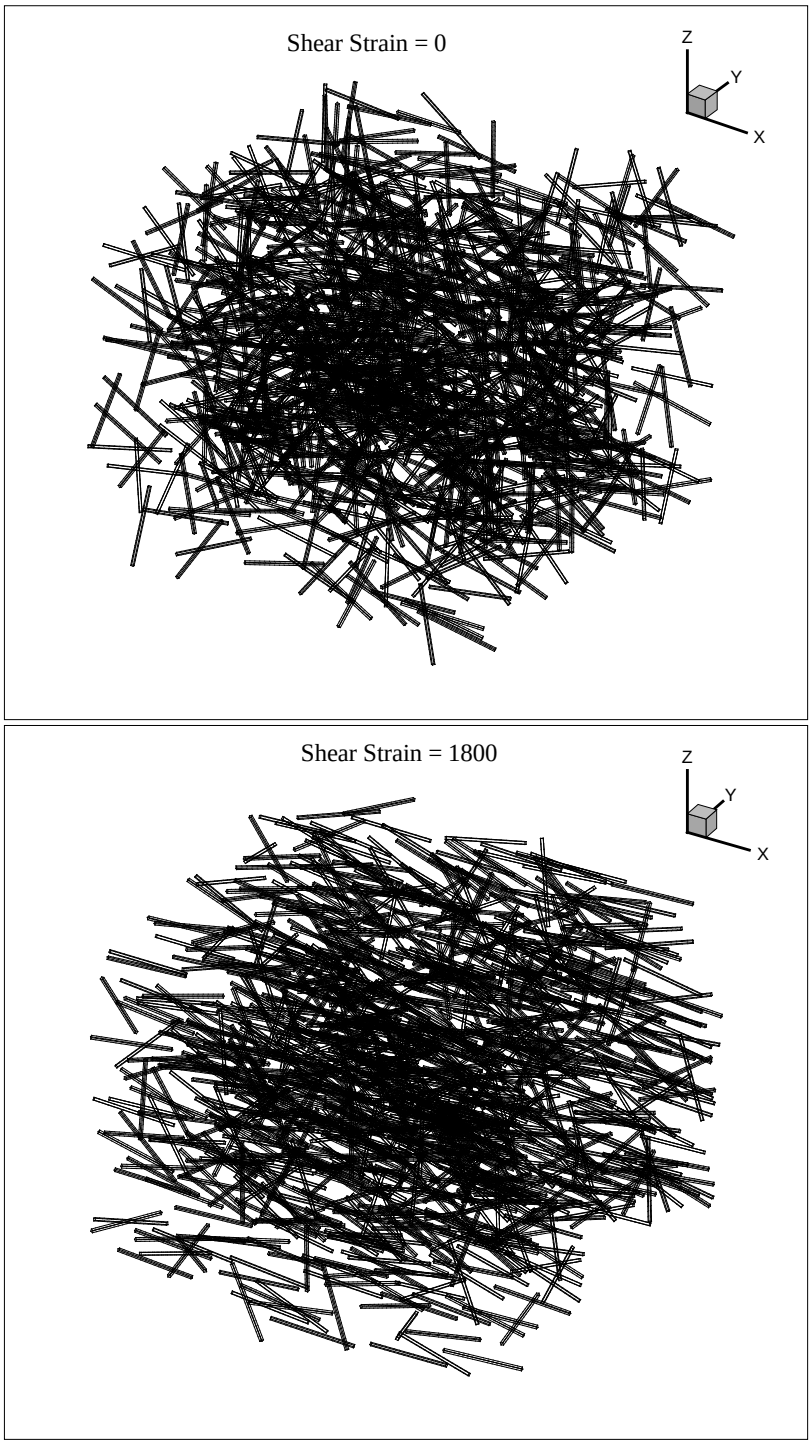

Figure 4: The time evolution of the configuration of 995 fibers ($r_p = 32$ and initially randomly oriented) at solid volume concentration, $c_v = 0.00767$ in a simple shear flow with LBM–EBF simulation. The amount of shear strain, $\gamma = \dot{\gamma}t$ is indicated above the figures.

CHAPTER IV

ORBIT CONSTANT DISTRIBUTION IN A SHEARED SEMIDILUTE SUSPENSION

In creeping flow, Jeffery [59] completely neglected effects such as fluid and fiber inertia, Brownian motion, fiber flexibility and fiber–fiber interactions. All of these may be present in a semidilute suspension, where free rotation is prohibited but the thermodynamic properties of the system are the same as in the dilute case. Jeffery's solution does not describe any steady-state orbit constant (C_b)-distribution, since according to the solution, the C_b-distribution is unchanged due to shear, and hence indeterminate. But in a semidilute system, all or some of the above mentioned effects might be present, which will cause small departures of orbits from the undisturbed creeping flow situation. This will lead to a slow change in the orbit of a fiber so that eventually a steady-state distribution of orbits, which is independent of the initial orientations of the fibers, may be established. In other words, a fiber in dilute suspension obeying Jeffery's solution has a perfect memory (the C_b-distribution is unchanged), whereas the fading memory effect in the semidilute suspension yields an unique steady-state orbit constant distribution.

In the absence of other factors, the hydrodynamic interactions among fibers can disturb the Jeffery orbits, which can give rise to a rotary diffusion process and a steady-state orbit constant distribution. In the past, investigations on these issues have mostly been performed for suspensions with concentrations lower than that under consideration in this research. In this chapter, numerical (LBM–EBF) simulation is used to predict the orbit-constant distribution of fibers in the semidilute suspension. Then we discuss the anisotropic weak diffusivity model 'A.W.D.M.' and test its

applicability in measuring rotational diffusivity in the semidilute regime.

4.1 Experimental and numerical simulations to determine the C_b-distribution

Anczurowski & Mason [8, 9] measured the orbit constant distribution of rods (with $r_p = 18.4$ and 20.3) in precision Couette flow with counter-rotating concentric cylinders. They used nylon fiber filaments in 5.1% by volume tetrabromoethane solution in Pale 4 oil. The orbit constant was calculated by measuring the maximum value of θ (see figure 1) by viewing the projection of the particle in the xz-plane. The lowest two concentrations ($nL^3 = 0.016$ and 0.066) had essentially the same orbit constant distribution, which indicates that they were both in the dilute regime, while the highest concentration ($nL^3 = 0.26$) favored higher orbit constants indicating a departure from the dilute regime. Stover et al. [115] observed the orientation of the semidilute, index-of-refraction matched suspension in a Newtonian fluid with one opaque tracer fiber in a cylindrical Couette device (figure 5). Stover et al. used cellulose acetate propionate (CAP) fibers of $r_p = 16.9$ and 31.9, in a mixture of glycerine and polyethylene glycol (PEG). From the recorded orientations of fibers, time-averaged C-distributions were constructed for the low aspect-ratio fibers, $r_p = 16.9$ in different concentrations of $nL^3 = 20, 10, 3$ and 1; and for high aspect-ratio fibers, $r_p = 31.9$ in $nL^3 = 45, 18, 10,$ and 5. The measured C_b-distributions were similar to each other, and markedly different from the dilute C_b-distributions measured by Anczurowski & Mason [9]. Anczurowski & Mason's dilute regime experiments yielded the peak values for C_b-distributions in the range of $0 < C_b < 0.25$; whereas, Stover et al. showed that the C_b-distributions have peaks in the range of $0 < C_b < 0.5$ for both the dilute and the semidilute systems.

Fiber-level numerical simulations have also been performed to determine the C_b-distribution in sheared suspension of non-Brownian rigid (or flexible) fibers in the last two decades. Yamane et al. [130] proposed an approximate method for the semidilute

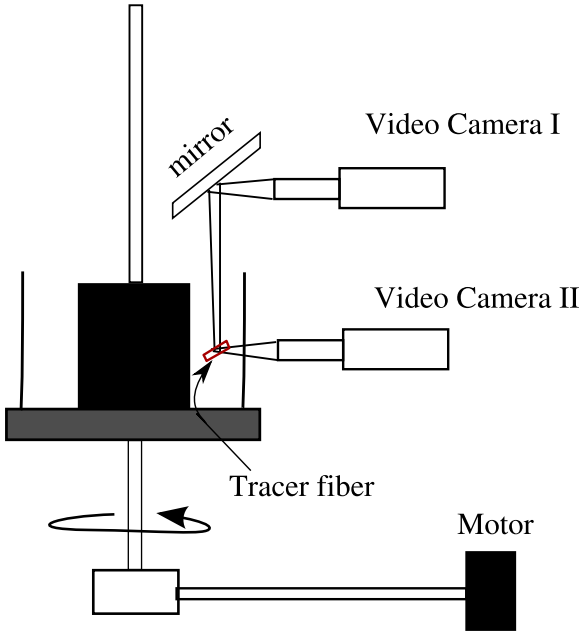

Figure 5: The Schematic of Couette device used by Stover et al. [115]

suspension where they only took into account short-range hydrodynamic interaction, which is modeled by the normal lubrication forces between close neighboring rigid rod-like fibers. The lubrication force is applied when the gap between two neighboring fibers becomes lower than a certain value. If the gap is larger than this value, then the fiber moves as a single rod in shear flow without the effect of any long-range hydrodynamic interaction. To simulate a statistically homogeneous system, a sheared periodic boundary condition is used. Yamane et al. predicted the steady-state distribution of C_b for $r_p = 16.9$ and $nL^3 = 20$ in a sheared suspension. The distribution of C_b shifted to higher values of C_b as the system was sheared. But Yamane et al.'s C_b distributions do not agree well with Stover et al.'s experimental results. This might be the result of neglecting long-range hydrodynamic interactions completely in the semidilute regime.

Fan et al. [40] employed the indirect boundary element method (BEM) and the completed double layer boundary element method (CDLBEM) [62, 90] to simulate

the periodic suspension of prolate spheroids accounting for hydrodynamic interaction among infinite particles. They used the slender body approximation (similar to Mackaplow & Shaqfeh's work [76]) for long-range hydrodynamic interactions, and a lubrication approximation (in the manner of Yamane et al. [130]) for short-range interactions.

In the dilute regime with $nL^3 = 0.016$, and with fibers of $r_p = 18.4$, Fan et al.'s simulations seemed to be randomly distributed in C_b, and therefore, the simulations did not agree with the corresponding experimental C_b of Anczurowski & Mason [9], which favored lower orbit constant, C_b values. Fan et al. attributed this disagreement to the difference in initial conditions between experiments and simulations. In the dilute experiments, the fibers were initially located in the orbits with lower values of C_b, i.e. close to the vorticity axis. The simulations had initial configurations generated by a pseudo-random sequence, and the C_b was distributed randomly. Fan et al.'s [40] simulated C_b distribution, for $nL^3 = 20$ with fibers of $r_p = 16.9$, in the semidilute regime was in qualitative agreement with Yamane et al.'s simulation data. However, by comparing the semidilute regime C_b-distribution of Fan et al. [40] (for $nL^3 = 45$ with fibers of $r_p = 31.9$), to the corresponding Stover et al. [115] experimental results, it is seen that – in simulation, more fibers drift toward the xy-plane relative to the experimental observation. In simulations, the fibers move in orbits within a range of about $0.42 \sim C \sim 1.12$ or $0.296 \sim C_b \sim 0.528$ which gave higher distribution probabilities in the region of larger C_b than was observed in Stover et al.'s semidilute experiments. Fan et al. tried to explain this discrepancy by mentioning that the inclusion of long-range hydrodynamic interactions drives the fibers to orbits with higher orbit constants. In fact, the small reference cells and a small number of fibers (e.g. only 40 fibers were used in the reference cell, for $nL^3 = 0.016$ and with fibers of $r_p = 18.4$, to save computational cost) might have caused large statistical errors in those simulations.

Lindström & Uesaka [71] performed a fiber–level simulation by taking into account both the short-range and the long-range hydrodynamic interactions, and additionally modeled the actual mechanical contacts among fibers in the simulation. The mechanical contact model certainly plays an important role in a semiconcentrated ($nL^2d = \mathcal{O}(1)$) to a concentrated suspension where the hydrodynamic interactions are weak and the mechanical contacts are dominant, but the model is also useful to account for any weak mechanical contact effects that might be present in the semidilute regime. The comparison of their semidilute results with Stover et al.'s experiments revealed that the simulations predict very well the C_b-distribution within the scatter of the measurement.

Sundararajakumar & Koch [117] numerically simulated rigid rod-like fibers in semiconcentrated regime with only a mechanical contact model. They showed that for slender fibers, lubrication force is not sufficiently strong to prevent actual physical contact between fibers, given that the fibers come very close to each other. For simplicity, they assumed frictionless contact so that the fibers could slide over each other. The fibers in the simulation showed a tendency toward alignment in the flow-gradient plane at higher fiber concentrations because of the strong mechanical contact effects.

It should be mentioned that numerical studies of orbit constant of a single flexible fiber have been performed by Skjetne et al. [110] and Ross & Klingenberg [99]. However in this study, the focus stays upon characterizing the orientation distribution of rigid fibers.

4.2 Prediction of orbit constant distribution with LBM–EBF

The LBM–EBF simulation method is employed to predict fiber orbit constant distribution in simple shear flow, where the velocity distribution of the bulk suspension flow is $\mathbf{u} = \dot{\gamma} y \hat{\mathbf{e}}_1$.

Before discussing the results in detail, it is important to quantify the sensitivity of the simulation results to several parameters, which are potential sources of error. Parameters investigated include the wall gap height, number of fibers, the time required to achieve an equilibrium state, and the intensity of concentration variations.

Since wall boundary conditions are used in the gradient, y-direction, a study has been performed to observe the effect of the walls on the orientation and the rheological properties. As mentioned in § 3.2.4, the lowest gap between the walls used in the simulation is $5L$ ($5\times$ fiber length). The spatial averages for rheological or orientational properties are computed within the sub-domain given by eqn. (30).

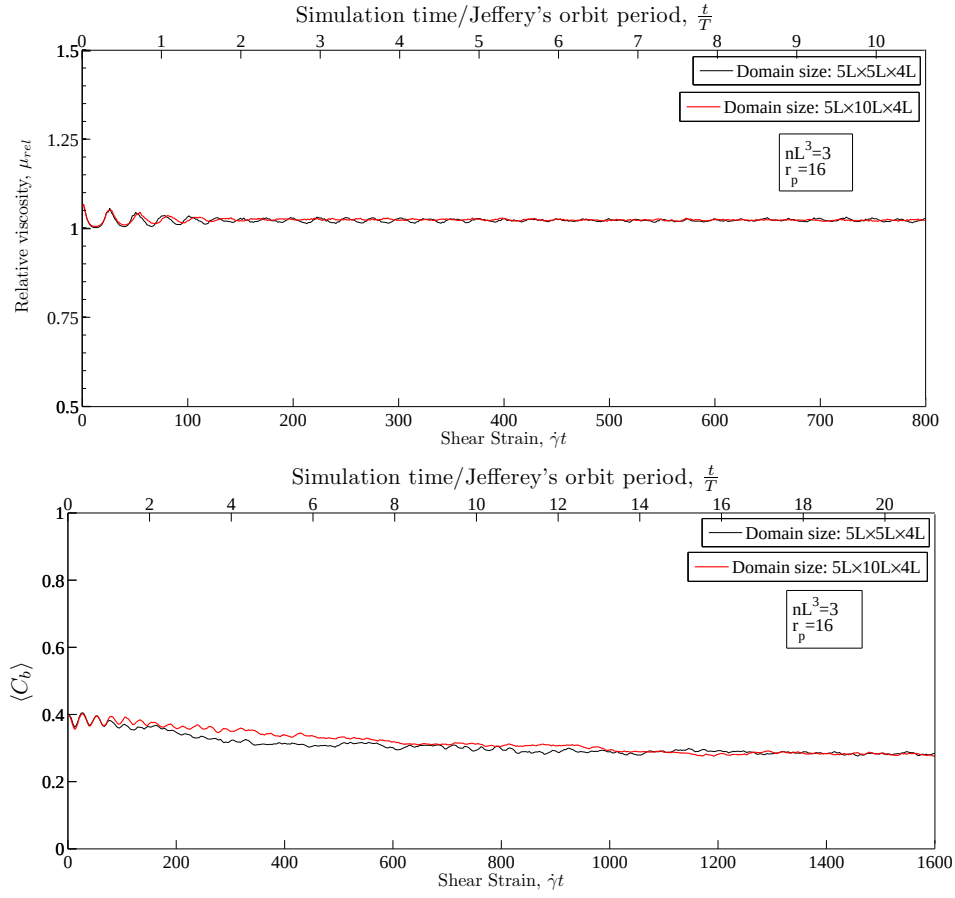

Figure 6: The effect of change of the wall gap on the orientation and the rheological properties of a suspension: (top figure) effect on the relative viscosity, μ_{rel} of a suspension, and (bottom figure) effect on the average orbit constant distribution, $\langle C_b \rangle$ of a suspension. The figures also demonstrate measures of the time scales required to achieve pseudo equilibrium (steady) states.

Figure 6 shows that, no statistically significant changes occur either between relative viscosities, μ_{rel} (μ_{rel} is the ratio of suspension viscosity to the continuous phase viscosity) or between average orbit constants, $\langle C_b \rangle$ at steady states when the gap height is increased from $5L$ to $10L$. μ_{rel} changes by less than 2% at steady-state when the wall height is increased in figure 6. Overall in our simulations, the changes remain within $\pm 5\%$ for both steady-state $\langle C_b \rangle$ and μ_{rel} by varying the wall gap from $5L$ to $10L$.

Figure 6 also demonstrates that, during the transient, both $\langle C_b \rangle$ and μ_{rel} undergo a damped oscillation process, but eventually, the oscillations level out and attain small signal to noise ratios, as inspected by the eye. The damping in the rheological property such as μ_{rel}, is primarily due to particle interactions (although polydispersion can contribute to damping as well) and is in agreement with the theoretical predictions (Ivanov & van de Ven [56], Okagawa et al. [83]) and experimental observations (Ivanov et al. [57], Ivanov & van de Ven [56]).

Again it is apparent from figure 6 that the parameter $\langle C_b \rangle$ achieves a statistically steady-state after more shear is applied than is required for the relative viscosity, μ_{rel} to reach such a state. Anczurowski & Mason [8, 9] showed that the C_b-distribution evolves into a steady-state with more shear being applied to the suspension. Hence, an additional time scale exists for the relaxation of C_b-distribution, and a more stringent test can be performed to confirm the equilibrium state for orbit constant distributions. Stover et al. [115] experimentally found that the time correlation function of the orbit constant in the semidilute suspension decays exponentially with the delay time at the characteristic time scale, $\tau_c \approx \dfrac{270}{nL^3\dot{\gamma}}$. It should be mentioned that the theoretical calculation by Rahnama et al. [97] gives comparable but slightly higher measures of τ_c. A fiber can lose correlation only after it comes into interaction with a sufficient number of fibers. Lindström & Uesaka [72] normalized the experimental τ_c of Stover

et al. with Jefferey's orbit period, T which yielded:

$$\frac{\tau_c}{T} \approx \frac{43}{nL^3 r_e} \tag{34}$$

Thus, the particular case shown in figure 6, has $\frac{\tau_c}{T} \approx 1.203$. The correlation time is smaller when the suspension concentration increases. For example, a suspension of $nL^3 = 45$ with fibers of aspect-ratio, $r_p = 32$ has $\frac{\tau_c}{T} \approx 0.045$ according to eqn. (34). The durations of the simulations in this study vary between $22\tau_c$ to $150\tau_c$, where the upper limit corresponds to the highest concentration simulated.

Figure 6 also demonstrates the sensitivity of results on the number of fibers simulated. Since the nL^3 value does not change ($nL^3 = 3$) regardless of the domain sizes in figure 6, the number of fibers has to change from 652, for a $5L \times 10L \times 4L$ domain, to 300 for a $5L \times 5L \times 4L$ domain, respectively. It can be said that the oscillations damp out at a slightly faster rate when fiber numbers are higher, as can be visible specially in the relative viscosity, μ_{rel} vs. shear strain plot in figure 6.

Fiber clumping and flocculation can i.e. Spatial inhomogeneity in the simulation domain can also affect the overall fiber orientation in the simulation domain. In Appendix B, a parameter termed as intensity of concentration variations is studied. This parameter showed that in the semidilute range, the concentration variation is very low.

Now, after having confidence on the simulation results, we move into analyzing the orbit constant distribution of fibers in semidilute suspension at a steady state. It should be mentioned that, in order to minimize the duration of transient at the onset of shear, sometimes, the initial condition of the fluid velocity is set to $\mathbf{u}_0 = \dot{\gamma} y \hat{\mathbf{e}}_1$.

In the simulation, the flow kinematics is known, but the motion of each fiber is tracked. For example, figure 7 shows the orbit of the end of a tracer fiber ($r_p = 32$) in the semidilute suspension, at $nL^3 = 5$, with LBM–EBF simulation. The black path indicates the initial Jeffery's orbit, $C_b = 0.414$ at zero shear strain. At a shear strain of 2148 (approx.), the fiber has been moving along different Jeffery's orbits for 16

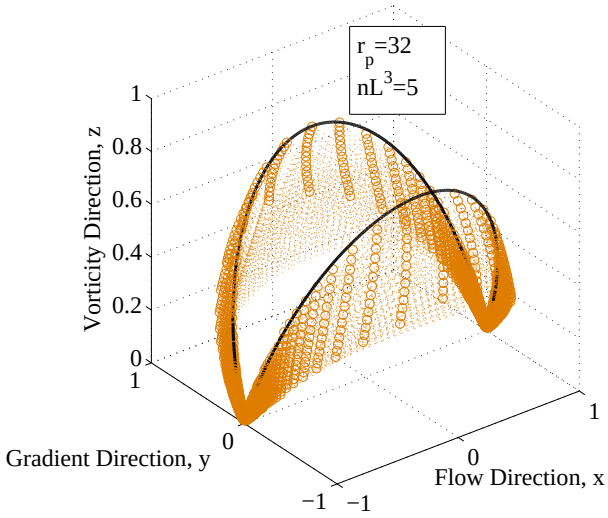

Figure 7: The orbits traced by one end of a tracer fiber with $r_p = 32$ in a semidilute suspension ($nL^3 = 5$) under a shear deformation with shear strain from 0 to 2148 (approx.).

(approx.) cycles (brown dotted paths) due to hydrodynamic interactions with other fibers. The orientation data are collected at every 1800 LBM timesteps, i.e., at every 1.293 shear deformation. From the density of the circles on every orbit, it also can be seen that the fiber spent more time in the orientation close to the flow direction.

The positions and the orientations of the fibers are output at specific time (shear strain) intervals. The output is post processed to form the C_b-distribution as follows:

1. The angles θ and ϕ (figure 1) are calculated from the *direction cosines* of the line passing through the fiber's axis.

2. The orbit constant, C, for that fiber is calculated with eqn. (8). The equivalent aspect-ratio, r_e is calculated with eqn. (4) to be used in eqn. (8) . The orbit constant, C_b (which has finite bounds) is calculated as $C_b = C/(1 + C) \in [0, 1]$.

3. Steps 1 and 2 are repeated to calculate the C_b values for all the fibers.

4. The span of C_b is divided into n number of bins, where $\sum_{i=1}^{n} dC_{b(i)} = 1.0$. The

MATLAB® function **'hist'** distributes the fibers into i number of bins based upon their corresponding $C_{b(i)}$ values. Now the probability of finding a specific fiber in the i-th bin is calculated as: $p\left(C_b\right) = \frac{no.\ of\ fibers\ in\ C_{b(i)}}{total\ no.\ of\ fibers}$.

5. $p\left(C_b\right)$ is normalized with the integral area under the histogram.

6. $p\left(C_b\right)$ is averaged over the last two orbit periods simulated.

Figures 8 – 10 compare the C_b-distributions predicted with LBM–EBF simulations to those of Stover et al.'s [115] experiments for nL^3 5 to 45. The C_b-distribution with LBM–EBF simulations validated the experimental results very well. The peaks of the C_b-distributions remain in the range $0.15 < C_b < 0.4$ for LBM–EBF which is consistent with the experimental results. The rotary diffusion process, which is the underlying mechanism that governs the C_b-distribution, would be analyzed next; and it should now be mentioned that the solid curves in figures 8 – 10 actually demonstrate the applicability of a particular rotary diffusion model to describe the C_b-distributions. This topic is the subject matter of § 4.3.

4.3 Rotational diffusion from C_b-distribution

Leal & Hinch [70] tried to develop a solution for the steady-state C-distribution of rod-like fibers obeying Jeffery's equation; their approach was to account for a weak scalar rotary diffusivity (i.e. rotary Brownian motion) in a shear flow, in the limit when the rotary diffusivity goes to zero. The solution method stipulates that the net flux of particles to any particular orbit is zero at the steady-state. In the solution for C-distribution function, no $\mathcal{O}\left(D^r\right)$ terms exist because of the double limiting process that occurs, in which rotary diffusivity goes to zero, and time goes to infinity. But in the dilute limit for non-Brownian fibers, this solution method did not reproduce Anczurowski & Mason's [9] experimental C-distribution, and the conclusion drawn was that either infrequent strong interactions are important to this problem or distant

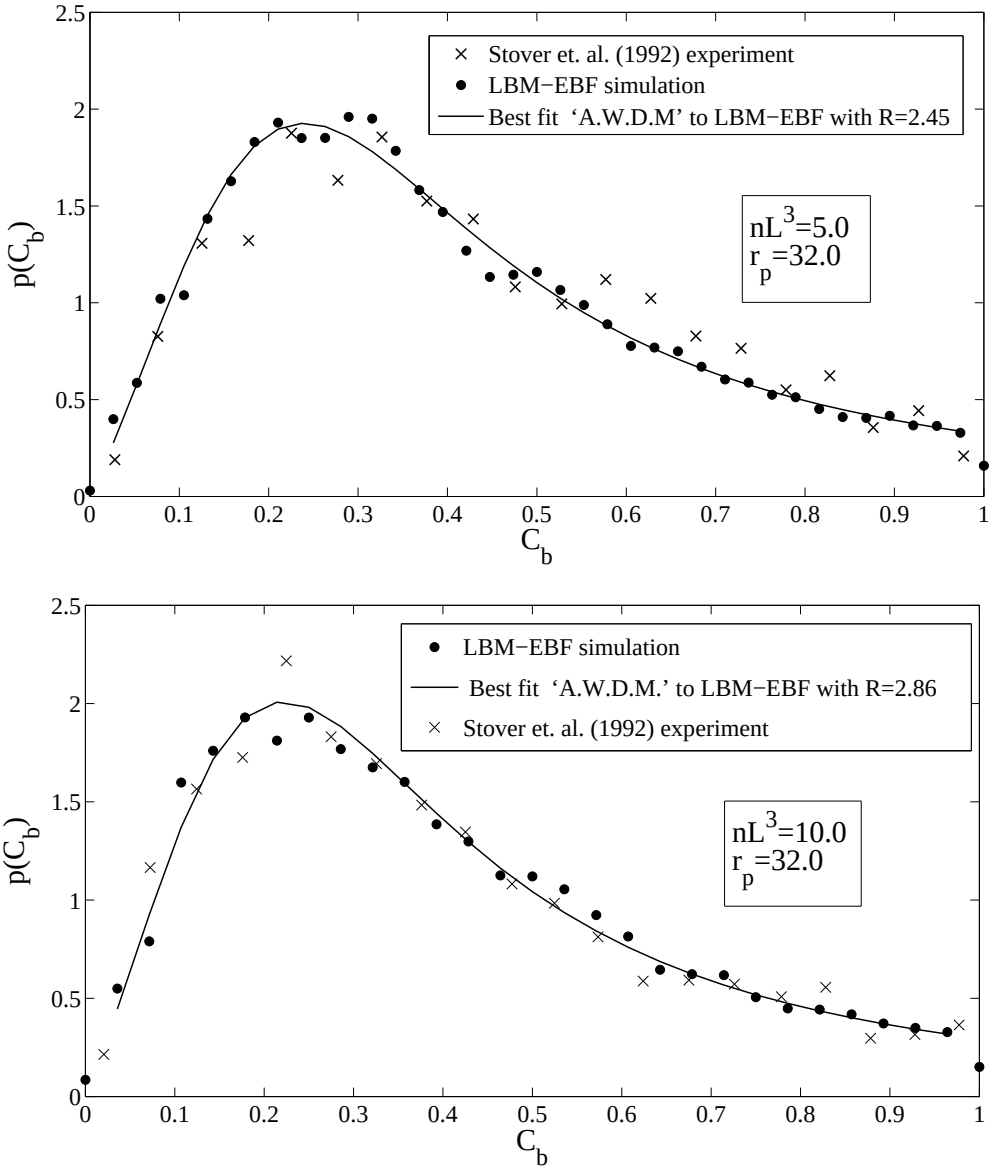

Figure 8: $p(C_b)$ with r_p=32.0, for nL^3=5 (top figure), and for nL^3=10 (bottom figure), respectively. The experimental C_b-distributions are within the 80% confidence interval. The solid curves demonstrate the one-parameter fit (with parameter R) of 'A.W.D.M.' to LBM–EBF simulation data. The best-fitted R values are indicated in corresponding legends.

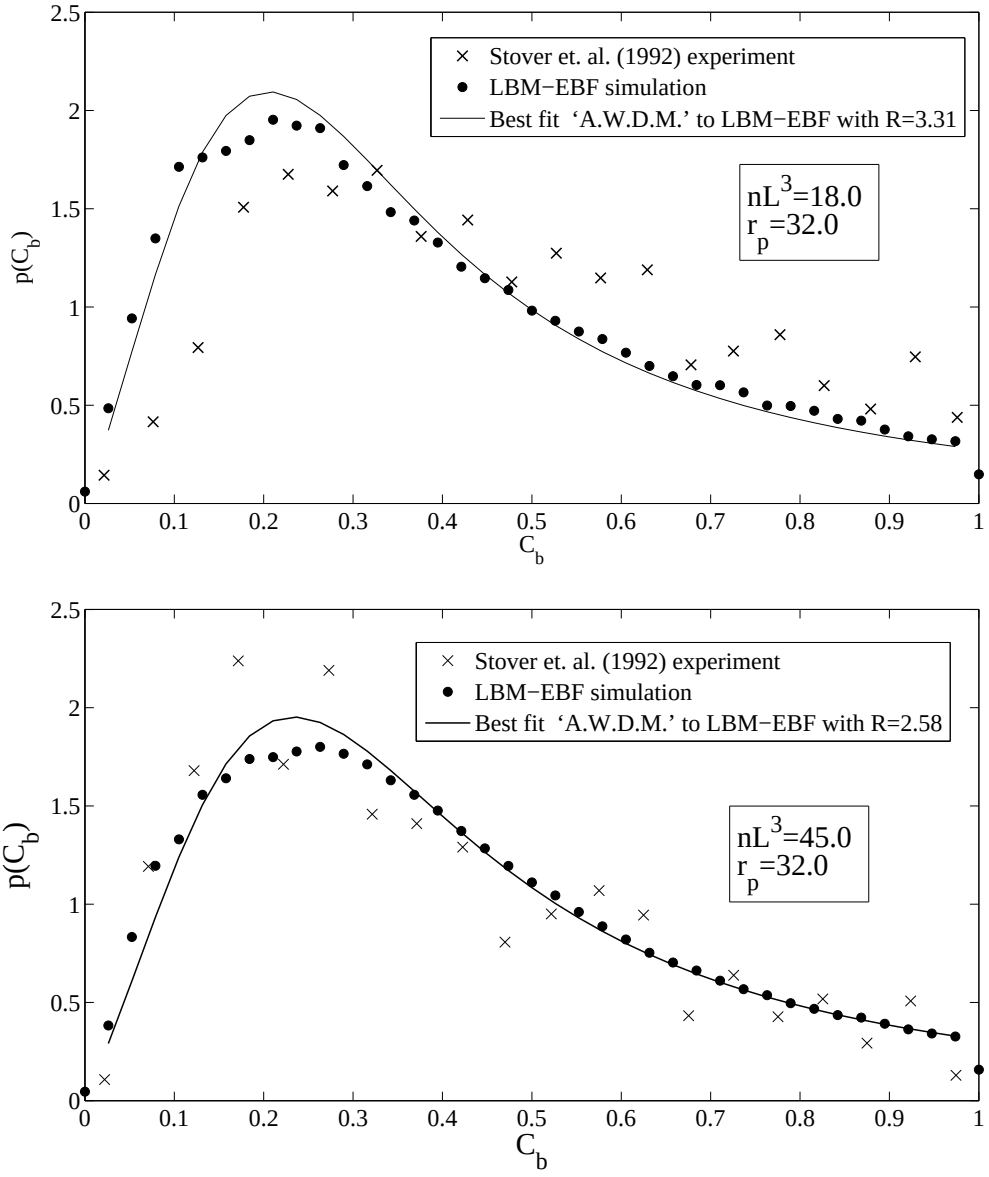

Figure 9: $p(C_b)$ with r_p=32.0, for nL^3=18 (top figure), and for nL^3=45 (bottom figure), respectively. The experimental C_b-distributions are within the 80% confidence interval. The solid curves demonstrate the one-parameter fit (with parameter R) of 'A.W.D.M.' to LBM–EBF simulation data. The best-fitted R values are indicated in corresponding legends.

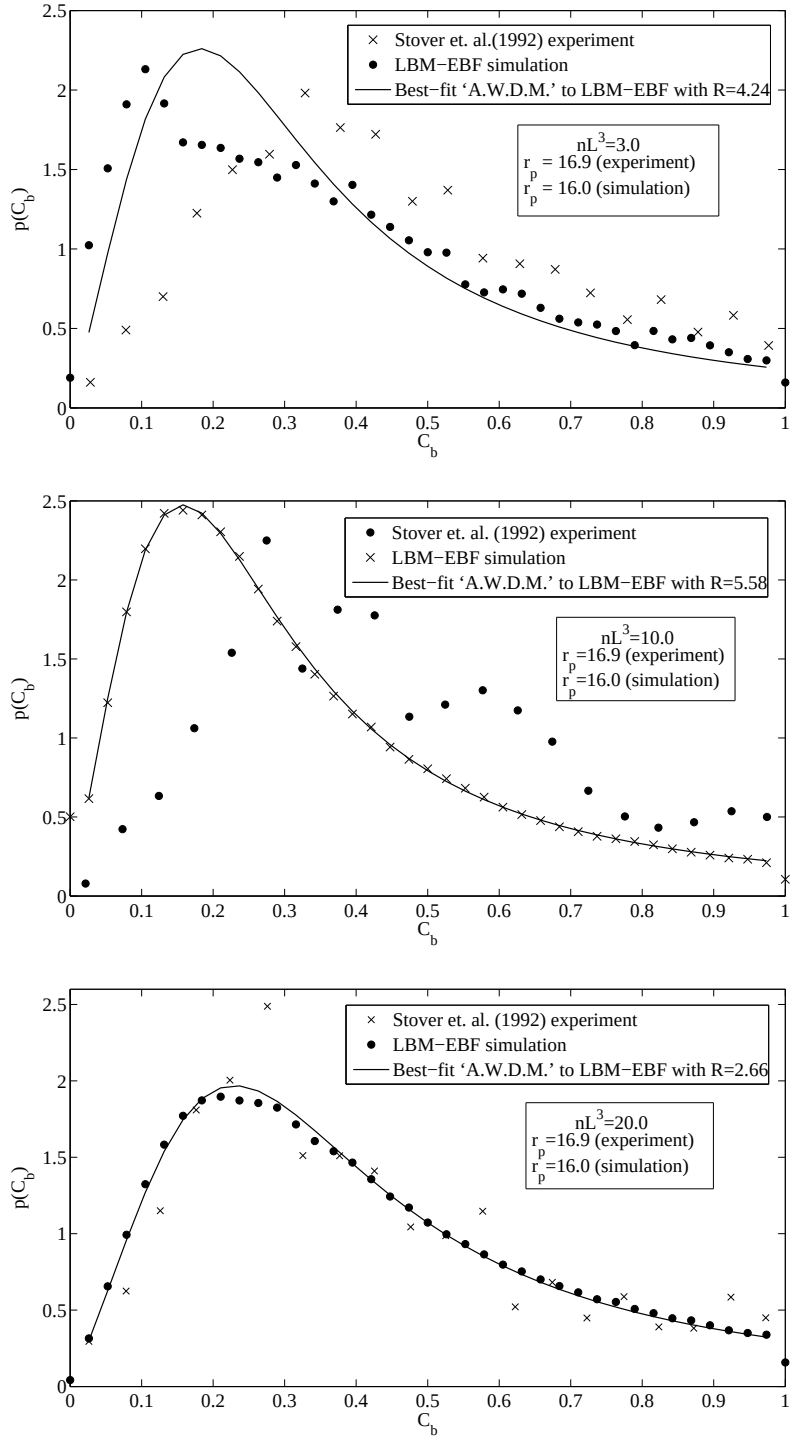

Figure 10: $p(C_b)$ with nL^3=3, 10, or 20, from top to bottom figure, respectively. The r_p=16.9 for the experiment, and r_p=16.0 for the simulation. The experimental C_b-distributions are within the 80% confidence interval. The solid curves demonstrate the one-parameter fit (with parameter R) of 'A.W.D.M.' to LBM–EBF simulation data. The best-fitted R values are indicated in corresponding legends.

interactions are described poorly by a rotary diffusivity. Stover in his PhD thesis [113] compared this weak isotropic diffusion model to his experiments, and discovered that the model was able to qualitatively describe the C-distribution in the semidilute regime better than it did in the dilute regime. Intuitively, if the effects of interactions can be modeled as a rotary diffusion process, one would expect the dilute regime to be well described by a weak diffusivity, and perhaps a finite diffusivity would be required for the non-dilute cases. Stover's effort to explain this behavior comes from consideration of the effects of an anisotropic weak rotary diffusivity.

The anisotropic orientation distribution function, which may evolve from the imposed anisotropic flow field, makes it unreasonable to expect an isotropic diffusivity to account for the hydrodynamic interactions in that anisotropic flow field. Rahnama et al. [96] and Rahnama et al. [97] generalized Leal & Hinch's [70] solution to the Burgers [23] evolution equation by including the orientation-dependent, anisotropic diffusivity tensor and a drift velocity. So the differential probability distribution function, $\Omega(\theta, \phi, t)$, looks like:

$$\begin{array}{lll} \frac{\partial \Omega}{\partial t} + \underbrace{\nabla_p \cdot \left(\dot{\mathbf{p}}^J \Omega\right)}_{\substack{\textit{convection along} \\ \textit{Jeffery orbits}}} & = \underbrace{\nabla_p \cdot \left(\mathbf{D}^r \cdot \nabla_p \Omega\right)}_{\substack{\textit{divergence of flux} \\ \textit{due to} \\ \textit{hydrodynamic diffusion}}} & - \underbrace{\nabla_p \cdot \left(\Omega \dot{\mathbf{p}}^h\right)}_{\substack{\textit{divergence of flux} \\ \textit{due to} \\ \textit{drift velocity}}} \end{array} \tag{35}$$

where ∇_p is the gradient operator in orientation space, $\dot{\mathbf{p}}^J$ is the rotation rate of the fiber as described by Jeffery, $\mathbf{D}^r$ is the anisotropic weak diffusivity tensor, and $\dot{\mathbf{p}}^h$ is the drift velocity. Some postulations about the origin of drift velocity include inhomogeneous mean shear flow, inertial effects, non-Newtonian effects, non-hydrodynamic fiber–fiber interactions, and deformation of the suspended fibers [64]. Since the diffusion is weak, so to the leading order, the steady-state distribution function is governed by:

$$\nabla_p \cdot \left(\dot{\mathbf{p}}^J \Omega\right) = 0 \tag{36}$$

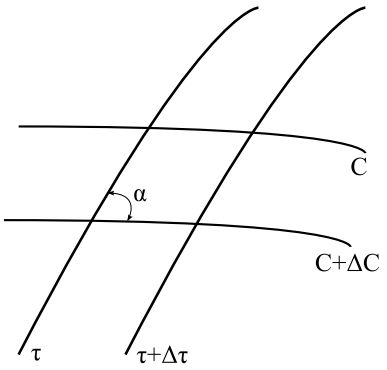

Figure 11: Typical co-ordinate lines for the orbit co-ordinates (C, τ)

Eqn. (36) is the 'Jeffery's advection equation' and yields no information about the relative populations of different orbits. Hence, the original eqn. (35) was re-examined to consider the consequences of the action of a small amount of weak anisotropic diffusion, in the limit as $t \to \infty$. The drift velocity, $\mathbf{p}^h$, has been neglected, and eqn. (35) was integrated over a singly connected domain, A, on the unit sphere, where the function, Ω, is defined. Then applying the 'divergence theorem' over the closed Jeffery's orbit as the bounding curve, along which $\dot{\mathbf{p}}^J \cdot \hat{\mathbf{n}} = 0$, where $\hat{\mathbf{n}}$ is the outward normal to the bounding curve, the following equation was obtained at steady-state [96, 97]:

$$\mathbf{D}^r : \int_l \hat{\mathbf{n}} \nabla_p \Omega \, dl = 0 \tag{37}$$

Here the components of the diffusivity tensor are assumed to be constant. Eqn. (37) states that the net flux of fibers across an orbit is zero at the steady-state and permits determination of the steady-state orbit constant distribution. In particular, eqn. (37) is applicable for a weak diffusion, provided that as $\mathbf{D}^r$ becomes small, other effects such as fluid inertia, and fiber–fiber interactions do not become of equal importance. For convenience, the (θ, ϕ) co-ordinates on the unit sphere were transformed to the more natural orbit co-ordinates (C, τ), where τ is the phase angle equal to $\tan^{-1}\left(\frac{1}{r_e}\tan\theta\right)$. The co-ordinate lines $C = const.$ and $\tau = const.$, though still on the unit sphere, are not orthogonal as shown in figure 11, where angle α defines the

skewness of the co-ordinate lines. Now the orientation distribution can be separated into two parts, such as:

$$\Omega\left(C,\tau\right)=f\left(C\right)g\left(C,\tau\right) \tag{38}$$

In this expression $f\left(C\right)$ is the unknown distribution function describing the population amongst the Jeffery orbits; $g\left(C,\tau\right)$ is the distribution around an individual orbit, C. Now the solution of eqn. (36) is subject to the condition of eqn. (37). Applying eqn. (37) in the (C,τ) co-ordinate system, and in the large aspect-ratio limit, the integral expression for $f\left(C\right)$ was analytically solved to yield:

$$f\left(C\right)=\frac{RC}{\pi\left(4RC^{2}+1\right)^{3/2}} \tag{39}$$

where $R{=}\left(\frac{D^{r}_{\theta\theta}}{D^{r}_{\phi\phi}}\right)$. $D^{r}_{\theta\theta}$ is the proportionality between gradients of $\Omega\left(\theta,\phi\right)$ in the θ-direction and the flux of probability in the θ-direction. A large value of R implies that the fibers are aligned near the vorticity axis, as the effect of $D^{r}_{\theta\theta}$ is to push fibers away from the flow direction, and push toward vorticity or toward decreasing values of orbit constant. Rahnama et al. [97] proved that the off-diagonal elements of the diffusivity tensor, $D^{r}_{\theta\phi}$, and $D^{r}_{\phi\theta}$, do not affect the final orientation distribution function. The effect of this weak anisotropic diffusion on the orbit distribution is schematically portrayed in figure 12. The steady-state orbit constant distribution can be presented as a differential probability distribution function, $p\left(C_{b}\right)$, such that the probability of finding any particular fiber with C_{b} in the interval $[C_{b},C_{b}+dC_{b}]$ is $p(C_{b})dC_{b}$. Eqn. (39) can be transformed to give:

$$p\left(C_{b}\right)=\frac{4RC_{b}}{\left\{4R\left[C_{b}/(1-C_{b})\right]^{2}+1\right\}^{3/2}\left(1-C_{b}\right)^{3}} \tag{40}$$

where $\int_{0}^{1}p\left(C_{b}\right)dC_{b}\equiv 1$. Eqn. (40) is referred to as the anisotropic weak diffusivity model 'A.W.D.M.' in this work. The trend of R, in the semidilute regime can be investigated, by fitting the model with different C_{b}-distributions, by varying the suspension concentration and the fiber aspect-ratio.

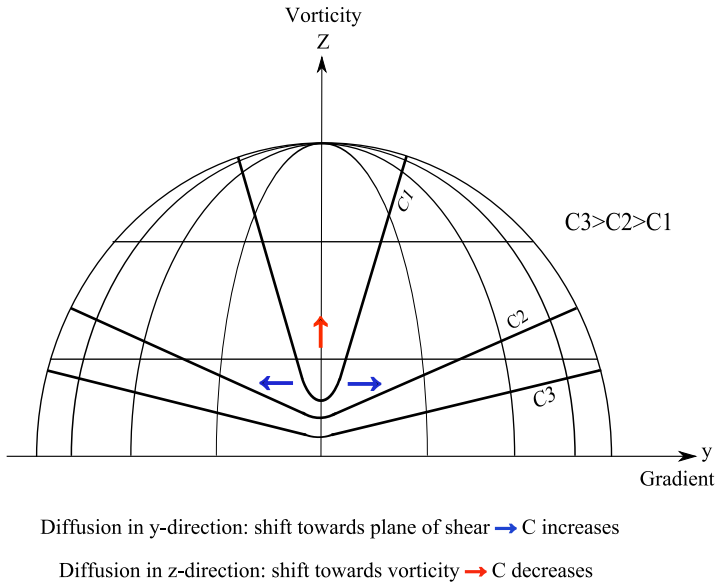

Figure 12: Schematic diagram illustrating the position of the end of the fiber and the effect of diffusion on the orbit distribution.

A nonlinear least-square (non-linear data fitting) problem is solved in this research to perform the one-parameter fit of the anisotropic diffusivity model, eqn. (40), to the simulated C_b-distribution. Rather than finding the value $f(x)$ (the sum of squares), this non-linear least-square method requires the user-defined function [in our case eqn. (40)] to compute the *vector*-valued function:

$$F(x) = \begin{bmatrix} f_1(x) \\ f_2(x) \\ \vdots \\ f_m(x) \end{bmatrix}$$

Then in vector terms, this optimization problem is restated as:

$$\min_x \frac{1}{2} \|F(x)\|_2^2 = \frac{1}{2} \sum_i f_i(x)^2$$

where x is a vector, and $F(x)$ is a function that returns a vector value. This is known as the LevenbergMarquardt algorithm (LMA) [81], which provides a numerical solution to the problem of minimizing a function, generally nonlinear, over a space of parameters of the function. The LMA algorithm was obtained from the MATLAB®

Function Optimization Toolbox™ with *quadcubic* (a safeguarded mixed quadratic and cubic polynomial interpolation and extrapolation method) linesearch to produce a best fit value of diffusivity ratio, $R\left(\frac{D^r_{\theta\theta}}{D^r_{\phi\phi}}\right)$.

To determine the diffusivity ratio, R, in the semidilute regime, Stover et al. fitted the 'A.W.D.M.', eqn. (40), to their experimental C_b-distribution with R as an adjustable parameter. They also fitted the 'A.W.D.M.' to Anczurowski & Mason's [9] dilute experimental C_b-distribution. The fibers with r_p=18.4 for Anczurowski & Mason's experiment show a plateau at about $\left(\frac{D^r_{\theta\theta}}{D^r_{\phi\phi}}\right)$ =17 for the apparent dilute regime (nL^3=0.016, 0.066). But a steep drop to another plateau, at about $\left(\frac{D^r_{\theta\theta}}{D^r_{\phi\phi}}\right)$ =1.5, was observed for Stover et al.'s semidilute regime experiments.

Rahnama et al. [97] theoretically studied the orientation diffusivity in dilute to semidilute regimes with 'hydrodynamic interaction theory'. In this hydrodynamic theory, orientation diffusivity was obtained from an ensemble average of the hydrodynamic fiber–fiber interactions. The steady-state fiber orientation distribution is controlled by the anisotropy and the orientation dependence of the diffusivity. The steady-state and transient fiber orientation distributions are derived using a perturbation analysis for weak hydrodynamic orientation diffusion. For computational convenience, Rahnama et al. fitted the 'A.W.D.M' to the C_b-distribution calculated with 'hydrodynamic interaction theory', and obtained the best-fit value of R. Rahnama et al. used an iterative solution with an initial guess of R (averaged R=2.4 from Stover et al.'s experiments, for r_p=31.9 was used as an initial guess) to calculate the C_b-distribution with this theory.

Table 1 summarizes R=$\left(\frac{D^r_{\theta\theta}}{D^r_{\phi\phi}}\right)$ values from Stover et al.'s [115] experiments, from 'hydrodynamic interaction theory' and from the LBM–EBF simulations. The R values in the semidilute regime, from $nL^3 = 1-45$, fall in the same range for the theory and the experiments. The quantitative comparison between the LBM–EBF simulations and the experiments are good, considering statistical uncertainties in the experiments.

Table 1: Comparison of the diffusivity ratio, $R\left(\frac{D^r_{\theta\theta}}{D^r_{\phi\phi}}\right)$

nL^3	Stover's experiment $r_p = 31.9$	Hydrodyn. Interaction Theory $r_p = 31.9$	LBM–EBF simulation $r_p = 32.0$
45	3.16	2.55	2.58
18	1.38	3.12	3.31
10	2.85	3.50	2.86
5	2.18	3.50	2.45

However, Stover et al.'s experimental values of R do not show any systematic dependence on the volume concentration, nL^3, and aspect-ratio, r_p. Whereas, the theory reveals a dependence of diffusivity ratio, R, on nL^3, and aspect-ratio, r_p in a way that, for a fixed aspect ratio ($r_p = 31.9$), the value of R decreases with increasing nL^3. Physically this means that the fibers shift closer toward the flow direction with increasing nL^3. According to Rahnama et al. this shift resulted from the anisotropic hydrodynamic screening incorporated in the renormalized Green's function derived by Shaqfeh & Fredrickson [104]. The LBM–EBF predicted R values first increase slightly from $nL^3 = 5 - 18$, and then decrease with increasing concentration, following the theoretical prediction. The physical reason behind this can be explained by studying the change of $\langle C_b \rangle$ values with the change of concentration.

From figure 13 it is seen that the $\langle C_b \rangle$ values for the Stover et al. experiments and the LBM–EBF simulations decrease with increase of nL^2d. Physically this means the fibers are shifting towards the vorticity axis, and as a result the R value also increases (diffusion occurring primarily in flow-vorticity plane) with concentration. But as the concentration increases more ($nL^3 > 18$ or $nL^2d \gtrsim 0.56253$)), the fiber–fiber hydrodynamic interactions dominate, and also there can be presence of some mechanical contacts among fibers. Both of these effects cause extra fiber flipping, and as a result the fibers move closer to the flow direction ($\langle C_b \rangle$ increases) and the diffusivity ratio R

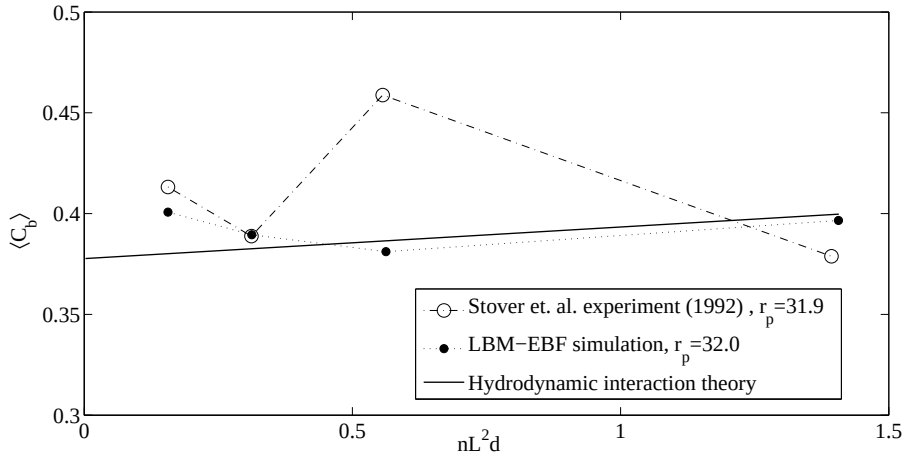

Figure 13: Average value of orbit constant, $\langle C_b \rangle$, as a function of nL^2d. The prediction of 'hydrodynamic interaction theory' is indicated with a solid line.

decreases (i.e. diffusion occurring primarily in the flow-gradient plane). So the $\langle C_b \rangle$ values from Stover et al.'s experiments, from the 'hydrodynamic interaction theory' and from the LBM–EBF simulations fall close to each other for higher values of concentration, as observed, for example, at the concentration $nL^3 = 45$ ($nL^2d \approx 1.41$). Now the apparent discrepancy between the theory and the experiments at low concentrations can be due to the lower accuracy of renormalized Green's function at low concentrations (which is used to account for hydrodynamic screening in 'hydrodynamic interaction theory'). Actually that function shows better accuracy at higher values of nL^3 [104]. Perhaps at lower concentrations, a two-fiber theory would work better. On the flip-side, through a private communication with Professor Koch at Cornell University, the authors were informed that during Stover et al.'s [115] experiments, that group of researchers did not pay much attention to these trends of diffusivity ratio, R. Not being too sure about the statistical significance of the trends, they rather paid more attention just to the overall range of values of the diffusivity ratio, R. So it is encouraging that the LBM–EBF simulations produced physically explainable results of the trend of R and in addition verified its range in the semidilute suspension for non-colloidal rigid fibers.

4.4 ϕ distribution

In § 4.2 it has been demonstrated that the 'A.W.D.M.' adequately described the orbit constant distribution. But it is also important to investigate the ϕ-distribution and its relation to the 'A.W.D.M.' model. Although the model predicts the C_b-distribution with good accuracy, the ϕ-distribution may not be described by it, since fiber–fiber hydrodynamic interactions affect these two distributions differently. A weak rotary diffusivity can affect the C_b-distribution, but the ϕ-distribution is unchanged by a weak rotary diffusivity, since the diffusivity in the ϕ-direction is dwarfed by the Jeffery's convective term in that direction. The orientation dispersion in the semidilute regime may be investigated by comparing the probability distribution, $p(\phi)$, in that regime to the $p(\phi)$ for an isolated fiber in fluid, given by the Jeffery's solution. According to Anczurowski & Mason [8], the orientation probability distribution for the angle ϕ for an isolated fiber is given by:

$$p(\phi) = \frac{r_e}{\pi \left(r_e^2 \cos^2 \phi + \sin^2 \phi \right)} \tag{41}$$

where $0 < \phi < \pi$. The ϕ-distribution must be symmetric about the flow direction ($\phi = \pi/2$), if all the particle–particle interactions are hydrodynamic. The argument follows from the form of the *N-particle Smoluchowski equation*, and is similar to that given by Koch [64] for the pair probability in a suspension of spheres. The quantities $\mathbf{U}_i$ (the velocity of the ith particle) and $\boldsymbol{\omega}_i$ (angular velocity of the ith particle) are linear with shear rate, $\dot{\gamma}$, so the probability of a certain configuration is unchanged if the flow is reversed. Therefore, the ϕ-distribution must be symmetric upon reflection through the xz-plane. However, Stover [113] found that, most of the peaks of the ϕ-distributions experienced a slight shift from the x-direction ($\phi = \pi/2$) to the upstream direction, i.e., to a value of ϕ less than $\pi/2$. But they were unable to determine the source of this apparent shift.

Similar to procedure followed in measuring the C_b-distributions from the LBM–EBF data, the probability distributions, $p\,(\phi)$, are also calculated at a specific timestep. The angle, ϕ, can vary between 0 to π. So the total range of ϕ is divided into n number of bins, where $\sum_{i=1}^{n} d\phi(i) = \pi$. As before, the probability that a fiber will have a ϕ angle within the range $[\phi(i) < \phi < \phi(i) + d\phi]$ is: $p\,(\phi) = \frac{no.\ of\ fibers\ in\ \phi(i)}{total\ no.\ of\ fibers}$. The $p(\phi)$ is normalized with the integral area under the histogram.

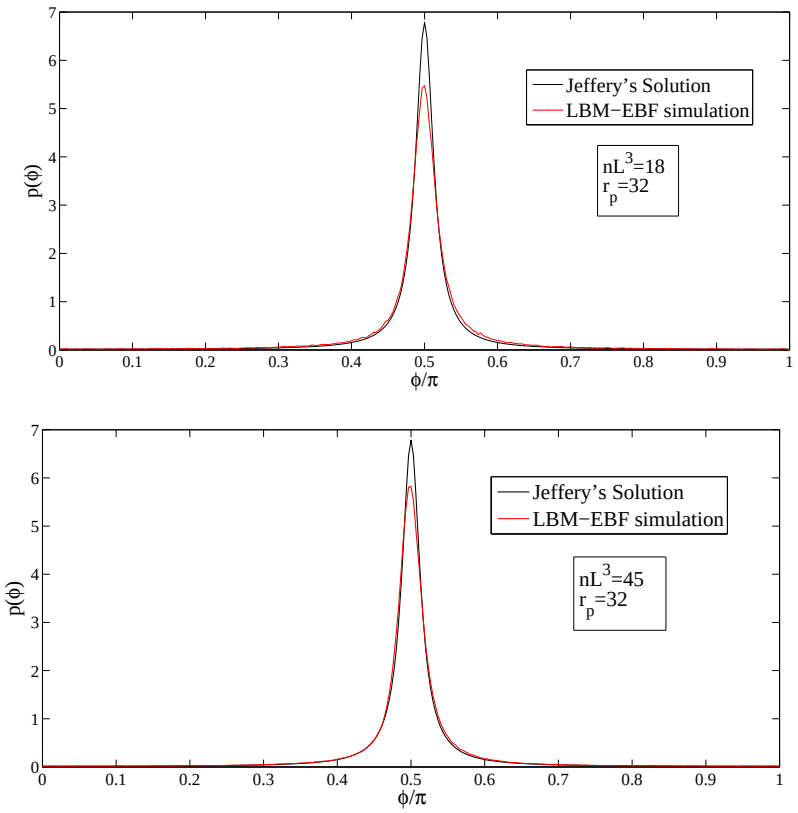

Figure 14: Comparison of Jeffery's ϕ-distribution (eqn. (41)) for an isolated fiber to the LBM–EBF simulated ϕ-distributions for suspensions with (top figure) fibers of aspect-ratio $r_p = 32$ at $nL^3 = 18$; and (bottom figure) fibers of aspect-ratio $r_p = 32$ at $nL^3 = 45$, respectively.

The ϕ-distributions in figure 14 are demonstrations of the fact that spreading of $p(\phi)$ occurs due to a diffusion-like process, which favors low gradients of the ϕ-distribution function in the semidilute regime. The fibers are nearly aligned in the flow direction, but slight shifts of the peaks of $p(\phi)$ are observed as compared to the

symmetric Jeffery's solutions.

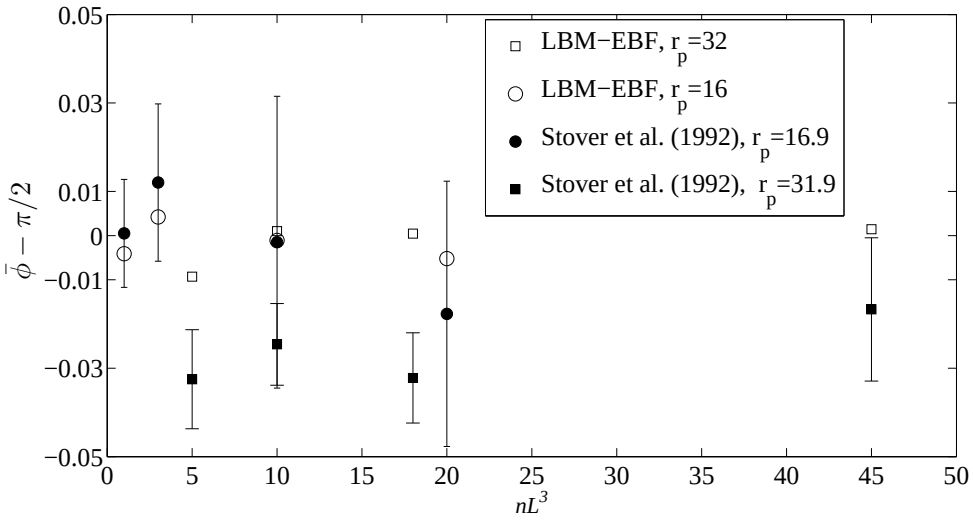

Figure 15: The shift of mean angle of ϕ-distribution as a function of nL^3 for different aspect-ratio fibers. The error bars indicate a 80% confidence interval for the experiments.

Figure 15 quantifies these shifts of mean angles of ϕ from the flow direction, ($\phi = \pi/2$) observed in experiments of Stover et al. [115] and in the LBM–EBF simulations for different aspect-ratio fibers with increasing nL^3. The finite values of $(\langle\phi\rangle - \pi/2)$ in figure 15 prove that Stokes flow symmetry is being violated in the semidilute regime. It can be argued that, since hydrodynamic interactions can not cause deviation from the symmetry of the ϕ-distribution, there must be some non-hydrodynamic effects present in the semidilute regime. In most of the experiments of Stover et al., slight upwind shifts of the peaks of the ϕ-distributions were observed, while some occasional cases of forward shifts were noted too. For example, in figure 15, the experimental cases of $nL^3 = 1$ or 3 with r_p=16.9 demonstrate this observation. In the LBM–EBF simulation, any particular trend for the shift is not visible either. The most probable reason for this non-systematic behavior is that, since the angular velocity is at a minimum when a fiber is aligned with the flow direction, it has an equal probability of being *bumped* forward, where the angular velocity would increase, or

being *bumped* backward, where it still would pass through the aligned orientation state. But certainly these shifts of peaks from the flow direction indicate that a complete description of hydrodynamic interactions is more complex and sophisticated than a weak diffusion in the simple 'A.W.D.M.' can provide. Although the model was very good in describing $p(C_b)$ it can not describe the asymmetry in $p(\phi)$.

CHAPTER V

EVOLUTION OF FIBER ORIENTATION MOMENTS WITH ROTATIONAL DIFFUSION MODELS

This chapter continues the analysis of rotational diffusion of non-colloidal fibers in a simple shear flow. This is a component of the overall effort to predict changes in the magnitudes of different directional diffusivities of a rotational diffusion process with changes of c_v and r_p.

The evaluations are made with a combined use of fiber orientation information from the LBM–EBF simulation data and an appropriate rotational diffusion model. In § 4, the 'A.W.D.M.' model has produced a sense of directional diffusivity through the diffusivity ratio, R. But the model can not estimate magnitudes of different components of an anisotropic rotational diffusivity tensor. A more rigorous anisotropic diffusivity model, in a three dimensional spatial tensorial form (we denote that tensorial form with the symbol, $\mathbf{C}$, in this research) is required to satisfy that inquiry. The results in this chapter first address this issue.

In addition, to test the performance of an appropriate rotational diffusion model into a fiber orientation evolution equation is significant for studying the behavior of fiber orientation moments. For example, in the fiber-reinforced industry today, the evolution equation is solved to predict the fiber orientations in different directions. Almost all commercial software programs for fiber-reinforced molding processes, such as for the injection molding process, are yet to be developed based on fiber-level simulation methods, and these programs solve the fiber orientation evolution equation. The diffusion mechanism in the evolution equation is usually represented by a phenomenological model. Closure approximations are indispensable to solve the

evolution equation.

To date, the widely used form of the evolution equation is called the 'Standard Folgar–Tucker model' [43], and it includes an isotropic diffusion. The Folgar–Tucker model family has been implemented in almost all commercial software programs for injection molding process simulation. Now some of the limitations of this Folgar & Tucker [43] proposed isotropic diffusivity was discussed in § 2.3; it also poses certain limitations when being used in the evolution equation. Folgar and Tucker supplemented the Jeffery's rotation rate for a fiber in a Newtonian fluid with an isotropic, orientation diffusivity. The Folgar–Tucker formulation correctly prescribes the orientation diffusivity to be proportional to a scalar measure of the velocity gradient. However, an empirical constant is used as a fitting parameter in the expression for diffusivity, and the constant needs to be estimated for each new composite molding experiment. It has been observed that, with an isotropic diffusivity in the evolution equation it is not possible to predict and tune all the orientation moment components simultaneously within reasonable accuracy [15, 92]. So several researchers [65, 89, 92] have proposed to include a orientation-state dependent, anisotropic diffusivity in the evolution equation.

The author wants to emphasize the fact that, in solving the evolution equation, the LBM–EBF simulation plays no part. But to reiterate, in the fiber-reinforced composite industry, solving for the evolution equation is a widely practiced method to predict fiber orientation moments; and thus monitoring the performance of an anisotropic diffusivity model in that equation certainly is important. This is why the solution of the fiber orientation moments with an anisotropic diffusion model being employed in the evolution equation is studied in this chapter. It should be noted that the orientation moments that the evolution equation solves for, can effectively be calculated with the prospective LBM–EBF simulation in a direct way. The author discusses that scope to close this chapter.

We would first cover some background on fiber structure in suspension which would lead to a more elaborate discussion on the solution of the evolution equation.

5.1 Characterization of the fiber structure in suspensions

The orientation of a single, straight fiber is characterized by two angles θ and ϕ in a spherical coordinate system, or by a unit vector $\mathbf{p}$ directed along the fiber axis. A sensible assumption to characterize macroscopic properties of suspensions is to consider a volume with dimension much smaller than the characteristic dimension of the flow field, yet the volume should be much larger than the size of the suspended particles. Across this volume, there are supposed to be no obvious changes of statistical properties of the suspension. But usually for fiber suspensions, the fiber length is of the order of mm. So the above assumption seems difficult to satisfy, since the volume containing large number of fibers cannot be looked at as a *macroscopic point*. However, studies of fiber orientation and rheology of fiber suspension are usually done in the uniform bulk flow fields in which suspension properties are independent of the position in the flow fields. Therefore, a volume exists that contains a large number of fibers and over which the macroscopic properties are uniform.

With the application of statistical mechanics, The motion of fibers can be treated as a stochastic process. The macroscopic quantities of the suspension can be obtained in terms of the ensemble average of the relevant microscopic quantities, for example, for a physical tensor, $\boldsymbol{\mathcal{H}}(\mathbf{p})$:

$$\langle \boldsymbol{\mathcal{H}} \rangle = \oint \boldsymbol{\mathcal{H}} \Omega (\mathbf{p}) \, d\mathbf{p} \tag{42}$$

where $\langle \boldsymbol{\mathcal{H}} \rangle$ is a macroscopic value of $\boldsymbol{\mathcal{H}}$, and for a collection of fibers, the complete description of orientation is the probability distribution function, $\Omega (\mathbf{p})$.

A useful property for fiber suspensions is the structure tensors of fibers, which are

the moment tensors of $\mathbf{p}$. When $\boldsymbol{\mathcal{H}} = \mathbf{p} \cdots \mathbf{p}$, the n-th structure tensor is:

$$\left\langle \underbrace{\mathbf{p} \cdots \mathbf{p}}_{n} \right\rangle = \oint \underbrace{\mathbf{p} \cdots \mathbf{p}}_{n} \Omega\left(\mathbf{p}\right) \, d\mathbf{p} \tag{43}$$

Advani & Tucker [1] showed that, a general and concise way to describe orientation is to use the second-order orientation tensor, $\mathbf{A}$ which has components:

$$A_{ij} = \langle p_i p_j \rangle \tag{44}$$

The angle brackets denote an average over all fibers in an unbiased sample. Alternately, the angle brackets denote an average over all directions, weighted by the probability distribution function, Ω. This is given by:

$$\mathbf{A} = \langle \mathbf{pp} \rangle = \oint \Omega \mathbf{pp} \, d\mathbf{p} \tag{45}$$

Here, $\oint d\mathbf{p}$ denotes an integral over all orientations at a given location, and $\mathbf{pp}$ is the dyadic (tensor) product of the orientation vector with itself. Similarly, the fourth-order orientation moment, $\mathbb{A}$, and sixth-order orientation moment, $\mathcal{A}$, can be written as:

$$\mathbb{A} = \langle \mathbf{pppp} \rangle = \oint \Omega \ \mathbf{pppp} \, d\mathbf{p} \tag{46}$$

$$\mathcal{A} = \langle \mathbf{pppppp} \rangle = \oint \Omega \ \mathbf{pppppp} \, d\mathbf{p} \tag{47}$$

By its definition, the second-order orientation moment is symmetric ($A_{ij} = A_{ji}$) or ($\mathbf{A} = \mathbf{A}^{\mathsf{T}}$), and has a unit trace ($A_{ii} = 1$) or ($tr\mathbf{A} = 1$). The symmetry of $\mathbf{A}$, allows this tensor to be rewritten in contracted form as:

$$\mathbf{A} = \left\{ \begin{array}{c} A_{11} \\ A_{22} \\ A_{33} \\ A_{23} \\ A_{31} \\ A_{12} \end{array} \right\} \tag{48}$$

This is convenient for computational storage when the evolution equation is solved. The higher-order tensors, $\mathbb{A}$, and $\mathcal{A}$, are also noted to be completely symmetric [58]. In addition, higher-order orientation tensors completely describe lower-order orientation tensors [1].

5.2 Evolution equation for Ω and $\dot{\mathbf{A}}$

In § 2.3, the concept of the orientation distribution function, Ω, is introduced. The orientation distribution function, Ω, is normalized over all orientations; it needs to satisfy:

$$\oint \Omega \; d\mathbf{p} = 1 \tag{49}$$

where $\oint d\mathbf{p}$ denotes an integral over the orientation space. Thus, the orientation distribution is conserved, and the orientation probability distribution function must satisfy a continuity equation, or Fokker–Planck type equation for Ω. This continuity equation is given by:

$$\frac{D\Omega}{Dt} = -\nabla_p \cdot (\Omega \dot{\mathbf{p}}) \tag{50}$$

where $\dfrac{D}{Dt}$ is the material derivative operator in Cartesian coordinates, ∇_p is the surface gradient operator in orientation space, and $\Omega\dot{\mathbf{p}}$ is the probability flux.

5.3 Evolution equation (Standard Folgar–Tucker model) with isotropic diffusion

The kinetics of the orientation distribution function Ω is governed by eqn. (50). Folgar & Tucker [43] built on this conservation equation by decomposing the probability flux term $\Omega\dot{\mathbf{p}}$ into a hydrodynamic contribution $\Omega\dot{\mathbf{p}}^J$ and a diffusive flux vector $\mathbf{q}^d$, giving:

$$\frac{D\Omega}{Dt} = -\nabla_p \cdot \left(\Omega\dot{\mathbf{p}}^J + \mathbf{q}^d\right) \tag{51}$$

The hydrodynamic contribution is responsible for the orientation kinetics for fibers in dilute suspension. Typically, the hydrodynamic contribution is modeled by the Jeffery-Ericksen equation, eqn. (1), for particle motion in a dilute suspension. But

with the increase of suspension concentration, fiber–fiber contacts also increase, causing deviations from the orientation states observed in non-concentrated suspensions. The diffusive flux vector represents a phenomenological way to account for these deviations [43].

In order to model the diffusive flux vector $\mathbf{q}^d$ in eqn. (51), Folgar & Tucker suggested the phenomenological relationship:

$$\mathbf{q}^d = -\mathsf{C}_I \dot{\gamma} \nabla_p \Omega \tag{52}$$

where C_I is the fiber–fiber interaction coefficient (a fitting parameter), and $\dot{\gamma} = \sqrt{(2\mathbf{E} : \mathbf{E})}$ is the scalar magnitude of strain-rate tensor, $\mathbf{E}$. In this model, Folgar & Tucker assumed that the rate of fiber–fiber collisions is proportional to $\dot{\gamma}$; and the orientation perturbation per collision is independent of $\dot{\gamma}$. To determine C_I, Folgar & Tucker [43] measured the probability distribution function in steady Couette flow. Then they solved eqn. (51), for the distribution function with various C_I in steady shear flow to fit the experimental distribution.

Determining the orientation state by solving the evolution equation for probability distribution function, Ω is quite cumbersome since, $\Omega(\mathbf{r}_c, \mathbf{p}, t)$ has six independent variables in the 3D case. As such, the orientation moment, $\mathbf{A}$, is the quantity actually calculated in predictive-engineering models of fiber orientation, and it is the preferred way[1] to report orientation data.

[1]The primary reason for using $\mathbf{A}$ instead of Ω to describe orientation comes from the numerical simulation of fiber orientation in complex flows, which asks for costly, intensive calculation should the evolution of Ω be monitored. It is computationally more efficient to track the components of $\mathbf{A}$ over multiple time steps and many spatial nodes, than it is to track the distribution function Ω over the same discretization. Besides saving computational cost, the second-order orientation tensor $\mathbf{A}$ offers other advantages as well [1, 121]. It is independent of the choice of the co-ordinate system, and it also easily transforms between co-ordinate systems; it requires no assumptions about the nature or symmetry of the probability distribution function Ω ; it can be measured by direct experiments; and nonetheless, it can be used to predict the effect of orientation on material properties.

Advani & Tucker [1] took the material derivative of eqn. (45) and substituted the governing equation for Ω [utilizing eqn. (1), eqn. (51) and eqn. (52)] on the right-hand side and integrated by parts. The result after some simplifications produces a time evolution equation for the second-order tensor $\mathbf{A}$. This is the standard Folgar–Tucker model:

$$\dot{\mathbf{A}} = \underbrace{(\mathbf{W}\cdot\mathbf{A} - \mathbf{A}\cdot\mathbf{W}) + \lambda\,(\mathbf{E}\cdot\mathbf{A} + \mathbf{A}\cdot\mathbf{E} - \mathbf{2}\mathbb{A} : \mathbf{E})}_{hydrodynamic\ contribution,\ \dot{\mathbf{A}}^J} + \underbrace{2\mathsf{C}_I\dot{\gamma}\,(\mathbf{I} - 3\mathbf{A})}_{diffusive\ contribution,\ \dot{\mathbf{A}}^d} \tag{53}$$

In this model, $\dot{\mathbf{A}}$ represents the material derivative of $\mathbf{A}$, $\mathbf{I}$ is the identity tensor, and $\mathbb{A}$ is the fourth-order orientation tensor defined by eqn. (46).

The interaction term $\dot{\mathbf{A}}^d$ is a rotary diffusion term. It provides an isotropic flux that pulls fibers toward a random state, defined by $\mathbf{A} = \mathbf{I}/3$. Hence, the diffusive contribution to orientation kinetics goes to zero for a random orientation state. The Folgar–Tucker model allows the control of the steady-state fiber orientation through the magnitude of C_I, but the rate of fiber reorientation is still dominated by the flow field for typical values of C_I, in the range of $0.016 \sim 0.0001$, as reported by Bay [13].

5.4 Evolution equation with an anisotropic rotational diffusion

The accuracy of the hydrodynamic contribution, $\dot{\mathbf{A}}^J$, in the standard Folgar–Tucker model has typically been agreed upon, and the need for a diffusive contribution in semidilute to concentrated suspensions is readily acknowledged. However, the means of selecting the parameters used to model the diffusive contribution, and even the form of this contribution itself, are still not well-developed. Below, the noteworthy anisotropic diffusion models are introduced, accompanied by a discussion of their implementation in the evolution equation.

5.4.1 Evolution equation with Phan-Thien's model

A modification to the Folgar–Tucker isotropic rotary diffusion model was proposed by Fan et al. [40], and it was updated with some corrections by Phan-Thien et al. [89]. This group of researchers performed direct numerical simulations of multiple interacting fibers in a concentrated suspension undergoing simple shear flow. Fan et al.'s attempt to fit the calculated steady-state orientation distribution using the Folgar–Tucker model was unsuccessful. Consequently, they developed a rotary diffusion model, starting from describing the motion of a fiber in the suspension, under the action of hydrodynamic and random forces by the Langevin's equation. The scalar interaction coefficient, C_I, was replaced by a second order tensor $\mathbf{C}$. This makes the rotary diffusion anisotropic. At steady-state the proposed form of $\mathbf{C}$ by Fan et al. looks like:

$$\begin{aligned}&\dot{\gamma}\left(2\mathsf{C}_{ij}-3\mathsf{C}_{ik}\langle p_k p_j\rangle-3\langle p_i p_k\rangle\mathsf{C}_{kj}\right)\\&=\frac{1}{2}\left(W_{ik}\langle p_k p_j\rangle-\langle p_i p_k\rangle W_{kj}\right)-\frac{1}{2}\lambda\left(E_{ik}\langle p_k p_j\rangle\ +\langle p_i p_k\rangle E_{kj}-2E_{kl}\langle p_l p_k p_i p_j\rangle\right)\end{aligned}\tag{54}$$

Eqn. (54) contained an error such that it could not guarantee $\dfrac{D}{Dt}\langle \mathbf{p}\cdot\mathbf{p}\rangle = 0$ at all times. Phan-Thien et al. [89] tried to correct this error and proposed a slightly modified form of spatial tensor $\mathbf{C}$ for steady-state as follows: $\mathbf{C}$:

$$\begin{aligned}&\dot{\gamma}\left(2\mathsf{C}_{ij}-3\mathsf{C}_{ik}\langle p_k p_j\rangle-3\langle p_i p_k\rangle\mathsf{C}_{kj}-2\langle p_i p_j\rangle\mathsf{C}_{kk}+6\mathsf{C}_{kl}\langle p_l p_k p_i p_j\rangle\right)\\&=\frac{1}{2}\left(W_{ik}\langle p_k p_j\rangle-\langle p_i p_k\rangle W_{kj}\right)-\frac{1}{2}\lambda\left(E_{ik}\langle p_k p_j\rangle\ +\langle p_i p_k\rangle E_{kj}-2E_{kl}\langle p_l p_k p_i p_j\rangle\right)\end{aligned}\tag{55}$$

Six components of the tensor $\mathbf{C}$ can be determined using eqn. (55), once all components of moment tensors are obtained from sample data. Phan-Thien et al. [89] proposed to replace the standard Folgar–Tucker $\dot{\mathbf{A}}^d$ in eqn. (53) with:

$$\dot{\mathbf{A}}^d = \dot{\gamma}\left[2\mathbf{C}-2\ \mathrm{tr}(\mathbf{C})-3\left(\mathbf{C}\cdot\mathbf{A}+\mathbf{A}\cdot\mathbf{C}\right)+6\mathbb{A}:\mathbf{C}\right]\tag{56}$$

This model does satisfy the symmetry requirement on $\dot{\mathbf{A}}$ and maintains $\mathrm{tr}\mathbf{A}=1$.

It must be noted that Phelps & Tucker [92] with their own preliminary calculation using eqn. (56), observed unrealistic behavior and discovered some inconsistencies in the Phan-Thien model. Even though Phan-Thein et al. [89] performed some corrections on the previous version of the model by Fan et al. [40], the Phan-Thien model still incorrectly showed a non-zero diffusive flux and a non-zero diffusive contribution ($\dot{\mathbf{A}}^d \neq 0$) to the evolution equation at the isotropic orientation state. In other words, for a general $\mathbf{C}$, when the fibers are randomly distributed, the diffusion term of this model would pull the orientation away from isotropy. Also, there was an error in their method of projecting the spatial tensor, $\mathbf{C}$, onto the orientation space. Phelps & Tucker [92] corrected these irregularities in their proposed general 'ARD' model.

5.4.2 Evolution equation with Phelps & Tucker's General 'ARD' model

Phelps & Tucker [92] built on Phan-Thien's approach by exploring the dynamic properties of the moment-tensor equation. Their model focuses especially on composites with long discontinuous fibers known as the long fiber thermoplastics or LFTs (typical length of LFTs are $\mathcal{O}(1)$ mm after fiber attrition in the mold).

Phelps & Tucker pointed out that the derivations of Fan et al. [40] and Phan-Thien et al. [89] do not draw a clear distinction between spatial quantities (such as $\mathbf{p}$ and $\mathbf{C}$) and surface quantities in the orientation space (such as ∇_p or $\mathbf{q}^d$). Phelps & Tucker [92] corrected this problem by developing an evolution equation ('ARD' model) that incorporates a proper two-dimensional understanding of rotary diffusion. Advani & Tucker [1] implicitly stated the two-dimensionality of $\dot{\mathbf{p}}^J$, $\mathbf{q}^d$ and ∇_p when they built on the decomposed form of the continuity equation, eqn. (51), to develop the expression for $\dot{\mathbf{A}}$, eqn. (53). Phelps & Tucker [92] considered a two-dimensional rotary diffusivity surface tensor, denoted by $\mathbf{D}^r$ defined in surface spherical coordinates in their proposed 'ARD' model. The diffusive flux vector $\mathbf{q}^d$ for the 'ARD model' is

then:

$$\mathbf{q}^d = -\dot{\gamma}\ \mathbf{D}^r \cdot \nabla_p \Omega \tag{57}$$

In passing, we point out that the author has derived the projected form of diffusivity, $\mathbf{D}^r$ in a 2-dimensional surface coordinate system from its 3-dimensional spatial form, C in global Cartesian co-ordinates in Appendix A.

With some assumptions and algebraic simplifications, Phelps and Tucker's general 'ARD' model is written as:

$$\begin{aligned}\dot{\mathbf{A}} = &(\mathbf{W}\cdot\mathbf{A} - \mathbf{A}\cdot\mathbf{W}) + \lambda\,(\mathbf{E}\cdot\mathbf{A} + \mathbf{A}\cdot\mathbf{E} - \mathbf{2}\mathbb{A} : \mathbf{E}) \\ &+ \dot{\gamma}\,[2\mathsf{C} - 2(\text{tr }\mathsf{C})\mathbf{A} - 5(\mathsf{C}\cdot\mathbf{A} + \mathbf{A}\cdot\mathsf{C}) + 10\mathbb{A} : \mathsf{C}]\end{aligned} \tag{58}$$

Phelps & Tucker's [92] expression for C was especially modeled for long discontinuous fibers. They made simplifying assumptions to keep their model tractable but maintained the objectivity of C by assuming $\mathsf{C} = \mathsf{C}\,(\mathbf{E}, \mathbf{A})$ which also makes $\dot{\mathbf{A}}^d \propto \dot{\gamma}$. Phelps & Tucker's expression for C is adjustable through five scalar constraints, b_{1-5} and is given by:

$$\mathsf{C} = b_1\mathbf{I} + b_2\mathbf{A} + b_3\mathbf{A}^2 + \frac{b_4}{\dot{\gamma}}\mathbf{E} + \frac{b_5}{\dot{\gamma}^2}\mathbf{E}^2 \tag{59}$$

5.4.3 Evolution equation with Koch model

Koch [65] developed a mechanistic rotary diffusion model in semidilute to semiconcentrated fiber suspensions, taking into account long-range hydrodynamic interactions only. In the Koch model, the anisotropic diffusivity scales with the rate of deformation (as does the Folgar–Tucker isotropic diffusivity), and it also varies with the orientation state. Koch [65] created a general objective model for spatial tensor, C, by requiring that $\mathsf{C} = \mathsf{C}\,(\mathbf{E}, \mathbf{A}, \mathbb{A}, \mathcal{A})$. Where, $\mathbf{A}$, $\mathbb{A}$ and $\mathcal{A}$ are second, fourth and sixth-order orientation moments defined by eqn. (45), eqn. (46) and eqn. (47) respectively. Now using notation of our work, the tensor C for Koch model is given by:

$$\mathsf{C} = \frac{nL^3}{\dot{\gamma}^2 \ln^2 r_p}\left[\beta_1\,(\mathbf{E} : \mathbb{A} : \mathbf{E})\,\mathbf{I} + \beta_2 \mathbf{E} : \mathcal{A} : \mathbf{E}\right] \tag{60}$$

The value $\mathbf{C}\dot{\gamma}$ represents rotary diffusion. Since, rotary diffusion only operates in orientation space, Koch points out that only the components of the tensor tangent to the unit sphere has physical significance.

The first term in eqn. (60) is an isotropic, rotary diffusion that is proportional to the average of the square of the force per unit length of the fibers in the suspension. The second term demonstrates the anisotropic rotary diffusion of the test fiber in the directions parallel to the force per unit length exerted by other fibers, i.e., parallel to the axes of the other fibers. Eqn. (61) writes these two terms separately in indicial notation:

$$\mathsf{C}_{mn}^{\text{isotropic}} = \frac{\beta_1 n L^3}{\dot{\gamma}^2 \ln^2 r_p} \left[\sum_{i,j,k,l=1}^{3} E_{ij} \langle p_j p_i p_k p_l \rangle E_{lk} \right] I_{mn} \tag{61a}$$

$$\mathsf{C}_{mn}^{\text{anisotropic}} = \frac{\beta_2 n L^3}{\dot{\gamma}^2 \ln^2 r_p} \left[\sum_{i,j,k,l=1}^{3} E_{ij} \langle p_m p_n p_i p_j p_k p_l \rangle E_{lk} \right] \tag{61b}$$

where $m = 1 \ldots 3$, $n = 1 \ldots 3$.

Koch determined the constants $\beta_1 = 3.16 \times 10^{-3}$ and $\beta_2 = 1.13 \times 10^{-1}$ by fitting the model to the theory of orientational dispersion in extensional flow (Shaqfeh & Koch [106]) and assessed the accuracy of the approximation with reference to the dispersion in simple shear flow (using the fiber orientation moments from the experiments of Stover et al. [115]). The model is valid for the semidilute regime and Koch mentioned that for $nL^2 d > 3$, the orientational displacement in each interaction is not small and the interactions can not be modeled by the orientation diffusion given in eqn. (60). Phelps & Tucker [92] pointed out that positive eigen-values of Koch's $\mathbf{C}$ tensor should guarantee a physically plausible solution for the orientation distribution function, Ω.

Now unlike Phelps & Tucker's $\mathbf{C}$, which is particularly developed for LFTs, the Koch [65] model for $\mathbf{C}$, eqn. (60), does not pose any such restrictions, and also it is valid in the semidilute regime, where the focus of this research lies. In the literature, either the trend of an anisotropic diffusivity with changes of fiber aspect-ratio and suspension concentration or the behavior of such a diffusivity model, if cast into an

evolution equation, remains largely unexplored. The fiber orientation information predicted with the LBM–EBF simulation can be used to analyze the trend of $\mathbf{C}$, component-by-component, in parameter two space ($c_v \times r_p$), and a solution of the evolution equation with the anisotropic diffusivity model can judge the usefulness of such a model in predicting the fiber orientation moments.

To summarize, the following two different studies are performed next:

I. The LBM–EBF simulation fiber orientation data is used to calculate the Koch model $\mathbf{C}$, eqn. (60). The goal is to measure and analyze the relative magnitudes of the different components of the diffusivity tensor for suspension in steady-state simple shear flow. Suspensions with different concentrations and with different fiber aspect-ratios are simulated with the LBM–EBF method for this reason. The values of $\mathbb{A}$ and $\mathcal{A}$ required to evaluate the Koch model $\mathbf{C}$ are calculated with new fiber configurations in the LBM–EBF computational domain at each timestep. Time averaging of $\mathbf{C}$ is performed assuming ergodicity after the suspension reaches an equilibrium state. These predictions are compared with existing experimental and simulation results, which will be discussed in § 5.5.1.

II. The evolution of fiber configuration in a suspension subjected to an anisotropic rotational diffusion is studied. The second-order evolution equation for $\mathbf{A}$, eqn. (58), with the Koch model, $\mathbf{C}$, is solved for this purpose. Closure approximations are applied to calculate higher order orientation moments in terms of lower order moments (the need for closure approximations are discussed in § 5.4.4). The results are analyzed in § 5.5.2.

After conducting these two studies, a brief discussion of the possible application of the fiber–level LBM–EBF method to directly predict the second order orientation moments is presented.

5.4.4 The closure problem

The weakness of the evolution equation for $\mathbf{A}$ is that some additional information is required to predict flow-induced orientation, since eqn. (53) or eqn. (58) contains a higher order (fourth-order) orientation tensor. The classical solution to this problem is to use a *closure approximation*, a formula that approximates the $(2n+2)^{th}$-order tensor (in this case the 4^{th}-order tensor, which is not known when solving eqn. (53) or eqn. (58)) as a given function of $2n^{th}$-order tensor (in this case 2^{nd}-order tensor). Many closure approximations have been proposed. A good review of their accuracy can be found in the works of Advani & Tucker [2] and Chung & Kwon [29]. The closure approximations used in this work are listed in table 5 in § 5.5.2.

5.5 Results and discussions

5.5.1 Measurement of anisotropic diffusivity with Koch model

The analysis starts with characterizing the variation of the anisotropic diffusivity, $\mathbf{C}$ tensor (Koch model), with change of aspect ratio, r_p, and volume concentration, c_v or non-dimensional volume concentration, nL^3 (for a cylindrical fiber, $nL^3 = \dfrac{4c_v r_p^2}{\pi}$).

Tables 2 – 4 show the variation of $\mathbf{C}$ with increased concentration for fiber aspect-ratios, $r_p = 16$, 32 and 72 respectively. By inspection of the components of $\mathbf{C}$ at a specific concentration and aspect-ratio, it is found that the off-diagonal components are $\mathcal{O}(10^{-3})$ smaller than the largest diagonal component. In the past, Fan et al. [40] attempted to calculate individual components of $\mathbf{C}$ by using their model, eqn. (54), with sample fiber orientation data from their numerical simulations; whereas no experimental report on the components of $\mathbf{C}$ has come to the author's knowledge as yet. Besides, Fan et al. [40] reported the components of $\mathbf{C}$ only for $r_p = 16.9$ and $nL^3 = 30$. In their findings, the components C_{xz} and C_{yz} are small ($\mathcal{O}(10^{-3})$ and $\mathcal{O}(10^{-4})$ respectively) and can be neglected. In general, the LBM–EBF prediction with the Koch model is $\mathcal{O}(10^{-1})$ to $\mathcal{O}(10^{-2})$ smaller than the Fan et al.'s predictions

Table 2: Spatial Anisotropic Diffusivity Tensor $\mathbf{C}$ for $r_p = 16$ at different concentrations with the LBM–EBF simulation using the Koch model at steady simple shear flow ($\mathbf{u} = \dot{\gamma} y \hat{\mathbf{e}}_1$). The Scalar measure of Folgar–Tucker Constant, C_I is extracted from corresponding tensor $\mathbf{C}$ in the table.

nL^3	c_v	$\mathbf{C}$	$\mathsf{C}_I = \frac{1}{3}\mathrm{tr}(\mathbf{C})$
3	0.009204	$\begin{pmatrix} 2.86 \times 10^{-04} & 2.91 \times 10^{-07} & -5.20 \times 10^{-07} \\ \cdot & 7.37 \times 10^{-05} & 1.18 \times 10^{-06} \\ \cdot & \cdot & 1.27 \times 10^{-04} \end{pmatrix}$	1.62×10^{-04}
10	0.030680	$\begin{pmatrix} 1.54 \times 10^{-04} & 7.02 \times 10^{-05} & 8.24 \times 10^{-05} \\ \cdot & 4.90 \times 10^{-04} & 8.55 \times 10^{-05} \\ \cdot & \cdot & 5.98 \times 10^{-04} \end{pmatrix}$	8.77×10^{-04}
20	0.061359	$\begin{pmatrix} 3.49 \times 10^{-03} & 2.35 \times 10^{-04} & 1.87 \times 10^{-04} \\ \cdot & 1.12 \times 10^{-03} & 1.91 \times 10^{-04} \\ \cdot & \cdot & 1.16 \times 10^{-03} \end{pmatrix}$	1.90×10^{-03}

for diagonal components and $\mathcal{O}(10^{-3})$ smaller for non-diagonal components.

The literature offers little data on the diffusivity tensor, $\mathbf{C}$, so it was not possible to compare Koch's $\mathbf{C}$ tensor component-by-component, with theoretical or experimental results other than with Fan et al.'s [40] numerical simulation data. Phan-Thien et al. [89] proposed a way to determine the scalar Folgar–Tucker constant, C_I from the anisotropic diffusivity tensor $\mathbf{C}$, in order to be able to compare with Folgar & Tucker's [43] experimental C_I values. If the three eigenvalues of $\mathbf{C}$ were identical (i.e. isotropic $\mathbf{C}$) then C_I would be equal to its eigenvalues. Otherwise, $\mathbf{C}$ can be reduced into an isotropic tensor with its eigenvalue being equal to the average of the three eigenvalues of $\mathbf{C}$, and the scalar Folgar–Tucker constant C_I can be evaluated as:

$$\mathbf{C} \rightarrow \frac{1}{3}\left(\mathrm{tr}\ \mathbf{C}\right)\mathbf{I} \ \text{ and } \ \mathsf{C}_I = \frac{1}{3}\left(\mathrm{tr}\ \mathbf{C}\right) \tag{62}$$

The last columns of tables 2 – 4 show the scalar Folgar–Tucker constant, C_I, extracted from the Koch model $\mathbf{C}$ with the application of eqn. (62). The C_I values increase monotonically with nL^3 for the same aspect-ratio, r_p; a result which is expected given that higher concentrations lead to an increase in the frequency of fiber–fiber interactions, thus causing greater diffusion of orientation. The trends of

Table 3: Spatial Anisotropic Diffusivity Tensor $\mathbf{C}$ for $r_p = 32$ at different concentrations with the LBM–EBF simulation using the Koch model at steady simple shear flow ($\mathbf{u} = \dot{\gamma} y \hat{\mathbf{e}}_1$).

nL^3	c_v	$\mathbf{C}$	$\mathsf{C}_I = \frac{1}{3}\mathrm{tr}(\mathbf{C})$
5	0.003835	$\begin{pmatrix} 4.78 \times 10^{-04} & 2.04 \times 10^{-05} & -1.14 \times 10^{-05} \\ \cdot & 1.26 \times 10^{-04} & -9.27 \times 10^{-06} \\ \cdot & \cdot & 1.13 \times 10^{-04} \end{pmatrix}$	2.39×10^{-04}
10	0.007670	$\begin{pmatrix} 7.89 \times 10^{-04} & 7.63 \times 10^{-06} & 4.26 \times 10^{-06} \\ \cdot & 2.11 \times 10^{-04} & -6.52 \times 10^{-06} \\ \cdot & \cdot & 1.91 \times 10^{-04} \end{pmatrix}$	3.97×10^{-04}
45	0.034515	$\begin{pmatrix} 3.47 \times 10^{-03} & -1.35 \times 10^{-05} & 8.99 \times 10^{-06} \\ \cdot & 8.73 \times 10^{-04} & -1.09 \times 10^{-05} \\ \cdot & \cdot & 7.66 \times 10^{-04} \end{pmatrix}$	1.70×10^{-03}

Table 4: Spatial Anisotropic Diffusivity Tensor $\mathbf{C}$ for $r_p = 72$ at different concentrations with the LBM–EBF simulation using the Koch model at steady simple shear flow ($\mathbf{u} = \dot{\gamma} y \hat{\mathbf{e}}_1$).

nL^3	c_v	$\mathbf{C}$	$\mathsf{C}_I = \frac{1}{3}\mathrm{tr}(\mathbf{C})$
5	0.000758	$\begin{pmatrix} 1.73 \times 10^{-04} & 5.46 \times 10^{-07} & 3.77 \times 10^{-06} \\ \cdot & 4.56 \times 10^{-05} & -2.74 \times 10^{-06} \\ \cdot & \cdot & 3.35 \times 10^{-05} \end{pmatrix}$	8.42×10^{-05}
10	0.001515	$\begin{pmatrix} 3.45 \times 10^{-04} & -1.23 \times 10^{-06} & 2.15 \times 10^{-06} \\ \cdot & 9.43 \times 10^{-05} & -1.03 \times 10^{-05} \\ \cdot & \cdot & 7.25 \times 10^{-05} \end{pmatrix}$	1.71×10^{-04}
45	0.006818	$\begin{pmatrix} 1.54 \times 10^{-03} & 2.07 \times 10^{-05} & 1.70 \times 10^{-05} \\ \cdot & 3.88 \times 10^{-04} & -9.03 \times 10^{-06} \\ \cdot & \cdot & 2.88 \times 10^{-05} \end{pmatrix}$	7.38×10^{-04}

C_I, increasing with volume fraction for the same fiber aspect-ratio and decreasing with fiber aspect-ratio for the same nL^3, agree with Yamane et al.'s [130] numerical predictions.

Yamane et al. [130] ignored the long range hydrodynamic interactions and applied the lubrication theory to account for contacts between rods by considering the viscous flow in the narrow gap in between. They assumed scalar diffusion and followed Zuzovsky et al.'s [136] method to measure the Folgar–Tucker constant, C_I, by fitting a curve to the damping rate of oscillation of an order parameter $\zeta(t) = \left\langle \frac{p_1^2}{p_1^2 + p_2^2} \right\rangle$. An exponential decay was monitored, and the suspension was regarded to be in steady-state if the oscillation of $\zeta(t)$ damped out apart from some persistent fluctuations. Thus, Yamane et al. [130] found the value of C_I from a transient analysis of the parameter $\zeta(t)$. Yamane et al. [130] explained the trend of C_I, seen in their numerical simulation, by arguing that for a fixed value of nL^3, the collisions among fibers should become less frequent as the diameter decreases and thereby C_I should decrease.

In the LBM–EBF simulation, the number of average contacts per fiber is monitored, and it has been confirmed that the collisions do decrease as the diameter decreases for a fixed nL^3 value in the semidilute regime. However, Yamane et al.'s simulated results for C_I are too low, $\mathcal{O}(10^{-9})$ to $\mathcal{O}(10^{-4})$, compared with Folgar & Tucker's [43] wall bounded shear flow experiments and other simulation results (discussed next). This can be due to the effect of simulating an unbounded shear flow domain or it can be due to the omission of the long range hydrodynamic interactions in their simulations. However, Yamane et al. tried to explain this discrepancy by stating that the Folgar & Tucker [43] experiments were performed in a viscoelastic matrix and experimental values of C_I depended considerably on the method of estimation. The range of simulated value of C_I is about $\mathcal{O}(10^{-5})$ to $\mathcal{O}(10^{-3})$ for the Koch model with LBM–EBF orientation data, and the reliability of this range of C_I in dilute to semidilute regimes is consolidated with the discussion of figure 16 that follows next.

Figure 16 compares the present results of the Folgar–Tucker constant, C_I extracted from the Koch model to the results of the Stover [113] and Stover et al. [115] experiments, the Folgar & Tucker experiments [43] and the numerical results of Phan-Thien et al. [89]. Stover [113] measured the value of C_I for different suspensions by adjusting C_I in the isotropic diffusivity model for Ω (eqns. (51) and (52)) to fit the experimental steady-state ϕ-distributions in simple shear flow. Here, ϕ is the angle between the longitudinal fiber axis and the flow direction. In our co-ordinate system (figure 1) the angle would be $(\pi/2 - \phi)$. They completed the numerical solution of eqn. (51) at steady-state, including the effects of finite aspect-ratio, using the finite difference technique. The best-fit was determined by using the least square technique for the experimental data points and theoretical curve. Their C_I values for $r_p = 31.9$ at several different concentrations $nL^3 = 1$ to 45 are $\mathcal{O}(10^{-4})$ as shown in figure 16. It can be seen that the prediction of C_I ($\mathsf{C}_I = \frac{1}{3}(\text{tr } \mathbf{C})$) with the Koch model is in very good agreement with the experiments of Stover [113] and Stover et al. [115], which demonstrates the accuracy of the fiber orientation data, simulated with LBM–EBF method, and the robustness of the Koch model.

It is evident from figure 16, that the experiments done by Folgar & Tucker [43] yielded overly diffusive values of $\mathsf{C}_I \approx 0.0038$ to 0.0165 for fiber aspect-ratio, $r_p = 16$ in the semidilute regime. They solved the isotropic diffusivity model for Ω (eqns. (51) and (52)) at steady-state in the limit of infinitely thin rods, but they compared their results to the experiments with fibers of finite aspect-ratio (e.g. with $r_p = 16$). It should be noted that, when $nL^3 \to 0$, at a given r_p, the diffusion should be very low due to infrequent fiber interactions, and thus C_I should tend to zero as well. The Stover's [113] experiments confirm this trend, and in this work the Koch model with LBM–EBF data also reproduces this behavior. However, Folgar and Tucker's experimental C_I exceeds 0.003 (a finite amount of diffusion) as nL^3 approaches zero. Folgar & Tucker's use of an infinite aspect-ratio in their calculation of C_I from experimental

data is the reason for this overly diffusive behavior. Phan-Thien et al. [89] reasoned that, by assigning infinite aspect-ratio for a fiber in their model, Folgar & Tucker actually suppressed the flipping motion associated with Jeffery's orbit in simple shear. This effect might emerge through a residual diffusion process with a finite value of C_I. There may be other reasons for this deviation as well. In their experiment, C_I has been obtained for suspensions in a polymeric matrix. In such a matrix, viscoelastic effects can cause significant deviation from Jeffery's orbit. Also, the experiments were conducted with a very low gap to fiber length ratio ($l_2/L = 2.44$) in the Couette device, and the centroids of about 80% of the fibers were within one fiber length from the wall.

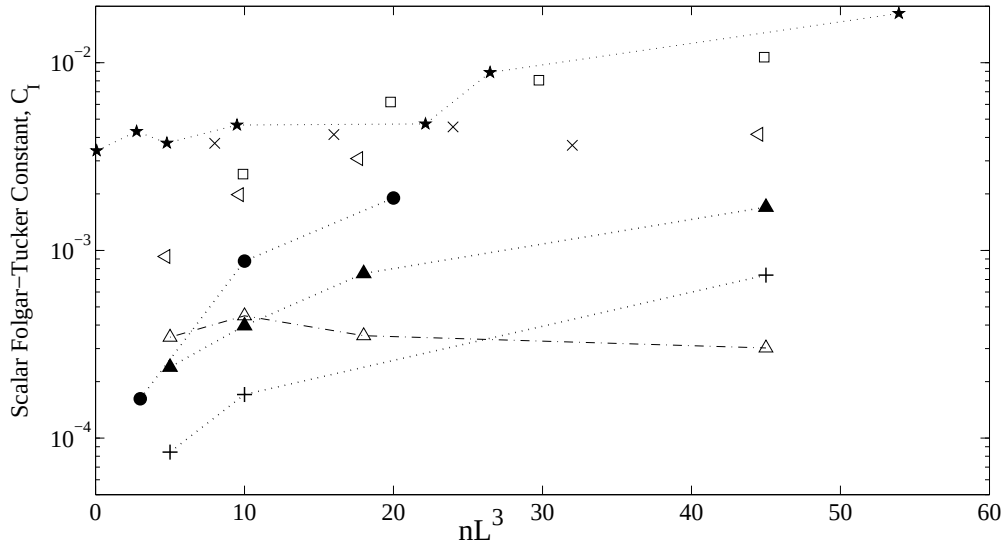

Figure 16: A comparison of the Folgar–Tucker constant, C_I, with the Koch model (using LBM–EBF data) to the experiments and other simulations. *Symbols*: Experiments of Stover [113] and Stover et al. [115]: △ cellulose acetate propionate (CAP) fibers of $r_p = 31.9$ in mixture of glycerine and polyethylene glycol (PEG); Experiment of Folgar & Tucker [43]: ★ nylon fibers of nominal $r_p = 16$ in silicone oil; LBM–EBF simulation: • $r_p = 16$, ▲ $r_p = 32$, + $r_p = 72$ in a Newtonian fluid; Phan-Thien et al. [89] simulation: □ $r_p = 16.9$, ◁ $r_p = 31.9$ in a Newtonian fluid. The dotted lines indicate the trends in data.

Figure 16 also shows the Folgar–Tucker constant, C_I as predicted by the numerical

simulations of Phan-Thien et al. [89]. They determined the six independent components of anisotropic tensor $\mathbf{C}$ by solving eqn. (55) for steady-state shear and extracted a value of C_I in a similar way mentioned before. Phan-Thien et al. did not report the individual components of the tensor $\mathbf{C}$. Their predictions were better in the dilute regime (yielded low diffusion as $nL^3 \to 0$) but exhibited overly diffusive behavior in the semidilute regime. However, their numerical results verified the trend of increases in C_I with increasing nL^3, as observed in Yamane et al.'s [130] simulations and also in the LBM–EBF simulations with the Koch model. Phan-Thien et al. considered both short and long range hydrodynamic interactions but simulated only a small number of fibers (~ 40) in a reference cell. The statistical errors in the numerical simulation of Phan-Thien et al. might be induced by the decision to use a small-sized domain ($0.5 < L/l_2 < 1.0$) to save computational cost, which rules out the possibility of fiber orientation perpendicular to the xy-plane.

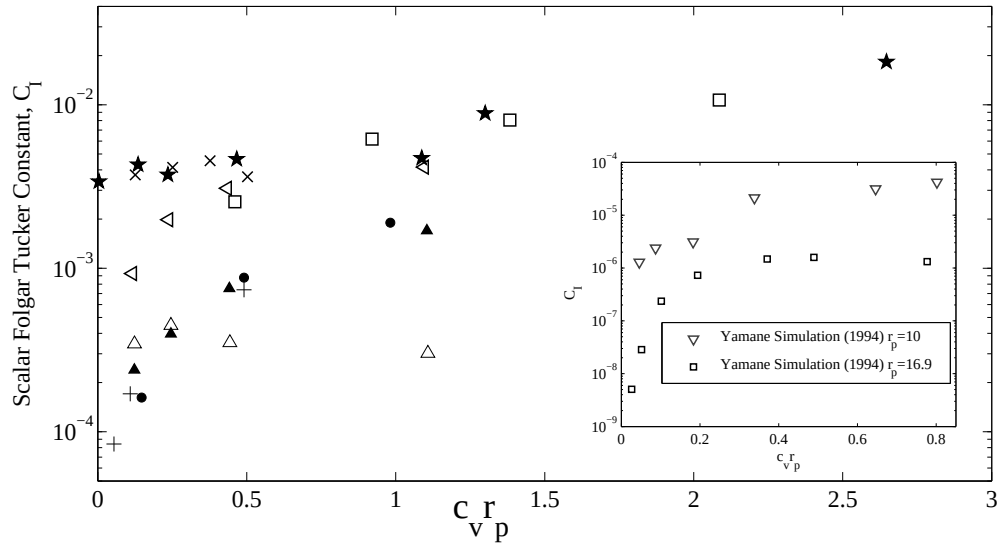

Figure 17: A comparison of the Folgar–Tucker constant, C_I with the Koch model (using LBM–EBF data) to experiments and other simulations. The C_I is plotted against a better measure of concentration $c_v r_p$ in a semidilute regime. *Symbols* are defined in figure 16. The inset shows the simulated C_I values by Yamane et al. [130] which were comparatively low.

In the semidilute to concentrated regimes, a fiber is expected to be found in a

volume dL^2 (*fiber mat*), which leads to $c_v r_p \sim \mathcal{O}(1)$ in this regime. So the simulated C_I should correlate much better with $c_v r_p$ in the semidilute regime than with $nL^3 = c_v r_p^2$, which is the relevant measure in the dilute concentration (in the dilute concentration a fiber is found within volume L^3, and thus $c_v \sim d^2 L/L^3$). Therefore, $c_v r_p$ may be a better measure of concentration in the semidilute regime [89]. Figure 17 and figure 18 (which is essentially a zoomed in portion of figure 17 to focus only on the Koch model with LBM–EBF data in linear scaling) show that when plotted against the parameter $c_v r_p$, the data for C_I at three different aspect-ratios, $r_p = 16,\ 32$ and 72 for the LBM–EBF simulation with the Koch model move together and almost collapse on the same curve. This suggests that an empirical relation for the scalar Folgar–Tucker constant, C_I, can be developed. Phan-Thien [89] proposed an empirical correlation which is of the form:

$$\mathsf{C}_I = M\left[1.0 - \exp\left(-N c_v r_p\right)\right] \tag{63}$$

where the upper bound parameter M can be determined by the value of C_I at $c_v r_p \gg 1$. The parameter N can be determined using a least-square method. However, due to demanding computational cost, it was not possible to conduct a large number of simulations, and thus such an effort to propose a correlation has been set aside for the present study.

5.5.2 Evolution of fiber configuration with anisotropic diffusion

Before predicting the evolution of fibers in the semidilute to concentrated regimes where rotational diffusion is present, it is worthwhile to begin analyzing the evolution of the orientation moment tensor, $\mathbf{A}$ by first showing the solution of the 'standard Folgar–Tucker Model', eqn. (53), for a dilute suspension. In this case, the diffusive contribution, $\dot{\mathbf{A}}^d = 0$ or $\mathsf{C}_I = 0$, but the term $\dot{\mathbf{A}}^J$ (hydrodynamic contribution) exists and gives the orientation kinetics for fibers which are fully non-interacting. Figure 19 demonstrates that for such a suspension, the orientation moments are completely

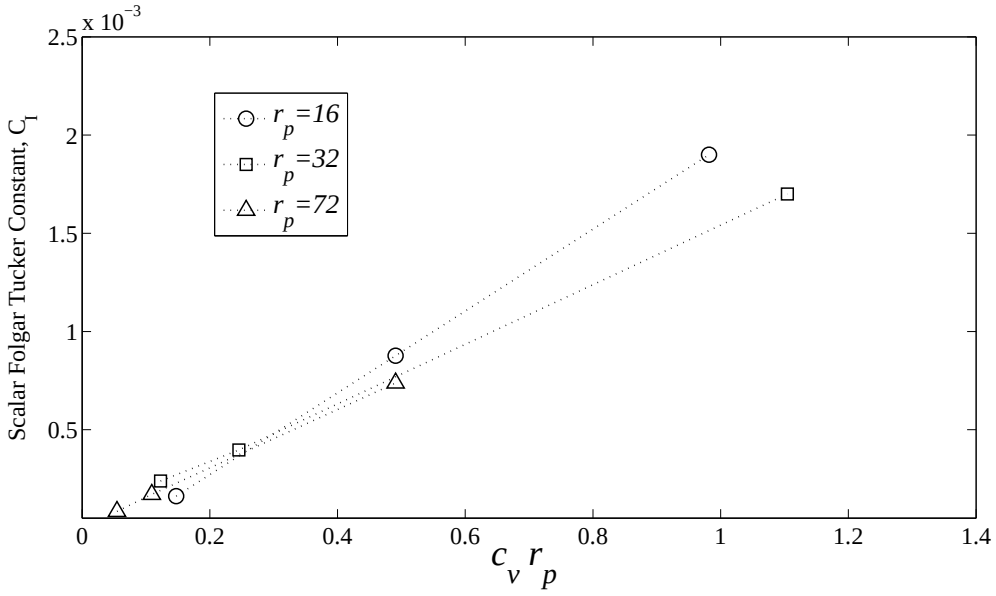

Figure 18: Scalar Folgar–Tucker Constant, C_I with the Koch model (using LBM–EBF data) plotted against a relevant parameter $c_v r_p$ in the semidilute regime.

periodic, since the suspension should theoretically be reversible (i.e. it has a perfect memory).

Now the scalar Folgar–Tucker constant, C_I is usually used in the evolution equation, eqn. (53), for a non-dilute suspension to model an isotropic rotational diffusivity. The performance of this diffusivity has been reported extensively in previous literature [1, 2, 14, 15, 30, 58]. The problem with scalar C_I is that, an increase in C_I (i.e. increased isotropic rotary diffusion) will decrease A_{11}, simultaneously increasing A_{22} and A_{33} and vice-versa. These trends were specially observed when Phelps [91] compared the diagonal A_{ij} experimental values for long fiber thermoplastic composites with the predictions of standard Folgar–Tucker model. It was not possible to match all three diagonal components of A_{ij} with the experimental values simultaneously. So the drawback of using a scalar C_I is its failure to individually tune the A_{11}, A_{22} and A_{33} components [91].

Keeping that in mind, the second-order evolution equation for $\mathbf{A}$ (general 'ARD' model, eqn. (58)) is solved with Koch model $\mathbf{C}$, to quantify the effect of anisotropic

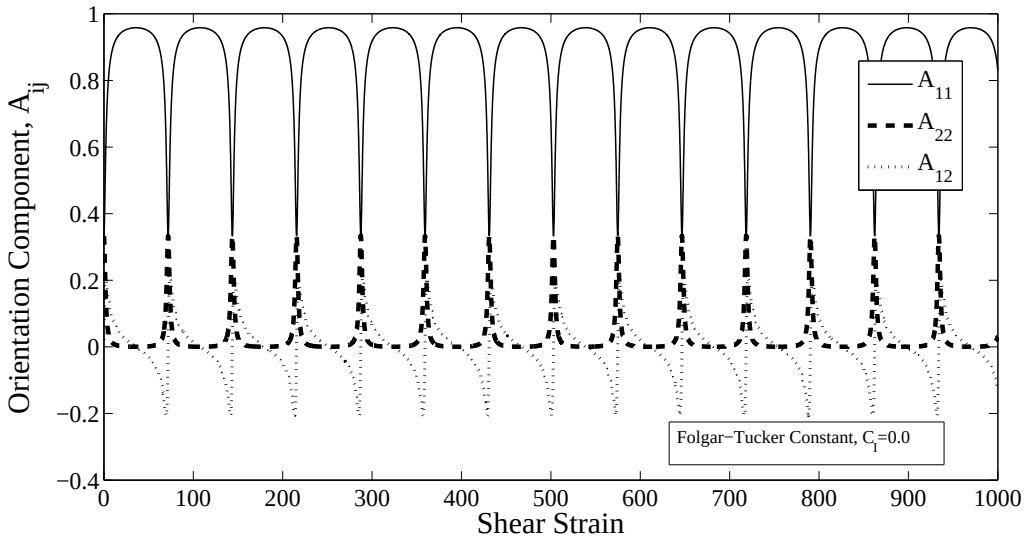

Figure 19: Periodic nature of evolution of second-order orientation moment, **A** when no diffusion is present. (by setting $\mathsf{C}_I = 0$ in eqn. (53)), for a finite aspect-ratio fiber.

Table 5: Abbreviations for closure approximations used in the present study.

Abbreviation	Closure	Orient. Mom.	Reference
NAT	natural	$\mathbb{A}$	[37]
IBF6	invariant-based fitted	$\mathcal{A}$	[58]

diffusion on fiber orientation. The closure approximations from table 5 replace the fourth-order term $\mathbb{A}$ and sixth-order term $\mathcal{A}$. A simple shear flow situation is chosen, because of its importance in many processing flows; e.g. simple shear flow is observed in the 'shell layer' of an injection molding cavity filling process [13, 92]. With reference to a molding cavity, indices 1, 2, 3 would be used here to denote flow direction, x; cavity thickness direction, y; and crossflow direction, z, respectively for the remaining parts of this chapter. The A_{11} component designates flow direction orientation, the out-of-plane orientation is given by A_{22}, and A_{12} represents the tilt of orientation in the 1-2 plane. A_{11} contains most of the qualitative information about the microstructure and is most sensitive to flow, processing and material changes.

For a three dimensional orientation, only five components of **A** are independent

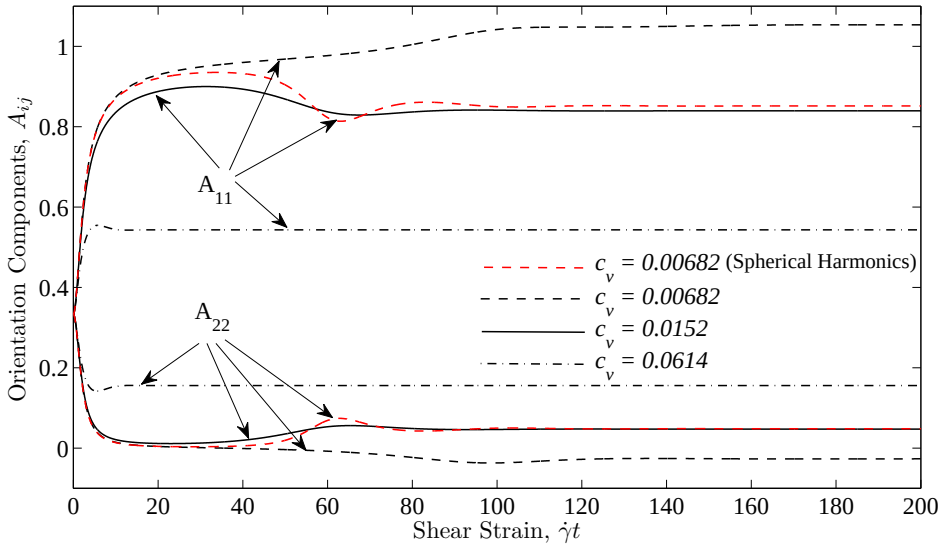

Figure 20: Dynamic solution of eqn. (58) (the general 'ARD' model) with the Koch model for three different concentration cases in simple shear flow. The Spherical Harmonics based expansion method [80] is used for the lowest concentration case to compare with the solution of eqn. (58). A fiber length of $L = 0.688$ mm with an aspect-ratio, $r_p = 72$ is used for all the cases.

in the evolution equation; consequently, only A_{11}, A_{12}, A_{13}, A_{23} and A_{33} are determined with general 'ARD' model, eqn. (58). The other components of the tensor are eliminated using the symmetry ($A_{ij} = A_{ji}$) and normalization condition ($A_{11} + A_{22} + A_{33} = 1$) of the tensor. The resultant five coupled ordinary differential equations are solved with a fourth-order Runge–Kutta algorithm using MATLAB. This solution procedure is implemented through personal communication with Dr. Jay H. Phelps (a former member of Prof. C.L. Tucker's group at UIUC).

Three scenarios are observed by varying the c_v in simple shear flow ($\mathbf{u} = \dot{\gamma} y \hat{\mathbf{e}}_1$, $\dot{\gamma} = 1$). In each case, $L = 0.688$ mm and $r_p = 72$. Figure 20 demonstrates the results with the solution of the general 'ARD' model evolution equation with an anisotropic diffusion (Koch model). For $c_v = 0.0614$, A_{11} and A_{22} equal to approximately 0.55 and 0.165 respectively at steady-state. This result is moderately diffusive, since A_{11} and A_{22} do not evolve significantly from the initial random orientation, $\mathbf{A} = \mathbf{I}/3$.

If c_v is reduced to 0.0152 ($nL^2d = 1.39$), the Koch model gives, $A_{11} = 0.835$ and $A_{22} = 0.04$ at steady-state. When c_v is further reduced to 0.00682 ($nL^2d = 0.625$), A_{11} component rises above unity while the A_{22} component falls below zero, which apprehends non-physical behavior. Phelps [92] pointed out that the $\mathbf{C}$ tensor given by the Koch model should always have positive eigenvalues to guarantee a physically plausible solution for the probability distribution function Ω. Indeed, the eigenvalues for this lowest concentration ($c_v = 0.00682$) case were negative, which explains the non-physical behavior. Using other closures might reduce these errors, although the NAT closure and the IBF6 closure are among the better-behaved closures available in the literature. Phelps & Tucker [92] used the ORE [30] and the IBF6 closures with the Koch model in the general 'ARD' evolution equation for long fiber thermoplastics and found similar non-physical behavior at low c_v.

We present two arguments to support the claim that the non-physical behavior of the Koch model is due to the errors in closure approximations. First, it should be noted that, we calculated the Koch model, $\mathbf{C}$ values with numerical fiber orientation data (tables 2 – 4) and for this particular lowest concentration case, the eigenvalues of $\mathbf{C}$ were found to be positive. As explained before, the 4th order moment, $\mathbb{A}$ and the 6th order moment, $\mathcal{A}$, used in the Koch model are directly calculated with the LBM–EBF simulation data, which do not require the use of any closure approximation. Hence, the positive eigenvalues of $\mathbf{C}$ for the Koch model, obtained by using the LBM–EBF simulation data, give evidence that the non-physical result of the Koch model at a low value of c_v is almost certainly caused by the closure approximations for $\mathbb{A}$ and $\mathcal{A}$ when the model is used in the general 'ARD' evolution equation.

The second more concrete evidence is based on a very recent approach presented by Montgomary-Smith et al. [80] to solve Jeffery's type equation using a Spherical

Harmonic-based expansion technique. This method eliminates the need for orientation tensors and their related closures. The main tools used to compute the coefficients for the spherical-harmonics based expansion are Rodrigue's formula and ladder operators. Montgomery-Smith et al. solved a wide variety of fiber orientation equations that were considered before by Jeffery, Folgar and Tucker, and Koch. Montgomery-Smith et al. showed that the use of the new algorithm retains the accuracy of DFE[2] benchmark simulations for predicting the fiber orientation. Also, it requires only slightly more computational effort than is needed for solving the time evolution of $\mathbf{A}$. The software suite for this method is available publicly through: http://www.math.missouri.edu/∼stephen/software/spherical, and Prof. David Jack of Baylor University, Texas, kindly provided guidelines and feedback to use this software suite.

Figure 20 shows the evolution of A_{11} and A_{22}, as predicted with this spherical harmonic based expansion method (with order 200) for the concerned case of a suspension with $c_v = 0.00682$ and fiber $r_p = 72$. It is seen that at steady-state the moments given by this method are $A_{11} = 0.85171$ and $A_{22} = 0.04821$ respectively; results are clearly physical. The results ensure that the Koch model can be valuable and it can represent the effects of an anisotropic diffusion on the evolution of orientation moments when the model is implemented in a way that avoids any closure approximations.

Now from the viewpoint of a fiber–level numerical simulation such as the LBM–EBF method, the second order orientation moments can be calculated directly by using predicted fiber orientation information. For that purpose, a suspension of simple

[2]Distribution Function Evolution (DFE): Solutions obtained from numerical integration of distribution function $\Omega(\theta, \phi, t)$ (eqn.7 in Cintra & Tucker [30]) using the finite difference code developed by Bay [13]. An isotropic rotary diffusion is used in Bay's method. The results from these DFE calculations provide a benchmark.

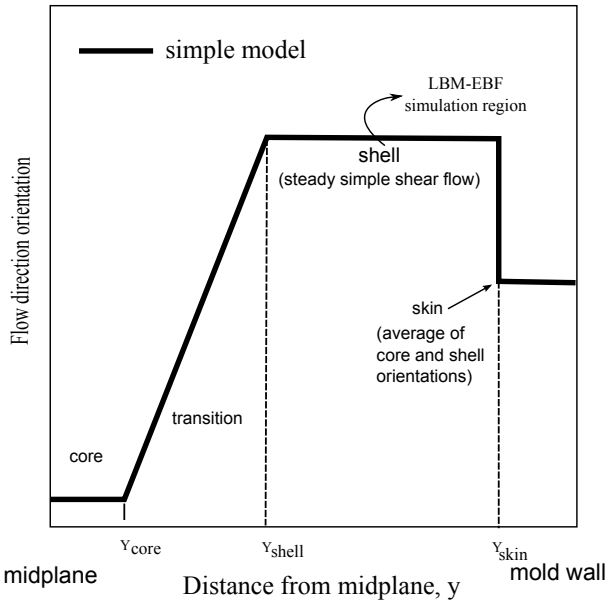

Figure 21: The layers of an injection molded composite. The shell layer orientation is assumed to be the result of steady simple shear.

shear flow is simulated with LBM–EBF simulation, which mimics the shell layer of an injection molding strip. The 'shell layer' usually occupies one quarter to one third of the mold cavity thickness, and the fibers in the shell experience very large shear strains during mold-filling. The fiber orientation in the shell should match the steady-state orientation of fibers in simple shear flow. Figure 21 shows a schematic representation of the A_{11} component observed in different layers of a mold cavity [13].

A comparison can be made between Bay & Tucker's [15] experiment with a SFT material (nylon 6/6 reinforced with 43% glass fibers with average fiber length and diameter of 0.210 mm and 0.011 mm respectively) and LBM–EBF simulation at the same concentration and with same fiber dimensions. Bay & Tucker [15] averaged the steady-state orientation values in simple shear for shell layer and compared the experimental data with: i) standard Folgar–Tucker model predictions (solved eqn. (53) with $\mathsf{C}_I = 0.01$ and hybrid closure), and with ii) DFE calculations (used $\mathsf{C}_I = 0.0003$).

Table 6 shows the A_{11}, A_{22} and A_{12} components obtained by different approaches mentioned above. Bay & Tucker's experimental orientation component A_{11} shows

Table 6: Comparison of LBM–EBF steady-state orientation moments with experimental results of Bay & Tucker [15] and with other predictive methods in simple shear flow ($\mathbf{u} = \dot{\gamma} y \hat{\mathbf{e}}_1$). The volume concentration for the suspension is $c_v = 0.43$. Fiber length, $L = 0.21$ mm and diameter, $d = 0.0105$ mm ($r_p = 20$).

	A_{11}	A_{22}	A_{12}
Bay & Tucker [15] experiment: shell layer in strip	0.895 ± 0.03	0.015 ± 0.01	0.020 ± 0.01
Bay & Tucker [15] prediction with evolution equation: hybrid closure, $\mathsf{C}_I = 0.01$	0.890	0.055	0.151
Bay & Tucker [15] DFE solution:$\mathsf{C}_I = 0.0003$	0.895	0.027	0.021
Spherical Harmonics [80] solution: $\mathsf{C}_I = 0.0003$	0.873	0.0354	0.0167
LBM–EBF: direct numerical prediction	0.959	0.014	0.003

high alignment in the flow direction. The standard Folgar–Tucker model with hybrid closure gave good fit to A_{11}, but greatly overpredicted A_{22} and A_{12}. Bay & Tucker [15] reported that, no value of scalar C_I could fit all the orientation components. The DFE results with $\mathsf{C}_I = 0.0003$ agreed with the experimental results within measurement error. The spherical harmonics based expansion technique with $\mathsf{C}_I = 0.0003$ and order=200 produced a slightly lower value of A_{11} than the experimental A_{11} value, which means fiber alignment is higher in the experiments. The other two components are also comparable with experiments, but not as accurate as of the DFE solution. The corresponding predictions with the LBM–EBF simulation are $A_{11} = 0.959$, $A_{22} = 0.014$ and $A_{12} = 0.003$. So the orientation moments in the flow and in the cavity thickness direction match well with experimental results. But the A_{12} underpredicts the experimental value. This suggests that the C_{12} component of rotary diffusion might be very low in simulation for a concentrated regime. Also the suspension in the simulation is not viscoelastic, which might affect the results.

It should be mentioned that the Koch model is also tested with the Spherical

Harmonics solution (a low order of expansion=30 is used) for the particular suspension system discussed above. The orientation evolution with the Koch model was understandably poor ($A_{11} = 0.5418$, $A_{22} = 0.1573$ and $A_{12} = 0.1021$) in this concentrated regime ($c_v = 0.43$), since the Koch model is developed for use in the semidilute regime only. This limits the use of the Koch model in real fiber-reinforced molding processes, where the suspension is usually highly concentrated. Also, in a highly concentrated regime the orientation evolution would begin from an isotropic state, and the spherical harmonics solution with the Koch model would remain nearly isotropic without any peak being observed in the orientation distribution function. Thus, only a very low order of expansion in the spherical harmonics would lead to a converging solution.

5.6 Summary

In this chapter, the magnitudes and trends of the rotary diffusion (anisotropic in nature) process for a semidilute suspension of rigid rod-like fibers in parameter two space (namely c_v and r_p) are analyzed. The studies are performed in simple shear flows. The diffusion process is represented with a mechanistic model [65], and the model diffusivity is calculated using the LBM–EBF simulation data. An interesting finding from the results is that C_I increases either with decrease of the fiber-aspect ratio (keeping nL^3 constant) or with the increase of volume concentration (keeping r_p constant) in the semidilute regime. The values of C_I, mostly of $\mathcal{O}(10^{-4})$, drawn out from the Koch model match the experimental results of Stover [113] in the semidilute regime. This observation consolidates the fact that the range of C_I ($0.0038 \sim 0.0165$) reported by Folgar & Tucker [43] in the semidilute concentration is overly diffusive, on average two orders of magnitude higher than the values seen in the Stover experiments.

The reason behind this is that Folgar and Tucker assumed infinite aspect-ratio fibers when they fitted the conservation equation for Ω, with adjustable C_I, to their

experimental data, and that assumption triggered the inordinate over diffusion. The overprediction was most prominent when the suspension was infinitely dilute. Also, the very low gap to fiber length ratio in the Couette device, and some other issues with Folgar and Tucker's experimental setup as indicated in § 5.5.1, might have caused some discrepancies between predictions and observations.

Also in this chapter, the difficulties of implementing the Koch model, C, in the evolution equation for $\mathbf{A}$ are pointed out. In particular, it is shown that the model accrues an unphysical solution for the evolution equation at a low concentration. The reason can be attributed to the errors associated with using closure approximations in the Koch model and in the evolution equation. Another concern is that solving the evolution equation with the Koch model is computationally demanding (because of the use of sixth order closure in the model) in comparison to the use of the scalar Folgar–Tucker constant, C_I in the evolution equation. An alternate approach can be the spherical harmonics based method [80].

We showed that the use of fiber–level simulations can also be encouraging to predict fiber orientation moments. The direct prediction of the orientation moments with the LBM–EBF simulation shows viable results to motivate further investigations with this kind of simulations to predict fiber orientation behavior in actual molding processes. In fact, the abilities of emerging fiber–level simulation techniques to account for mechanical contacts (the interaction mechanism that dominates in concentrated regime) and material properties such as fiber flexibility [119, 71, 126, 127] can be useful for simulating fiber orientation in the LFT molding processes. This is because the actual volume fraction, c_v in a typical LFT material far exceeds the "maximum"[3] volume fraction, $c_v^{max} = 5.3(d/L)$, indicating the fibers in the LFT must be bent to some extent [91]. The evolution equation for $\mathbf{A}$ still does not include any parameter

[3]This estimate of c_v^{max} was given by Evans & Gibson [39] for rigid fibers packed in a 3D random state for the SFTs.

to account for fiber flexibility. Thus, a fiber–level simulation method can make an advancement in predicting actual LFT molding process scenarios.

CHAPTER VI

RHEOLOGICAL STUDY OF A SHEARED SEMIDILUTE SUSPENSION

The main objective of this chapter is to understand and interpret the rheological behavior of a semidilute suspension with rigid fibers. The rheological properties of interest for shear-induced migration of the fibers are the relative shear viscosity, μ_{rel} (defined as the ratio of effective shear viscosity, μ_{eff}, and the continuous phase viscosity, μ), the first normal stress difference, N_1, and the second normal stress difference, N_2.

In this research, two approaches are undertaken to calculate these rheological properties from the numerical simulations. One way is based upon the Batchelor's theory. Batchelor [12] theoretically predicted the stress, $\boldsymbol{\sigma}^B$ in dilute and semidilute suspensions of non-Brownian high aspect-ratio fibers with a known orientation distribution as:

$$\boldsymbol{\sigma}^B = \mu_{fiber} \left[\langle \mathbf{pppp} \rangle - \frac{1}{3} \mathbf{I} \langle \mathbf{pp} \rangle \right] : \mathbf{E} \; + \; 2\mu \mathbf{E} \tag{64}$$

where μ is the viscosity of the suspending fluid, and μ_{fiber} is a function of concentration, orientation distribution and fiber geometry. This prediction is valid provided that the fiber interactions are purely hydrodynamic, and there is no fiber–fiber contact. Furthermore, Batchelor [12] found the expression for μ_{fiber} in the dilute limit:

$$\mu_{fiber} = \frac{\pi n L^3 \mu}{6 \ln(2r_p)} \; Q(\epsilon) \tag{65}$$

where $\epsilon = [\ln(2r_p)]^{-1}$, and $Q(\epsilon)$ is the correction factor for finite aspect-ratio fibers. So for particles considered to be infinitely long and thin $Q(\epsilon) = 1$; whereas $\mathcal{O}(\epsilon^2)$ correction is applied for finite-aspect ratio fibers (e.g. finite aspect-ratio circular

cylinder):

$$Q(\epsilon) \approx \frac{1 + 0.64\epsilon}{1 - 1.5\epsilon} \; + \; 1.659\epsilon^2 \tag{66}$$

According to Shaqfeh & Fredrickson [104], eqn. (64) is applicable in the semidilute regime as well, for slender particles, with:

$$\mu_{fiber} = \frac{\pi n L^3 \mu}{3\left(A - \ln c_v + \ln\left(-\ln c_v\right)\right)} \tag{67}$$

where A is a function of the orientation distribution. When all fibers are aligned in a common direction, then, $A = 0.16$, whereas $A = -0.66$ for an isotropic orientation distribution. Since no $\mathcal{O}(\epsilon)$ or $\mathcal{O}(\epsilon^2)$ correction was developed for eqn. (67), Stover et al. [115] heuristically assumed that the correction factor $Q(\epsilon)$ from eqn. (66) for the dilute case could also be applied in eqn. (67). This assumption notably improved the agreement between their experimental observations and the theoretical predictions of the relative viscosity. This concept was also successfully employed by Mewis & Metzner [79] for the measurement of elongational viscosity.

When boundary effects are negligible, a relative viscosity, μ_{rel} can be defined along with normal stress differences. The relative viscosity of the dilute or the semidilute regime is expected to be the result of a purely hydrodynamic stress and can be seen from eqn. (64) to be a function of the $\langle p_1^2 p_2^2 \rangle$ component of the quadrad $\langle \mathbf{pppp} \rangle$, where the subscripts 1 and 2 refer to the flow and gradient directions, respectively. Hence, the relative viscosity μ_{rel}, the first normal stress difference N_1, and the second normal stress difference N_2 can be identified in eqn. (64) to be:

$$\mu_{rel}^B = 1 + \frac{\mu_{fiber}}{\mu} \left\langle p_1^2 p_2^2 \right\rangle \tag{68a}$$

$$N_1^B = \mu_{fiber} \dot{\gamma} \left(\left\langle p_1^3 p_2 \right\rangle - \left\langle p_1 p_2^3 \right\rangle \right) \tag{68b}$$

$$N_2^B = \mu_{fiber} \dot{\gamma} \left(\left\langle p_1 p_2^3 \right\rangle - \left\langle p_1 p_2 p_3^2 \right\rangle \right) \tag{68c}$$

Equations (68a) – (68c) can be used to compute the rheological properties from the suspension state obtained from the simulations, as it is possible to calculate the

required moments by averaging over all fibers. The superscript 'B' in equations (68a) – (68c) is used to refer to rheological properties calculated with Batchelor's theory, the validity and accuracy of which depend on the theoretical framework based on eqn. (64).

In this research, the first way adopted to calculate the rheological properties is based on Batchelor's theory as expressed in equations (68a) – (68c). These measurements are valid under the conditions that fibers are moving freely without any mechanical contacts. Batchelor's theory is used for this calculation because it clearly shows the relation between the fiber orientation distribution and the rheological properties of a suspension. This feature is very important in finding the physical explanations for rheological properties which are computed in a direct way with simulation.

The rheological properties are obtained directly by computing the averaged stress tensor in a cubic box-shaped subdomain. If $E_{xy} = \dot{\gamma}/2$ is the shear strain component of the strain-rate tensor, $\mathbf{E}$, and σ_{xy} is the shear stress component of the stress tensor, $\boldsymbol{\sigma}$, then the rheological properties are given by:

$$\mu_{rel}^{*} \equiv \frac{\mu_{eff}}{\mu} = \frac{\sigma_{xy}}{2\mu E_{xy}} \tag{69a}$$

$$N_1^{*} \equiv \sigma_{xx} - \sigma_{yy} \tag{69b}$$

$$N_2^{*} \equiv \sigma_{yy} - \sigma_{zz} \tag{69c}$$

Here, the superscript '$*$' is used to denote properties calculated directly using the averaged stress tensor in a subdomain.

Eqn. (69a) is used to calculate the relative viscosity, μ_{rel}^{*}, of the suspension. The LBM–EBF solution provides a full dynamic state description regarding the flow in the medium, and fiber–fluid as well as fiber–fiber interaction forces. This allows for the direct computation of relative viscosity, μ_{rel}^{*}, which includes the effect of mechanical contacts. A comparison of this direct measurement of μ_{rel}^{*} with the measurement of μ_{rel}^{B} can quantify the possible effect of mechanical contacts in the semidilute regime.

The results are also compared with experimental measurements.

6.1 Study of steady-state relative shear viscosity

A review of literature (Nawab & Mason [82]; Blakeney [18]; Bibbo [17]; Stover et al. [115], Petrich et al. [88]; Sepehr et al. [102]; Thomasset et al. [120]; Lindström & Uesaka [71], [72]; Keshtkar et al. [61]) on fiber suspension confirms that adding fibers either to a Newtonian or a non-Newtonian fluid will increase both the shear viscosity and the first normal stress difference of the suspension.

In this research, with LBM–EBF fiber orientation information, the steady-state relative viscosity, μ_{rel}^{B}, has been measured with eqn. (68a). The μ_{fiber} is calculated with Shaqfeh and Fredrickson's proposed model, eqn. (67), in the semidilute regime with a multiplication to the correction factor $Q(\epsilon)$. In choosing $Q(\epsilon)$ for the semidilute regime, eqn. (66) is used, since the same heuristic assumption made by Stover et al. [115] is also followed here. In eqn. (67), $A = 0.16$ (corresponding to the fibers being aligned in a common direction) is chosen; in shear flow, fibers will spend most of the time aligned with the xz-plane, so the distribution will be more aligned in nature than to follow an isotropic state.

The parameter sets used in the simulations, and for the experimental investigations of Blakeney [18], Bibbo [17], Petrich et al. [88] and Stover et al. [115] are compiled in table 7. Bibbo [17] has measured the relative viscosity of fibrous suspensions, using a torsion cup, which is a parallel-plate rheometer with a wall attached to the outer edge of the lower plate, to hold the suspension in place. Blakeney [18] used a concentric cylinder viscometer to measure the relative viscosity of suspensions of straight, rigid nylon fibers. For rheological measurements, Petrich et al. [88] employed both concentric cylinders and parallel plate geometries. Since, the parallel plate rheometer was smaller, and curvature was more pronounced, the streamline curvature caused reduction in effective aspect-ratio, r_e, of the fibers in the rheometer, which

Table 7: Parameter sets used in the viscosity measurement experiments of Blakeney [18], Bibbo [17], Stover et al. [115] and Petrich et al. [88] for straight fibers. The parameters used in the LBM–EBF computer simulations are also included. The l_2 parameter refers to the gap height in the viscometers, and in case of the numerical simulation it refers to the height of the computational domain in the gradient direction. The symbol for each set of parameters is used in figure 23 for plotting the results.

	L (mm)	d (μm)	r_p (-)	$\dot{\gamma}$ (s^{-1})	μ (Pa.s)	l_2 (mm)	Symbol
Blakeney	0.324	16.9	19.2	< 0.4	10.23	22.75	◊
	0.875	43.1	20.3	< 0.4	10.23	22.75	×
Bibbo	2.0	120	17	$1 - 100$	13	> 3.0	○
	4.0	120	33	$1 - 100$	13	> 3.0	□
	6.0	120	51	$1 - 100$	13	> 9.0	▽
Stover et al.	1.61	95	16.9	$0.319 - 0.471$	1	17.5	+
	2.68	84	31.9	$0.447 - 0.472$	1	17.5	★
Petrich et al.	0.65	13	50	0.5	27.5	8.0/2.0	△
	0.55	11	50	0.5	27.5	8.0/2.0	△
LBM–EBF	1.52	95	16	$10 - 80$	1	$7.6 - 16.4$	●
	2.69	84	32	80	1	> 13.4	■
	6.0	115.4	52	80	13	24	▼

induced extra fiber-flipping. So in general, the relative viscosity measurements were slightly higher in the parallel plate geometry in Petrich et al.'s experiments. However, the results were typically comparable to within experimental error. Stover et al. [115] used a Couette device with an outer rotating cylinder (see figure 5 in § 4.1) for the experiments, and measured the fiber orientation using image analysis techniques. They did not directly measure the relative shear viscosity; rather they calculated the relative shear viscosity, μ_{rel}^B using Batchelor's theory.

Notably in table 7, the LBM–EBF simulations used higher shear rates than the shear rate used in the physical experiments of Blakeney [18], Petrich et al. [88] or Stover et al. [115]. This improved the numerical efficiency by decreasing the computational cost; but even with this reasonably high shear rate, the particle Reynolds numbers are restricted to the Stokes flow regime. This implies that the viscosity is

shear independent; within this regime drag forces are proportional to velocity, and consequently, the shear stresses of the suspension are proportional to the shear rate. In a shear rate dependent suspension of fibers, the viscosity decreases with increasing shear rate, until a plateau is reached [17, 46]. Bibbo's experiments were conducted at a shear rate rendering an asymptotic high shear viscosity. Therefore, the LBM–EBF simulation results can reasonably be assumed to represent this asymptotic high shear viscosity.

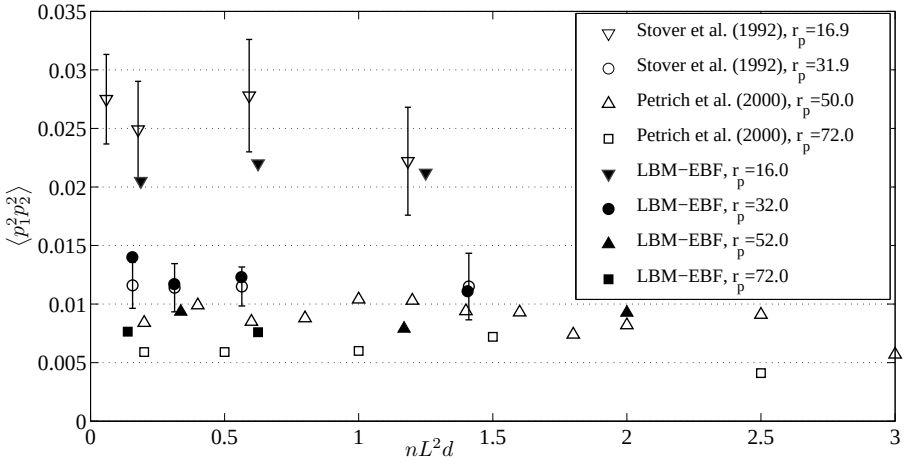

Figure 22: Values of $\langle p_1^2 p_2^2 \rangle$ as a function of nL^2d from experiments and LBM–EBF simulation. Stover et al.'s [115] data are within 80% and Petrich et al.'s [88] data are within the 90% confidence interval, respectively.

Before studying the results of suspension viscosity calculated with Batchelor's theory, it is important to study the moments of the orientation distribution $\langle p_1^2 p_2^2 \rangle$ which is used in Batchelor's theory to predict μ_{rel}^B with eqn. (68a). Figure 22 compares this moment among the experiments and the LBM–EBF simulations. Stover et al. [115] measured $\langle p_1^2 p_2^2 \rangle$ for $r_p = 31.9$ and 16.9 respectively and found that it was independent of fiber concentration throughout the semidilute regime for both the aspect-ratios. For $r_p = 16.9$ the semidilute plateau for $\langle p_1^2 p_2^2 \rangle$ was at about 0.025 and for $r_p = 31.9$ there was another semidilute plateau with all the values of $\langle p_1^2 p_2^2 \rangle$ being within 1% of 0.0115. Petrich et al.'s [88] experimental $\langle p_1^2 p_2^2 \rangle$ for aspect-ratios

Table 8: Comparison of $\langle p_1^2 p_2^2 \rangle$ between the LBM–EBF simulation and Koch's [65] correlation

r_p (-)	nL^3 (-)	LBM–EBF $\langle p_1^2 p_2^2 \rangle$	Koch's Correlation $\langle p_1^2 p_2^2 \rangle = 0.371/r_p$
16.0	3	0.0205	0.0232
	10	0.0223	
	20	0.0212	
32.0	5	0.0140	0.0116
	10	0.0117	
	18	0.0123	
	45	0.0111	
52.0	17.5	0.0094	0.00713
	60.8	0.0079	
	104	0.0093	

50 and 72 also did not show any clear trend as a function of concentration. For their experiment, the error bars overlapped with the majority of the data points, since the 90% confidence interval for their measured data was approximately ±10% of the value. Koch [65] fitted Rahnama et al.'s [97] expression for the orientation distribution to Stover et al.'s experimental data. The correlation thus resulting from Koch's calculations shows that $\langle p_1^2 p_2^2 \rangle = 0.371/r_p$. Experimental values of $\langle p_1^2 p_2^2 \rangle$ from Stover et al. (with $r_p = 16.9$), and Petrich et al. (with $r_p = 50$ and 72), slightly overpredict Koch's correlation for fibers with the same aspect-ratios. Table 8 presents the moment $\langle p_1^2 p_2^2 \rangle$ extracted from the fiber orientation data of the LBM–EBF simulations along with corresponding Koch's correlation predictions for different concentrations and aspect-ratio fibers. Now, the data from table 8 can be compared with the experimental results plotted in figure 22. For $r_p = 16$, the $\langle p_1^2 p_2^2 \rangle$ with LBM–EBF underpredicts Stover et al.'s experimental results (the experiments were performed with a slightly different aspect ratio, $r_p = 16.9$) but is in good agreement with Koch's correlation. The simulated values of $\langle p_1^2 p_2^2 \rangle$ match with the experiments very well for aspect-ratios, 32 and 52, respectively; but the simulated results for $r_p = 52$ slightly overpredict the

Koch's correlation; whereas the results for $r_p = 32$ are in very good agreement with Koch's correlation. Overall it can be said that the LBM–EBF simulation verified the experimental and the empirical observations that the $\langle p_1^2 p_2^2 \rangle$ values are not dependent on the change of concentrations.

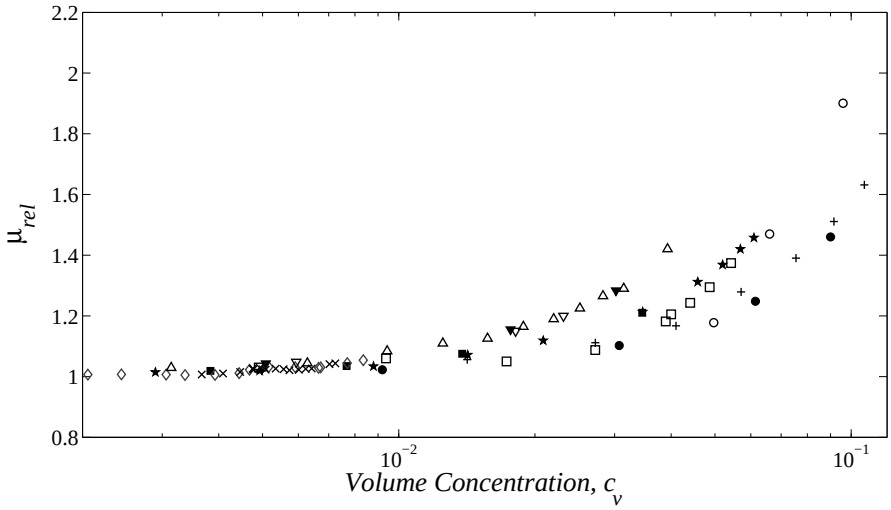

Figure 23: The relative viscosity, μ_{rel}, as a function of the volume concentration, c_v. Blakeney [18], Bibbo [17], Stover et al. [115] and Petrich et al. [88] used experimental viscometers to measure the viscosity of a suspension. Stover et al. [115] used experimental fiber orientation data to calculate the relative viscosity using Batchelor's [12] theory with the application of the semidilute limit correction for finite aspect-ratio fibers. The LBM–EBF simulation also used the same method to calculate the relative viscosity from simulated fiber orientation data. The symbols used in the figure are listed with corresponding parameter sets in table 7.

Now in figure 23, the experimental relative shear viscosity, μ_{rel} is compared to μ_{rel}^B calculated with LBM–EBF simulation data. Measures of μ_{rel}^B which were reported by Stover et al. (calculated using their fiber orientation experimental data) are also included in figure 23. The relative shear viscosity, μ_{rel}^B with the LBM–EBF simulation and with the experiments of Stover et al. compare reasonably well with Bibbo's [17] experimental, μ_{rel}, underpredicting Bibbo's data for low aspect-ratio fibers ($r_p = 16$ or 16.9), and slightly overpredicting the results which use higher aspect-ratio ($r_p = 32$

or 31.9) fibers. With a further increased aspect-ratio of $r_p = 52$, the μ_{rel}^B with LBM–EBF simulation data almost overlaps with experimental μ_{rel}, measured by Bibbo [17] and Petrich et al. [88] (for aspect-ratios $r_p = 51$ and 50, respectively). One of the reasons for higher aspect-ratio fibers to better reproduce experimental relative shear viscosity is because an aligned fiber orientation state is assumed in determining the model for μ_{fiber} given by Shaqfeh & Fredrickson [104]. Since in the semidilute regime, on average, only $\mathcal{O}(1/r_p)$ fibers flip at any given time, the higher aspect-ratio fibers are in a greater aligned state than lower aspect-ratio fibers in a suspension. So the assumption of aligned state is more suitable in eqn. (67) for higher aspect-ratio fibers; whereas assuming an aligned state predicted lower values of μ_{fiber} in eqn. (67) for r_p 16 or 16.9 and yielded smaller values of μ_{rel}^B when compared to the experimental μ_{rel}. However, the isotropic assumption of fiber orientation state ($A = -0.66$ in eqn. (67)) would lead to slightly higher viscosity, but still would be less than experimental measurements. The possibility of transmission of stress in the semidilute suspension due to actual mechanical contacts (a non-hydrodynamic effect which the Batchelor's theory with Shaqfeh & Fredrickson's model for μ_{fiber} in the semidilute regime does not consider) can be the reason for underprediction of suspension viscosity in the semidilute regime.

Figure 24 plots steady-state specific viscosity $\mu_{sp} \equiv \mu_{rel} - 1$ as a function of c_v to investigate the effect of fiber–fiber mechanical contact on suspension shear viscosity in comparison to the shear viscosity of the suspension where fiber–fiber hydrodynamic interactions are present alone. The simulated fiber orientation data from the LBM–EBF, and the experimental fiber orientation data from Stover et al. are used to produce μ_{sp}^B for both approaches. Bibbo's direct experimentally measured, μ_{sp}, is plotted as well in figure 24. Now in order to include any possible mechanical contact effect, the μ_{rel}^* is calculated from the averaged stress tensor in a computational subdomain in the LBM–EBF simulation, for $r_p = 16$. The $\mu_{sp}^* = \mu_{rel}^* - 1$ is extracted and

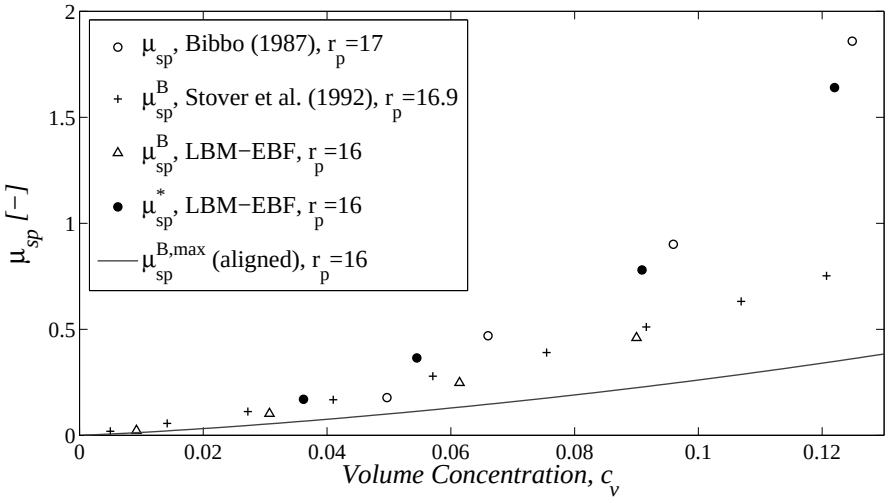

Figure 24: Specific Viscosity, μ_{sp} as a function of volume concentration, c_v. The solid line represents the theoretical upper limit of μ_{sp} for a suspension – with fibers of $r_p = 16$, all fibers are in the flow-gradient plane, the ϕ-distribution is given by Jeffery's prediction, and the viscosity is calculated with an aligned version of Batchelor's theory.

plotted in figure 24. It is seen that, for $c_v \geq 0.055$ (for a cylindrical fiber with $r_p = 16$, $c_v = 0.055$ corresponds to $nL^3 = 17.93$) the μ_{sp}^B values underpredict Bibbo's experimental μ_{sp}. It is first necessary to investigate whether an approximate upper limit $\mu_{sp}^{B,max}$ for hydrodynamic interactions can match Bibbo's experiments. In numerical [71, 100] and experimental [115, 88] studies, it was observed that the ϕ-distribution differs very slightly from ϕ-distribution given by Jeffery's solution, eqn. (41). Hence, it is possible to calculate an approximate upper limit $\mu_{sp}^{B,max}$ for the specific viscosity by considering a suspension with all the fibers in the xy-plane, the ϕ-distribution to be given by Jeffery's solution, and by using the Batchelor's theory to calculate the viscosity. This upper limit is shown with a solid line in figure 24. Even this estimate of hydrodynamic upper limit of $\mu_{sp}^{B,max}$ underpredicts Bibbo's experiments, and the deviation from the experiment increases with increasing concentration. The μ_{sp}^B with the present LBM–EBF simulation, and with Stover et al.'s experiments, fall very close to $\mu_{sp}^{B,max}$ in the dilute regime, but unexpectedly fall above the maximum

specific viscosity, $\mu_{sp}^{B,max}$, in the semidilute to concentrated regimes. It might seem surprising that these values are higher than the maximum limit predicted by Batchelor's theory. The reason behind this is that the moment $\langle p_1^2 p_2^2 \rangle$ calculated with the LBM–EBF simulations or with the experiments of Stover et al. implicitly includes some of the effects of non-hydrodynamic interactions present in the suspension, and this causes the predictions to be higher than the maximum limit drawn by hydrodynamic interactions alone; but to remind again, the predictions still remain lower than the Bibbo's μ_{sp}. Finally, a comparison of μ_{sp}^{*} with Bibbo's μ_{sp} reveals that the μ_{sp}^{*} is excellent in reproducing the trend in experimental specific viscosity quantitatively. The μ_{sp}^{*} falls close to the results with Batchelor's theory in the dilute regime, as mechanical contacts are rare therein. With increased concentration, it deviates from the results of Batchelor's theory, showing evidence of extra stress transmission due to non-hydrodynamic mechanical contacts, which enhances suspension viscosity. So a conclusion can be drawn that mechanical interactions have a noticeable effect on the viscosity of the semidilute suspension. Also, it can be suggested that an additional correction factor for mechanical contacts needs to be developed to use with Batchelor's theory, for theoretical prediction of suspension viscosity in semidilute to semiconcentrated fiber suspension flow.

6.2 First normal stress difference in dilute to semidilute fiber suspensions

According to Batchelor's theory [12], the moment of the orientation distribution, $(\langle p_1^3 p_2 \rangle - \langle p_1 p_2^3 \rangle)$, that governs the normal stress difference is zero for a structure corresponding to fibers following Jeffery's orbits, because it is an odd function of p_2. It has been argued that this moment must also be zero for purely hydrodynamically interacting fibers [88]. However, throughout the semidilute regime, slight asymmetries in ϕ-distributions (asymmetry about the flow-vorticity plane) have been observed in experiments [115, 88], and in numerical simulations [117, 71]; these asymmetries could

result in small or non-zero first normal stress difference, N_1. Non-zero positive values of N_1 have frequently been reported for fiber suspensions [135].

In a steady-state dilute suspension of rigid axisymmetric particles, where shear flow dominates small but non-negligible Brownian disorientations, Hinch & Leal [52] stated that the normal stress differences are of $\mathcal{O}\left(D^r\right)$, where $D^r << 1$. They mention that at steady-state, the normal stresses are $\mathcal{O}\left(D^r r_p^3\right)$ smaller than the steady-state shear stress. Hinch & Leal's [53] calculations for ellipsoids give the second normal stress difference, N_2, less than one-tenth of the magnitude of the first normal stress difference, N_1. It is a common belief that the N_2 is much less than the N_1 (on the order of 10%), and can be neglected [88, 102].

Since fibers undergoing hydrodynamic and coulombic solid-body interactions in suspensions are expected to yield orientation moments independent of the shear rates, the normal stress in such systems is directly proportional to the shear rate, $\dot{\gamma}$; this is unlikely in a polymer solution, where $N_1 \propto \dot{\gamma}^2$. Batchelor's theory shows this proportionality in eqns. (69b)–(69c). Based on Ericksen's continuum model [38], Carter [24] and Carter & Goddard [25] also predicted a linear dependence of the normal stresses on shear rate. For non-dilute suspensions with large aspect-ratio fibers, Carter [24] derived an expression for first normal stress difference:

$$\frac{N_1}{\mu\dot{\gamma}} \propto \frac{c_v r_p^2}{\ln\left(2r_p\right) - 1.8} \left\langle \sin(2\phi) \right\rangle \tag{70}$$

Carter assumed that $\langle \sin(2\phi) \rangle$ scales with r_p in the same way as $\langle \sin(2\phi) \rangle \propto \sqrt{1/r_p}$. On the basis of Jeffery's maximum energy dissipation [59], and assuming collision between the fibers to be the major cause for non-zero normal stresses in steady shear flow, the N_1 can be written as:

$$\frac{N_1}{\mu\dot{\gamma}} = K \frac{c_v r_p^{3/2}}{\ln\left(2r_p\right) - 1.8} \tag{71}$$

where 'K' is a constant, and must be determined experimentally.

Carter [24] and Carter & Goddard [25] experimentally measured the nonzero first normal stress difference for suspensions of E-glass fibers (r_p=57, 114 and 228) in a Newtonian polybutene oil. Kitano & Kataoka [63], with a cone and plate rheometer, observed that the first normal stress difference of suspensions of vinylon fibers (r_p=45.3, 112.5 and 120.1) in silicone oil increased with suspension concentration and fiber aspect-ratio. Petrich et al. [88] used the parallel plate attachment on the rheometer to investigate normal stresses with either glass or carbon fibers ($r_p = 50$) in PB fluid (mixture of two viscous polybutenes and a high index plasticizer). Table 9 lists the experimental and simulation parameter sets used for measuring first normal stress difference.

Table 9: Parameter sets used in the first normal stress difference measurements of Carter [24], Petrich et al. [88], Kitano & Kataoka [63] for straight rigid fibers and the parameters used in the LBM–EBF simulations. The experiments of Petrich et al. and the LBM–EBF simulation use the same set of parameters as for viscosity measurement (table 7). Those parameters are included here again for completeness.

	L (mm)	d (μm)	r_p (-)	$\dot{\gamma}$ (s^{-1})	μ (Pa.s)	l_2 (mm)
Carter	0.2	3.5	57	~ 100	18.6	< 1.0
Petrich et al.	0.65	13	50	0.5	27.5	8.0/2.0
	0.55	11	50	0.5	27.5	8.0/2.0
Kitano & Kataoka	1.22	26.8	45.3	$0.007 - 12$	100	0.175
LBM–EBF	6.0	115.4	52	80	13	24

Several researchers have tested Carter's model, eqn (71), on their normal stress measurements (Carter [24]; Kitano & Kataoka [63]; Goto et al. [46]; Zirnsak [135]; Petrich et al. [88]; Sepehr et al. [102]; Keshtkar et al. [61]). These experimental data fell within a band, for which constant K ranged from 0.035 to 0.32, but no discernible relation between K and variables such as fiber volume fraction and aspect-ratio could be determined. However, by analyzing data from different researchers, Zirnsak et al. [135] showed that in the semidilute regime for high aspect-ratio stiff fibers, the

constant K falls into a narrower band of 0.035 to 0.16. The other data, which lie scattered above this band are for flexible fibers with very high aspect-ratio.

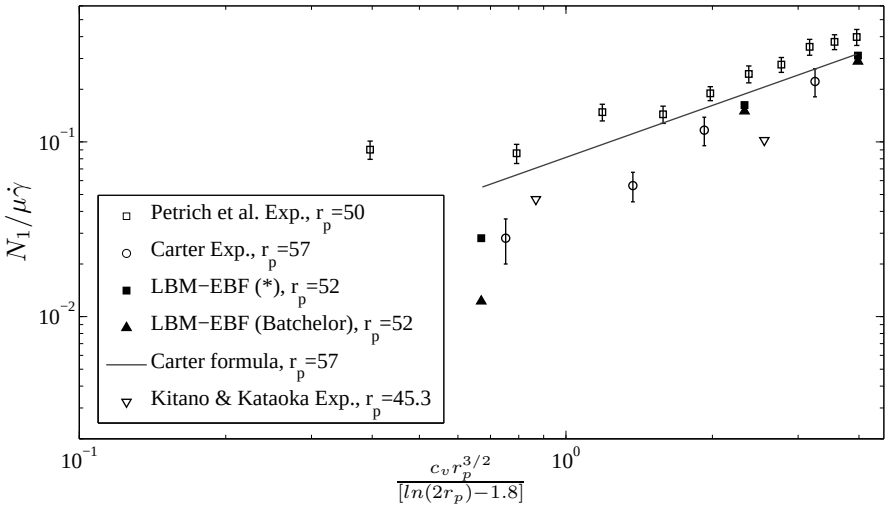

Figure 25: The steady-state first normal stress difference, N_1, scaled with $\mu\dot{\gamma}$ is plotted as a function of volume concentration, c_v and fiber aspect-ratio, r_p. Petrich et al.'s measurements are within the 90% confidence interval. In the relation suggested by Carter [24], eqn. (71), the expressions on the axes should be proportional. The slope of the solid line indicates proportionality.

Figure 25 compares the directly computed (eqn. (69b)) first normal stress difference, N_1 with the LBM–EBF simulation (distinguished with '$*$') to the prediction of N_1 with Batchelor's theory (eqn. (68b)) as calculated with moments from the LBM–EBF simulation data for aspect-ratio $r_p = 52$. Figure 25 also plots results from experiments listed in table 9. The N_1 measured with the Batchelor's theory underpredicts Petrich et al.'s experimental N_1 slightly, whereas the directly calculated N_1 with eqn. (69b) accounts for the mechanical contacts and matches better with experiments. In figure 25, the N_1 values are normalized with $\mu\dot{\gamma}$ and plotted against the parameter $[c_v r_p^{3/2}/(\ln(2r_p) - 1.8)]$ to test the applicability of Carter's formula (eqn (71)). A solid line is drawn following Carter's formula, with slope $K = 0.08$ for guidance. This same slope was also chosen by Petrich et al. to fit their data with $r_p = 50$, since Carter's results for $r_p = 57$ agreed with that slope. The results indicate

that the Carter's formula fails in the semidilute regime, but as volume concentration increases – it becomes more accurate, so that the experimental and simulated first normal stress differences fall onto the same curve, whose slope is close to K (≈ 0.08). Cater did not include the dependency of $\langle \sin 2\phi \rangle$ on volume concentration in eqn. (70). Lindström & Uesaka [71], with their numerical simulation presented evidence that the term $\langle \sin 2\phi \rangle$ is proportional to fiber number density, n, and thereby proportional to c_v in dilute to semidilute regimes and approximately constant in the concentrated regime. Hence, in concentrated regime, Carter's formula, eqn. (71), is more reliable and accurate, since the $\langle \sin 2\phi \rangle$ factor is assumed to be constant in the formula. The existence of the first normal stress difference provides additional evidence of mechanical contacts among fibers in the suspension. Analogous to the observations for the relative shear viscosity, the increase in normal stress above that predicted by the hydrodynamic Batchelor's theory is indicative of transmission of stress via mechanical contacts.

It should be noted that the steady-state second normal stress difference, N_2, is also calculated in the LBM–EBF simulations. But it is found that N_2 is small in relation to the numerical noise; the ratio of steady-state $|N_2|$ to the root-mean-square of $N_2(t)$ was less than 0.6 in all instances. Therefore, no reliable results for N_2 can be reported.

With the fiber–level LBM–EBF simulation, the investigations are performed in the parameter two-space ($r_p \times nL^3$) and the effect of inter-fiber friction on rheological properties is not considered. Recently, Lindström & Uesaka [72] included the effect of inter-fiber friction in their numerical simulation for non-Brownian rigid fibers and reported its effect (by changing friction coefficient, η_{fric}) on the normal stress differences. They observed that the steady-state N_1 increases with the increase in η_{fric} for a specific aspect-ratio fiber while keeping the concentration of the suspension constant. Lindström & Uesaka further investigated the dependence of N_1 on η_{fric} empirically by

assuming tentatively a function $\mathsf{g}(\eta_{\text{fric}}, nL^3, r_p)$ to model the effect of friction. They found that g is approximately a linear function of the cross term $nL^2 d\eta_{\text{fric}}$ in the parameter space $r_p \in [20, 40]$, $\eta_{\text{fric}} \in [0, 1]$, and $nL^3 \in \left[2, \frac{1}{2}r_p\right]$ in the steady-state, and in conclusion proposed:

$$N_1 = \left(\mathsf{g_0} + \mathsf{g_1} nL^2 d\eta_{\text{fric}}\right) nL^3 \frac{\ln r_e}{r_e r_p} \mu_{fiber} \dot{\gamma} \tag{72}$$

The above equation is for well dispersed fiber suspension. The constant $\mathsf{g_0}$ term is added to account for the case of zero inter-particle friction. The least-squares fitted values of $\mathsf{g_0} \approx 0.18$ and $\mathsf{g_1} \approx 0.49$ was reported. Lindström & Uesaka used Mackaplow & Shaqfeh's [76] semidilute regime expression for μ_{fiber} (based on two-body theory) in eqn. (72). Mackaplow & Shaqfeh showed that the rheological properties of dilute through the dilute/semidilute transition, and into the semidilute suspension are well predicted by a dilute theory that takes into account two-body interactions. It should be pointed out that the expression for μ_{fiber}, eqn. (67) used in this research is given by Shaqfeh & Fredrickson's [104] multiple-scattering technique. The semidilute theory of Shaqfeh & Fredrickson is qualitatively similar to Mackaplow & Shaqfeh's simulation data for $nL^3 >> 1$ [76].

6.3 Transient viscosity and transient normal stress differences

In addition to studying the steady-state rheology of the suspension, it is interesting to determine the dynamics of rheological properties. It is also important to assure that those properties have reached steady-state before beginning to take data characterizing steady-state.

Figure 26 and figure 27 show the rheological properties – relative viscosity, μ_{rel}, the first and the second normal stress differences, N_1, and N_2, respectively (both scaled with $\dot{\gamma}\mu$) plotted against shear strain, $\dot{\gamma}t$. The values are calculated with Batchelor's theory using the LBM–EBF orientation data. These transient properties characterize

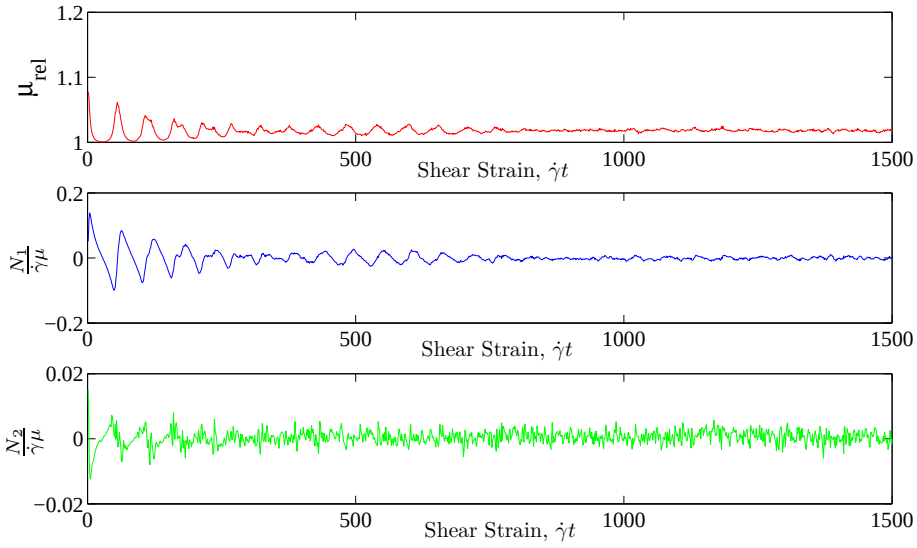

Figure 26: The relative viscosity, μ_{rel}^B, the first normal stress difference, N_1^B, and the second normal stress difference, N_2^B, plotted as functions of shear strain, $\dot{\gamma}t$, in the start-up of a steady shear flow (with constant shear rate, $\dot{\gamma}$). The suspension has concentration, $nL^3 = 5$ with fibers of $r_p = 32$.

the behavior of a suspension in start-up of steady shear flow. An important feature is that the structure development depends on the total strain, $\dot{\gamma}t$ imposed on the suspension and not on the shear rate or time separately. The structure remains unchanged during any intervals of flow cessation.

Figure 26 and figure 27 point out that at zero shear, the N_1 and N_2 are both zero, because the net effect of the normal components of the drag force on the fiber summed over all orientation configuration is zero. As the flow develops, the normal stress differences are finite for intermediate shear strain because of the oscillating stresses arising from the tumbling motion of the fibers, and the preferential orientation acquired by the fibers as a result of the bulk flow. Lipscomb [73] claimed that in dilute regime, for large aspect-ratio fibers ($r_p > 1$), the dimensionless time of shear, $t^* = \dot{\gamma}t/r_p$, needs to reach a value of $\mathcal{O}(1)$ in order to damp the oscillation of N_1. Transient theory for semidilute suspensions (Dinh & Armstrong [34], Atlan et al. [7]) predicts finite normal stresses with $\dot{\gamma}^2$ dependence during the inception of the steady

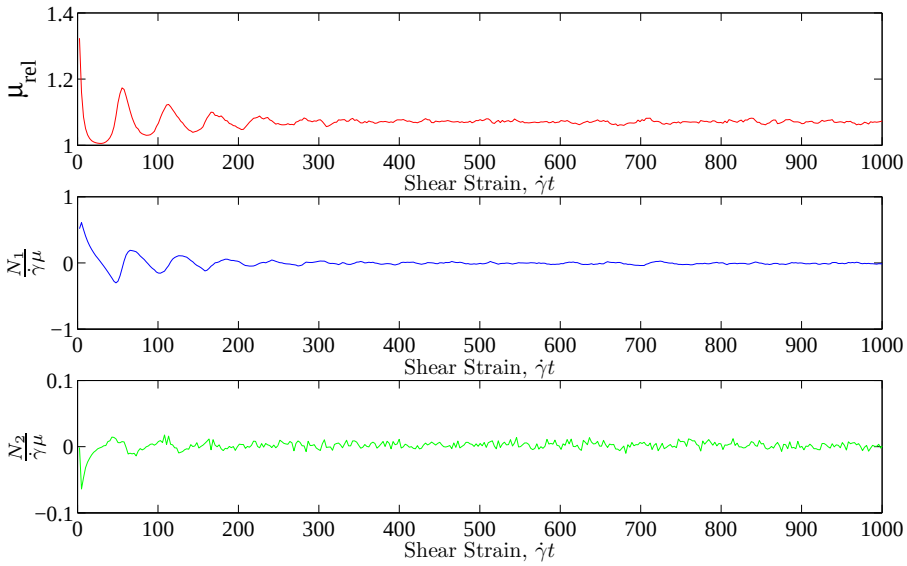

Figure 27: The relative viscosity, μ_{rel}^B, the first normal stress difference, N_1^B, and the second normal stress difference, N_2^B, plotted as functions of shear strain, $\dot{\gamma}t$, in the start-up of a steady shear flow (with constant shear rate, $\dot{\gamma}$). The suspension has concentration, $nL^3 = 18$ with fibers of $r_p = 32$.

flow, which completely disappear at a large shear strain value (at steady-state). But Atlan et al.'s [7] predictions showed the first normal stress difference would only reach zero at infinite strain. Dinh & Armstrong [34] approximates the actual hydrodynamic force on a fiber by a line integral along the axis of the fiber, and the thickness of the fiber is neglected. So at a large shear strain value, when the fiber is aligned into the plane of shear, it becomes invisible to the flow, and the tension in the fiber is removed. It causes the normal stresses to disappear, and also causes the suspension viscosity to approach the solvent viscosity [34]. However, the LBM–EBF simulation (which models the fiber with finite thickness), and other experiments have already shown evidence of non-zero normal stress differences at steady-state, as we discussed in § 6.2.

Figure 28 shows the transients of relative shear viscosity, μ_{rel}, for suspensions with fibers of aspect-ratio, $r_p = 32$ at different concentrations. At the inception of the shear flow, the zero shear viscosity is much higher than the steady-state viscosity

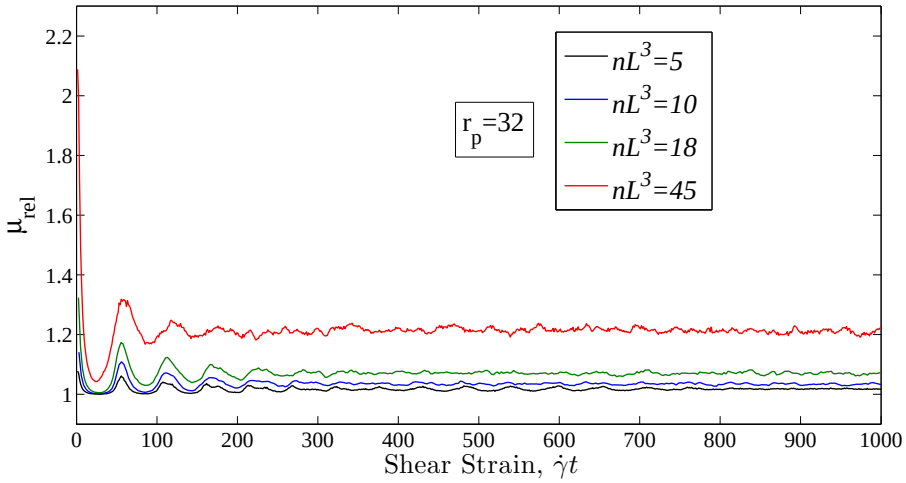

Figure 28: The relative viscosity, μ_{rel}^{B}, plotted as a function of shear strain, $\dot{\gamma}t$, in suspensions with different concentrations with fibers of $r_p = 32$. The relative viscosity is calculated with the Batchelor's theory.

due to the random fiber orientation at the assumed initial isotropic state set by the numerical simulation. At large strain, the fibers move to the plane of shear, and become more aligned to the flow direction, which causes the suspension viscosity to reduce from the initial isotropic value and to achieve the steady-state value.

CHAPTER VII

ROTATIONAL DIFFUSION IN HEADBOX FLOW

This research work continues with a numerical analysis of the rotational diffusion process for fibers flowing through a complex flow geometry, i.e. flow through a contracting channel geometry of the paper machine headbox. The principal objective in many scientific and industrial processes is to control the orientation states of fibers in contraction–type flows. For example, during the electrospinning of polymer based nanofibers, the suspension is fed through a small contraction called a spinneret, and the application of a strong electric field draws the suspension out through the contraction. This serves to align the polymer molecules in the flow direction. However, this study presented in this chapter is based on a similar but much larger-scale industrial process, namely papermaking. During papermaking, a fiber suspension is fluidized by turbulence created locally from a sudden change in geometry in an apparatus called a headbox. A schematic of the headbox is given in figure 29.

Upon exit from the contracting channel (headbox), the fiber suspension forms a plane liquid jet, which comes into contact with a moving permeable band or wire from which the water is drained and the paper is formed. Despite the longstanding use of such systems, many fundamental questions about the relationship between the operating state and the final fiber orientation distribution in the headbox remain unanswered.

Some previous studies investigated fiber orientations and rotational diffusion in a dilute suspension flowing through a headbox, where the rotational diffusion process occurs because of the randomizing effects of turbulent eddies. But it is hard to find analyses that address the interplay between the arranging effect of the velocity

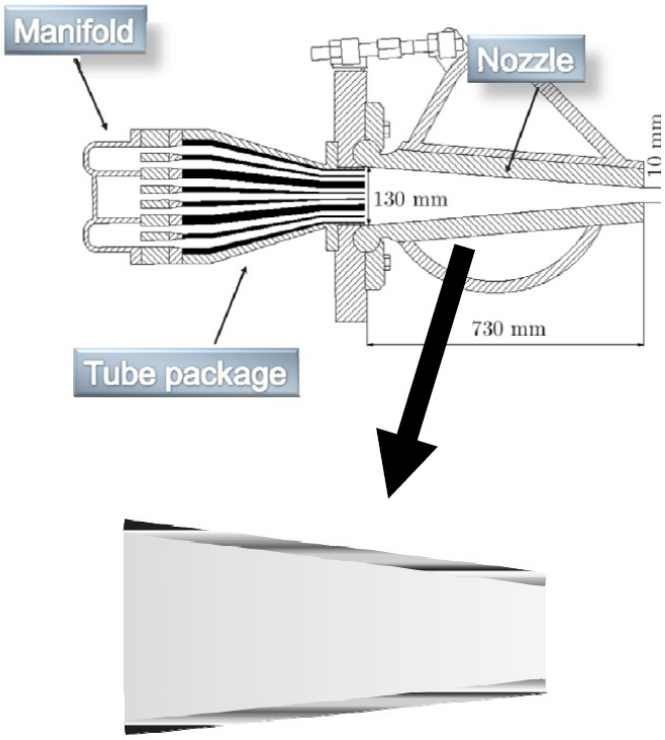

Figure 29: Schematic of modern hydraulic headbox. *Courtesy:* Smook [111].

gradient field and the randomizing effect of a rotational diffusion process that is induced solely by hydrodynamic interactions among fibers; there are no such analyses that include fiber–level numerical simulations. In order to understand these effects, LBM–EBF simulations are performed in a flow situation where the particle Reynolds number, Re_p, is considered to be asymptotically small, and the macroscopic Reynolds number, Re (based on the inlet channel height and local mean streamwise velocity, $Re = \frac{U_1 h}{\nu}$), is kept within $\mathcal{O}(1)$. The monodispersed fibers studied here are cylindrical in shape with a length and a diameter of $L = 1.52$ mm (9.6 LBM unit), and $d = 0.095$ mm (0.6 LBM unit), respectively, with $r_p = 16$, and the three concentration values in the semidilute regime under investigation are nL^3=8, 16 and 24.

7.1 Literature on headbox studies

Within the pulp and paper community, several researchers have analyzed the orientation behavior of pulp fibers in headbox flows. Ullmar [122] and Ullmar & Norman [123] measured the fiber orientation distribution in the plane of the paper at the headbox exit by digitally imaging nylon fibers in the suspension. These studies examined the effects of mean flow through the headbox, the headbox contraction ratio, CR ($\frac{\text{inlet height, } h_{in}}{\text{outlet height, } h_o}$), and concentration of the suspension on the orientation state of the suspension. Zhang [133] experimentally measured the fiber orientation distribution in both the plane of the paper (xz-plane in figure 31), and in the plane of contraction (xy-plane in figure 31) at several points along the central streamline of an asymmetric headbox, for a suspension well within the dilute regime ($c_v = 0.001\%$).

Olson et al. [84] analytically simplified the Fokker–Planck type equation by considering the flow of fibers along the central streamline of a linear contraction, and predicted the 2D orientation state of the fibers. They found the turbulence-induced rotational diffusion coefficient, D^r to be a constant ($D^r = 2\text{sec}^{-1}$) throughout the contraction by fitting the computations to the experimental data of Ullmar & Norman [123] and Zhang [133], respectively. Hyensjö et al. [55] extended the work of Olson et al. [84] by using single phase CFD modeling to predict the flow field along streamlines of a linearly contracting channel. Those results are used to compute the 2D fiber orientation distribution along individual streamlines of the flow in the absence of fiber–fiber interactions, and flow–fiber coupling. Parsheh et al. [85] used high speed imaging and laser doppler velocimetry (LDV) techniques to understand the effect of turbulence on the orientation anisotropy of a highly dilute suspension of rigid rods in a planar contraction. The turbulent intensity at the contraction inlet was varied, the orientation distribution along the centerline of the contraction was measured, and the results were compared to predictions that were based on the same Fokker–Planck type equation used by Olson et al. [84]. According to Parsheh et al.'s

[85] findings, the turbulence-induced rotational diffusion coefficient decays exponentially with the local channel contraction ratio and is influenced highly by the inlet turbulence characteristics.

Recently, Krochak et al. [66] experimentally studied an asymptotically low Reynolds number (based on fiber length-scale) flow of fiber suspension in a linear contraction. Index-of-refraction matched rigid glass fibers ($r_p = 50$) were used in dilute to semidilute suspensions. The orientation was measured along the centerline of the channel. The rotational diffusion in their experiments is induced by the hydrodynamic interactions among fibers. For theoretical model, they used the Fokker–Planck type equation derived by Olson et al. [84]. In that equation, for the case of hydrodynamic interactions among fibers, Krochak et al. represented the rotary diffusion process with either (i) Folgar & Tucker [43] constant (scalar interaction coefficient), C_I, ($D^r = \mathsf{C}_I\dot{\gamma}$) or (ii) Koch model [65]; when using the Koch model, only its isotropic part, eqn. (61a), was considered, with β_1 as an adjustable parameter. Krochak et al. developed an 'inverse solver method' (optimization routine) to estimate either the Folgar–Tucker constant, C_I or the β_1 parameter of the Koch Model by fitting the theoretical orientation distributions with the experimental results at the contraction exit (at the end of the contraction centerline). For both of these approaches, the diffusion coefficient was found to first increase with increasing suspension concentration up to a maximum, and then it would decrease with concentration above this point. This nonmonotonic behavior was attributed to fiber clumping or flocculation, a mechanism not considered in the relationships for the rotary diffusion coefficient.

As we discussed in § 5.4.3, Koch [65] proposed a constant value of the empirical constant, β_1 for simple shear flow. Krochak et al. attempted to find a best fit of this value from experimental results of linear contraction. Figure 30 shows these trends of β_1 with change of concentration for Poiseulle's flow through a linear contraction with comparison to the constant value assumed in simple shear flow. It is observed that the

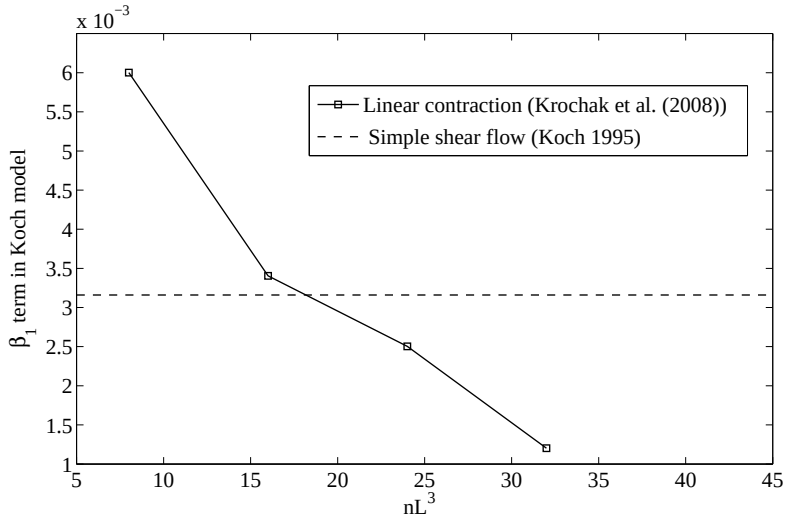

Figure 30: Adjustable parameter β_1 in the Koch model (eqn. (60)) for flow through linear contraction [66] for different nL^3 values with fibers of $r_p = 50$. The dashed line shows the constant value of β_1, for simple shear flow [65].

β_1 value decreases with increasing concentration in the linear contraction. This result is unexpected, since the effects of fiber concentration should be accounted for in the interaction rate term of the Koch model, i.e., the $\dfrac{nL^3}{\dot{\gamma}^2 \ln^2 r_p}$ term. This finding indicates that, at least for a linear contraction, the concentration dependence in eqn. (61a) is not quite appropriate. It should be clarified that the reason put forward by Krochak et al. [66] to drop the anisotropic term, (eqn. (61b), with another empirical constant β_2) of the Koch model was the enormous computational cost in evaluating that term which outweighed the marginal improvement in accuracy for rotary diffusion.

7.2 Specific objectives for LBM–EBF study of headbox

From the above review, it is clear that there are no fiber–level numerical analyses of the effects of fiber–fiber interactions on the orientation state of suspensions subject to flow within geometries typical of modern headboxes. Recently, Krochak et al. [66] provided the trend of the empirical constant in the isotropic part of the Koch Model in linear contraction through a combination of experimental and theoretical studies. However, Krochak et al. did not show the change of rotational diffusion with change

of contraction ratio, CR, along the centerline of the channel. The objectives for the study reported in this chapter are: (i) to directly predict the degree of fiber alignment inside the contraction for different concentrations with the LBM–EBF simulation, (ii) to numerically measure the rotary diffusion coefficient with Koch Model (isotropic part only) with the change of contraction ratio, for different concentration cases, (iii) to determine the interplay of aligning effect due to the increasing rate of strain along the contraction to the randomizing effect due to the rotational diffusion process of suspended fibers.

7.3 Academic headbox and boundary conditions in the simulation domain

A symmetric planar converging–diverging channel (the schematic of the simulation domain is shown in figure 31) is modeled with LBM–EBF simulation where the flow of the fiber is constricted only in the contracting section. The outflow fluid boundary condition at the throat is not known and that is why a diverging section is attached so that a periodic boundary condition could be imposed in the flow, x-direction. The contraction consists of two rigid sloping walls separated by $h_{in} = 17.42$ mm (110 LBM unit) at the inlet, and $h_o = 1.742$ mm (11 LBM Unit) at the throat, giving the maximum contraction ratio, $CR = 10$. The length of the contraction is $L_c = 44.175$ mm (278.5 LBM unit). The diverging section is a mirror image of the converging section.

Only the contracting section is seeded with fibers with an initial random distribution, and when the centroid of a fiber passes through the throat, the fiber re-enters from the inlet at the left, at a random position of the inlet cross section with a random orientation. The fiber images are periodic at the vorticity, z-direction. The fluid flow boundary conditions are periodic both in the flow, x-direction, and the vorticity, z-direction, respectively. A no-slip wall boundary condition (LB standard bounce back (SBB)) is applied in the gradient, y-direction.

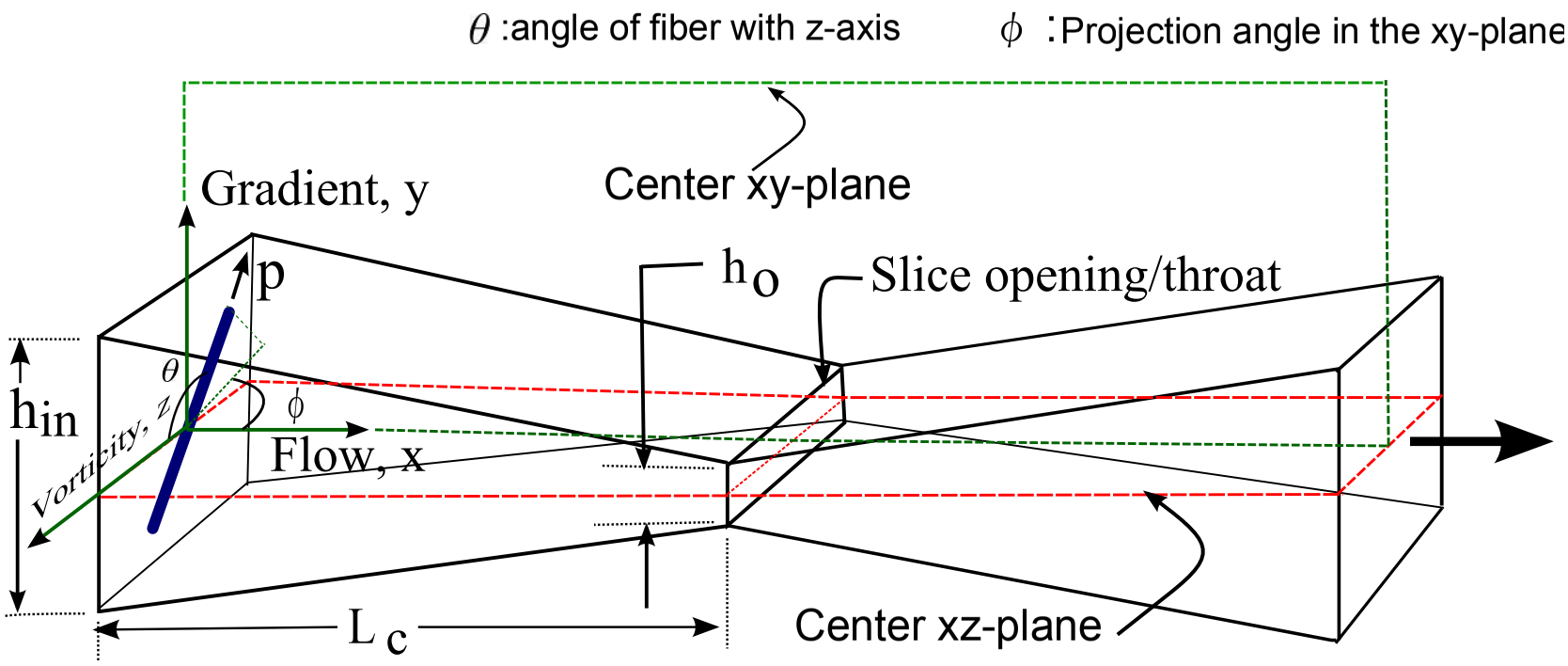

Figure 31: The orientation of fiber with respect to flow in the converging–diverging channel. **p** is parallel to the fiber's axis.

Figure 32 provides a visual representation of the actual simulation system, showing two simulation scenarios, one with a pure solvent, and the other with a suspension of fibers.

7.4 Region of analysis inside the contracting channel

Krochak et al. [66] used a Fokker–Planck type equation [84], which is applicable at the centerline of a planar symmetric converging shaped headbox. In order to use their proposed β_1 value in the Koch model, the analysis of the LBM–EBF simulation is also restricted to a certain region close to the centerline. Specifically speaking, the region of analysis is bounded by half fiber length, $0.5L$, from the centerline to the channel walls (both above and below the centerline on the xy-plane; see figure 33). The depth of this region is also half fiber length on both sides of the centerline (on xz-plane). The total length of the region is equal to the contraction length, L_c. All fibers observed within this region are then binned into their corresponding spatial cells along the x-axis according to the position of the center of area of each observed tracer fiber. For the present study, there are 29 cells along the central streamline, with a length of one fiber, L (9.6 LBM unit) each.

7.5 Results and discussion

To help understand the findings of this numerical simulation, and to characterize the evolution of the orientation distribution, it is instructive to first discuss the degree of alignment of the fibers along the contraction centerline. The degree of fiber alignment (orientation dispersion) about the principal direction of orientation can be defined by $\langle cos^2\phi \rangle$.

Figure 34 shows a plot of $\langle cos^2\phi \rangle$ for all concentrations tested numerically with LBM–EBF simulation. To clarify the findings, it is to be noted that, a high value of $\langle cos^2\phi \rangle$ corresponds to a highly aligned orientation state, and a low value of $\langle cos^2\phi \rangle$

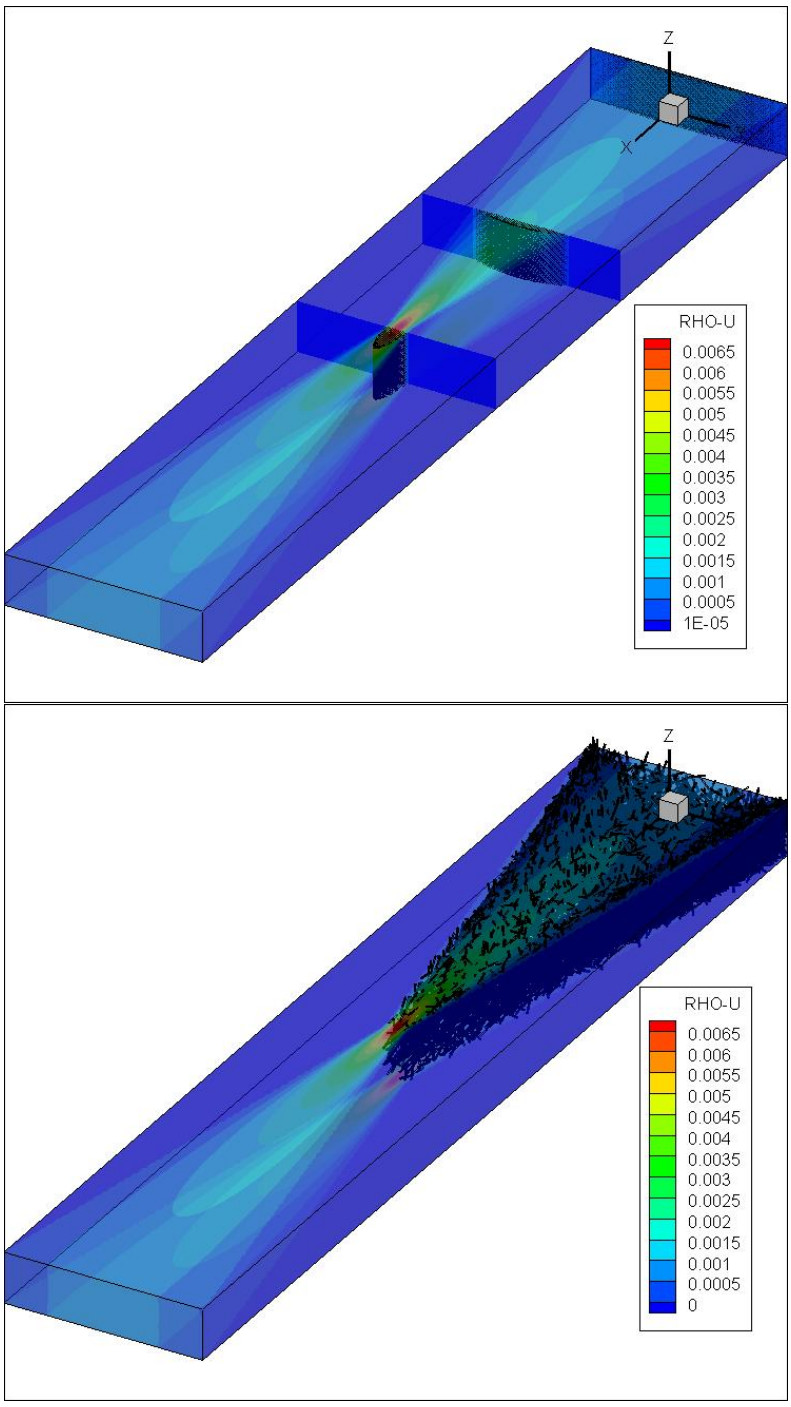

Figure 32: The LBM–EBF simulation snapshot at steady-state: (top figure) Contour plots and the velocity profile in the converging–diverging channel for a pure solvent. (bottom figure) A suspension of $nL^3 = 16$ with fibers of $r_p = 16$. Only the converging section is seeded with fibers, for computational efficiency.

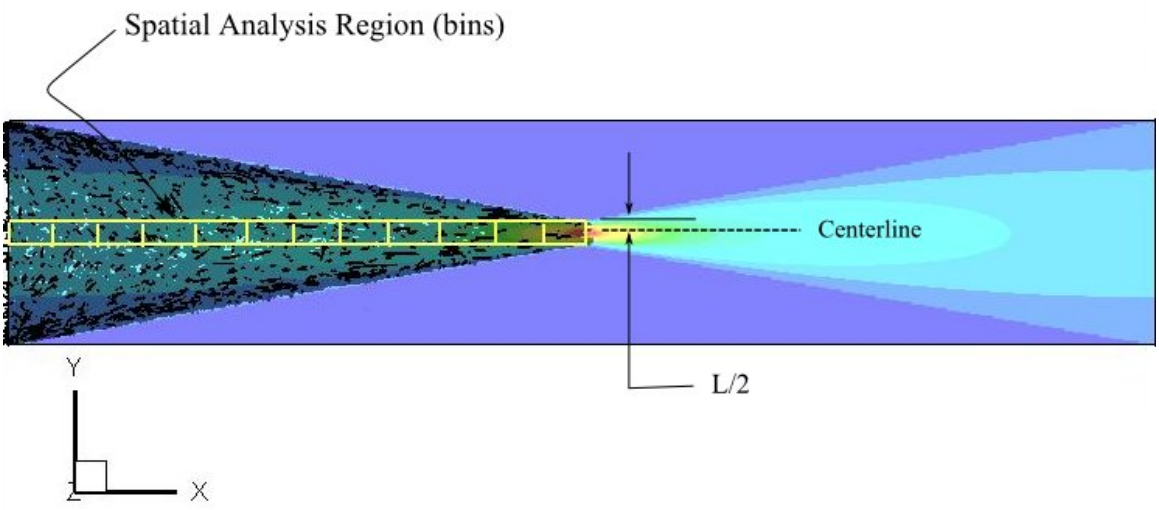

Figure 33: The region bounded by the yellow unit cells represents the analysis region. All fibers observed in this region are used for the determination of C_I, and $\langle cos^2\phi \rangle$.

corresponds to a more random orientation state. The first observation made from figure 34 is that the difference in $\langle cos^2\phi \rangle$ at the contraction exit is small but nonetheless unique for each concentration. At the inlet, however, we see that the degree of fiber alignment is slightly higher for the two higher concentrations ($nL^3 = 16$ and 24) than for the lowest concentration ($nL^3 = 8$) case. An argument can be made that this condition results from flocculation or mechanical entanglement which hinders fiber movement; however, Krochak et al.'s [66] findings showed that the flocculation effect was much more prominent at a higher concentration, $nL^3 = 32$. However, in this study we were unable to simulate such a high concentration in a headbox geometry because of computational limitations, and thus can not comment on the relative increase in the degree of fiber alignment when the concentration reaches $nL^3 = 32$.

Next in figure 35, the variation of scalar interaction coefficient, C_I, with change of concentration is numerically studied using the Koch model (isotropic part only). To evaluate the dependence of C_I on concentration with the Koch model, the suitable β_1 values (corresponds to figure 30) for a linear contraction at different concentrations

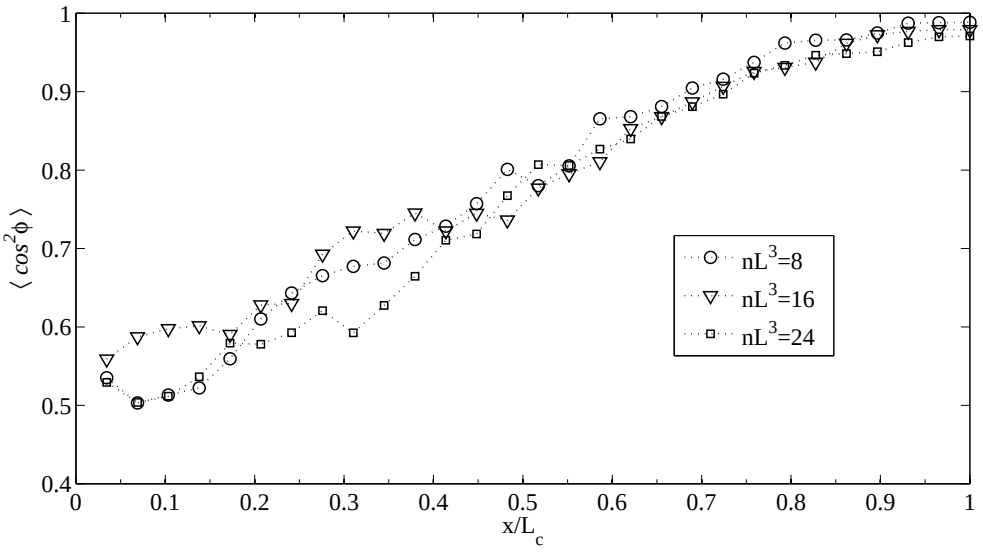

Figure 34: Plot of degree of fiber alignment $\langle cos^2\phi \rangle$ (for fiber aspect-ratio, $r_p = 16$) along the contraction length for different concentrations.

are used. The 4th order moments are calculated with the LBM–EBF fiber orientation data. The scalar measure of the interaction coefficient is extracted from the Koch model as $\mathsf{C}_I = \frac{1}{3}(\text{tr } \mathbf{C})$. These results are compared with the scalar interaction coefficient, C_I, or alternately called the Folgar–Tucker constant given by Krochak et al. [66]. To reiterate, Krochak et al. performed an optimization routine to estimate the Folgar–Tucker constant, C_I, based on experimental data measured just prior to the contraction exit. This parameter is evaluated near the exit because the suspension becomes highly aligned in this region. As a result, the second order terms in the Fokker–Planck equation play their most significant role in this region, for fiber orientations parallel to the central axis. Hence, the accuracy of C_I was most critical near the exit, but nonetheless, a good agreement was also maintained throughout the earlier stages of the contraction [66].

Now from figure 35 it is seen that the scalar interaction coefficient increases with concentration up to a nL^3 value of 24, for both the Koch model and Krochak et al.'s implementation of the Folgar–Tucker model. The order of magnitude of C_I for

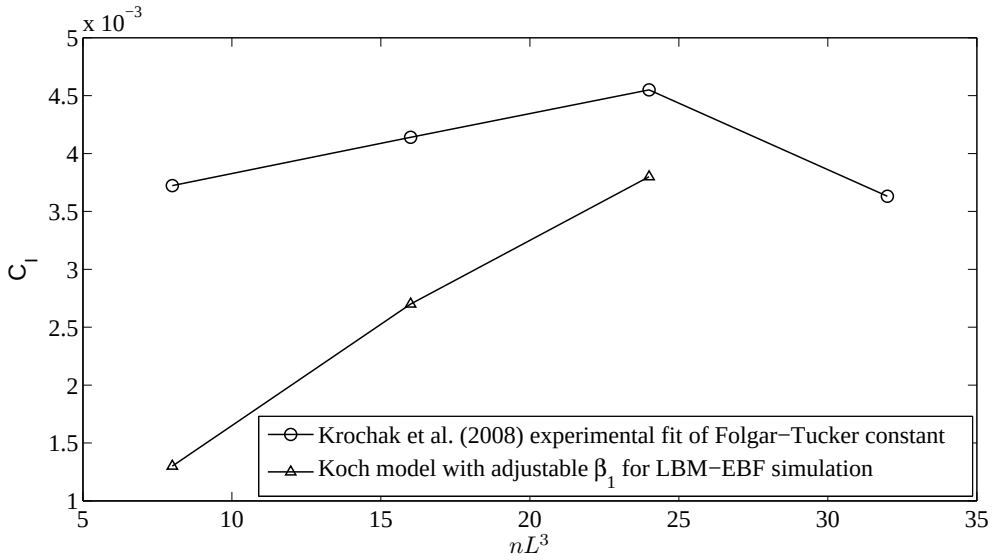

Figure 35: Scalar interaction coefficient at the contraction exit for different concentrations. The fiber aspect-ratios used in the experiments of Krochak et al. [66], and in the LBM–EBF simulations are $r_p = 50$ and 16, respectively.

both these models remains within $\mathcal{O}(10^{-3})$. Interestingly, Krochak et al. found a dramatic decrease in C_I, for their highest concentration, $nL^3 = 32$ in the headbox geometry. This observation can be supported by the 'caging effect' proposed by Doi & Edwards [36], where the 'cage' formed by neighboring fibers prevents each fiber from rotating freely. This effect was probably compounded with the aligning effects of the accelerating flow inside the contraction, which forced the fibers into a highly aligned state. As a result, fiber mobility was significantly reduced. As we have mentioned once before, the LBM–EBF simulations can not be carried out for $nL^3 = 32$ due to computational memory requirements, beyond the capabilities of the shared memory computers used in this study, and hence numerical results can not be generated for this higher concentration case.

The relative importance of rotational diffusion to the rate of strain can be effectively defined by a rotational Peclet number, $Pe = \frac{\dot{\gamma}}{D^r}$, where $\dot{\gamma}$ is a scalar magnitude of the rate of strain tensor as defined in § 5.3. Figures 36 – 38 show the trends of C_I (with the Koch model), and rotational Peclet number, Pe, along the contraction

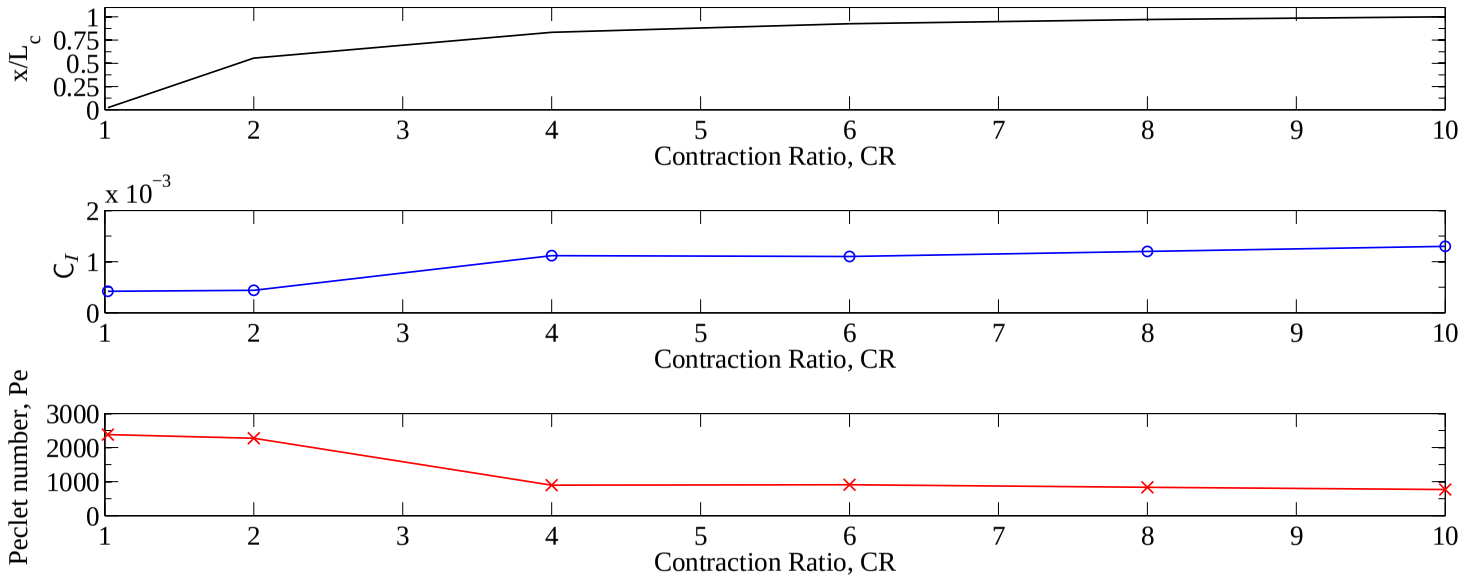

Figure 36: Trends of the rotational diffusion coefficient, C_I (with the Koch model), and the rotational Peclet number, Pe, with the change of contraction ratio, CR, along the contraction centerline, respectively. The suspension has an nL^3 value of 8, and the fibers are of $r_p = 16$.

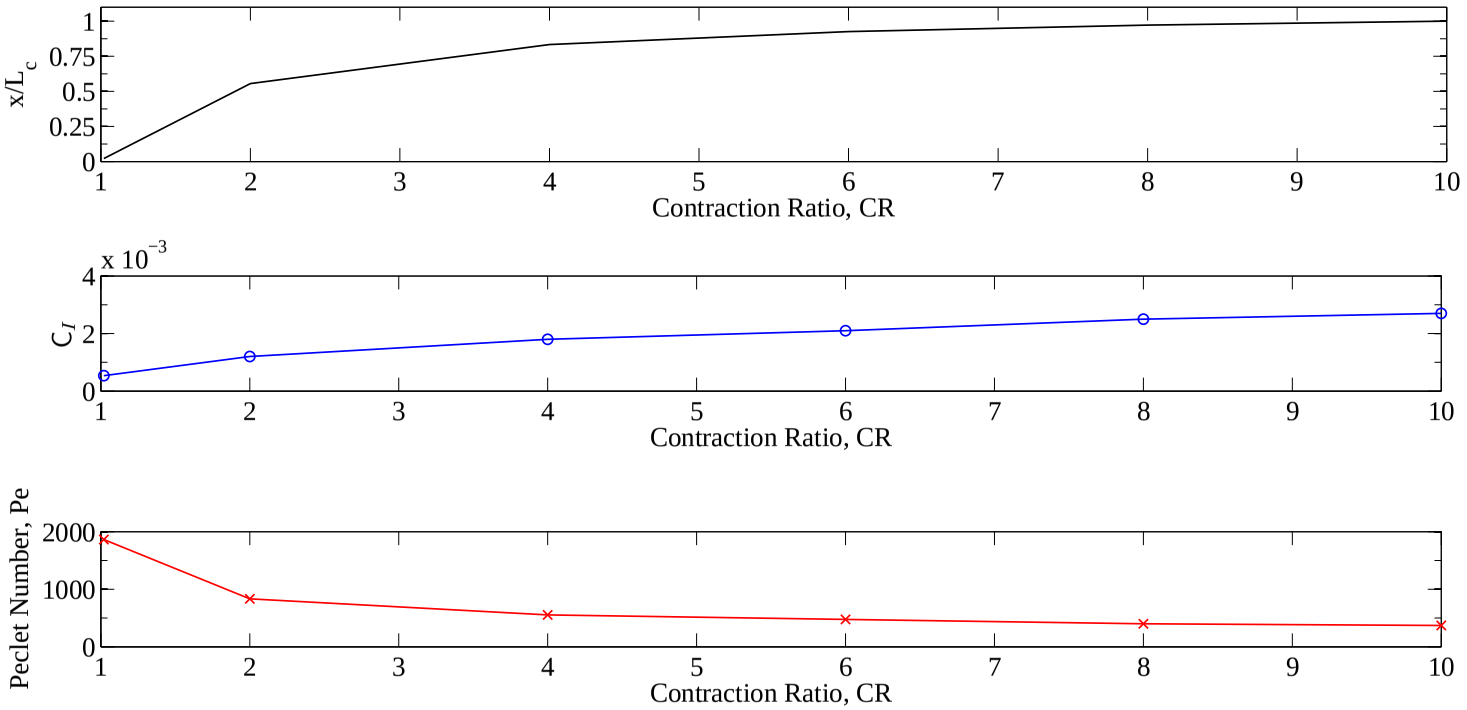

Figure 37: Trends of the rotational diffusion coefficient, C_I (with the Koch model), and the rotational Peclet number, Pe, with the change of contraction ratio, CR, along the contraction centerline, respectively. The suspension has an nL^3 value of 16, and the fibers are of $r_p = 16$.

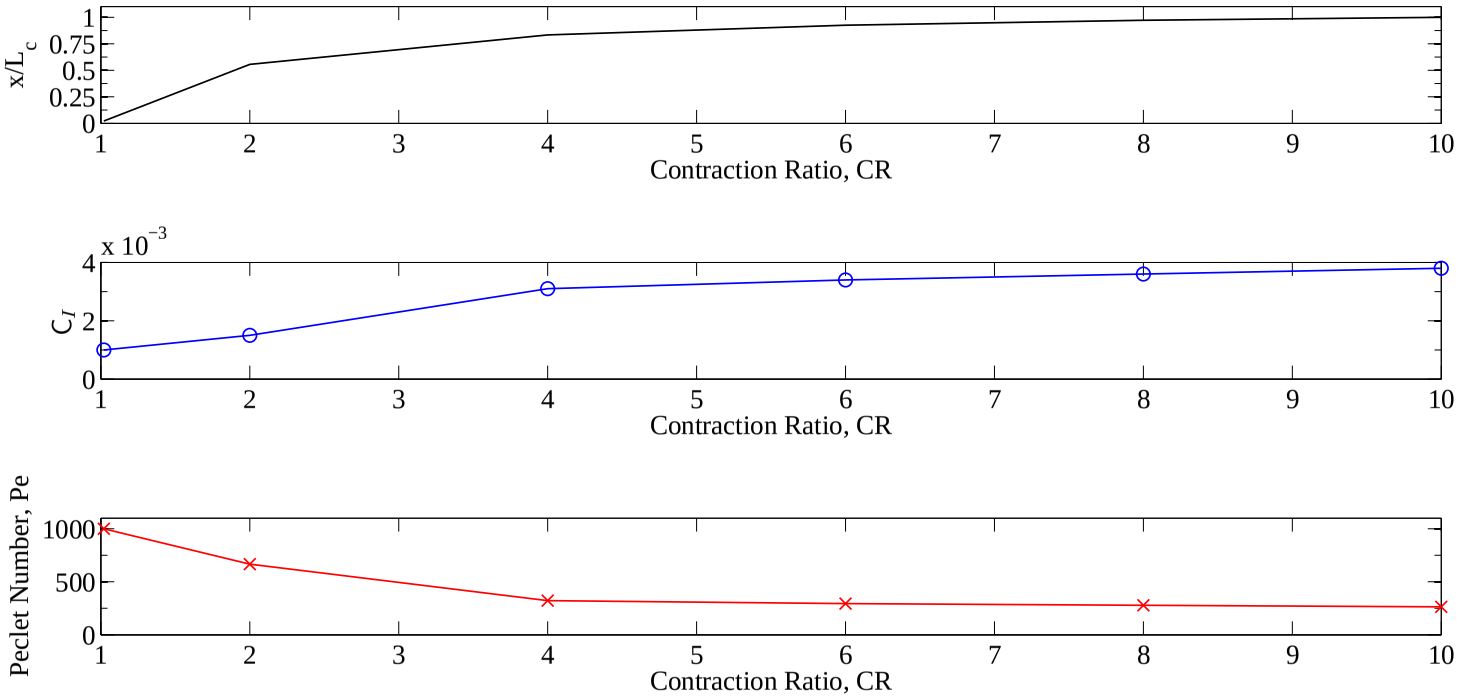

Figure 38: Trends of the rotational diffusion coefficient, C_I (with the Koch model), and the rotational Peclet number, Pe, with the change of contraction ratio, CR, along the contraction centerline, respectively. The suspension has an nL^3 value of 24, and the fibers are of $r_p = 16$.

centerline, for different concentrations with the same fiber aspect-ratio, $r_p = 16$. It is observed that, C_I increases at a relatively faster rate until $CR \leq 4$ (corresponds to $x/L_c = 0.8333$), and then there is a gradual increase up to the throat of the contraction ($CR_{max} = 10$ and $x/L_c = 1.0$); whereas, the rotational Peclet number, Pe, decreases at a relatively faster rate until $CR \leq 4$, and then there is a gradual decrease up to the throat of the contraction. These behavior can be explained by studying the change of the scalar measure of strain-rate, $\dot{\gamma}$ along the contraction centerline.

Figure 39 shows an example of the change of $\dot{\gamma}$ along the contraction centerline for the suspension with $nL^3 = 8$ and $r_p = 16$. Similar trends have been observed for $nL^3 = 16$ and 24 as well. It is seen that until $CR \leq 4$, the $\dot{\gamma}$ is quite low and increases almost linearly. As a result the randomizing effect of hydrodynamic interactions among fibers dominates and significantly offsets the aligning effect imposed by $\dot{\gamma}$. Consequently, in this range of lower contraction ratio, the rotational diffusion increases at a faster rate by maintaining its dominance over the corresponding rate of strain and also the rotational Peclet number, Pe, decreases rapidly.

Now from figure 39 it is obvious that, for $CR > 4$, the $\dot{\gamma}$ becomes stronger and increases at a much faster rate than it is observed in the upstream portion of the flow. The rotational diffusion still can dominate the aligning effect of $\dot{\gamma}$, but not as strongly as was possible for $CR \leq 4$. This is manifested by the gradual decrease of the rotational Peclet number, Pe, up to the channel throat. It is interesting to contrast the decreasing trend of rotational Peclet number, Pe, for the hydrodynamic interaction induced rotational diffusion in the semidilute regime (as observed in the LBM-EBF simulation), to increasing trend of the rotational Peclet number, Pe, for the turbulence-induced rotational diffusion in dilute regime (as observed in the experiments of Parsheh et al. [85]) in a headbox. Parsheh et al. [85] reported that the Pe increases with the increase in contraction ratio, CR, since turbulent energy decays as the mean rate of strain increases with increasing CR; so with increasing CR, the

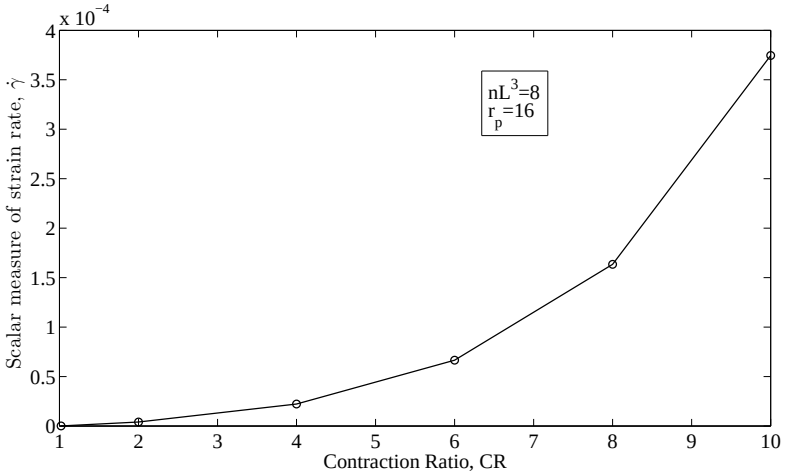

Figure 39: Scalar measure of strain-rate, $\dot{\gamma}$ along the contraction centerline.

rate of strain always dominates fiber orientation and offsets the randomizing effect of turbulence. However, in the present study it is found that the rotational diffusion due to hydrodynamic interactions among fibers is the predominant term over strain rate in the semidilute regime and results in a decreasing trend of rotational Peclet number, Pe along the contraction centerline.

7.6 Summary of headbox study

This chapter explored the orientation states of fibers in a semidilute suspension flow through a linearly contracting channel. The orientation behavior of the fibers is explained by observing the interplay between the mean rate of strain and the hydrodynamic interaction induced rotational diffusion process for the fibers in such a suspension system. To measure the rotational diffusion with the Koch model for different concentrations, the β_1 parameter is adopted from the experimental investigation of Krochak et al. [66]. The scalar interaction coefficient, C_I, extracted from the Koch model is shown to remain within $\mathcal{O}(10^{-3})$ from contraction inlet to outlet (throat). The C_I increases with concentration up to $nL^3 = 24$. Experimentally, at higher concentrations ($nL^3 = 32$), the C_I decreased due to fiber flocculation; but this observation could not be verified by numerical LBM–EBF simulations, due to

computational limitations. An interesting finding from this study is that the rotational Peclet number, Pe, decreases with increase of the contraction ratio, CR, when the rotational diffusion is driven by hydrodynamic interactions among fibers. This finding shows the opposite trend to the observations made in the dilute regime with a turbulence-induced rotational diffusion process [85].

CHAPTER VIII

CONCLUSIONS AND FUTURE RECOMMENDATIONS

8.1 Summary

The numerical simulations presented in this research have enabled us to find a number of intriguing results which altogether provide a coherent physical picture of the non-colloidal fiber orientation behavior and fiber rotational diffusion in a semidilute suspension flow.

In this study, the LBM–EBF simulations rendered the time-dependent fiber orientation distribution, and the steady-state time averaged values were found from those simulations. The investigation has spanned a parameter two-space ($r_p \times nL^3$) or alternately, ($r_p \times c_v$). Unlike some previous numerical fiber–level simulations reported by other research groups, the LBM–EBF simulations in this research correctly predict the orbit constant distribution of fibers in a semidilute suspension flow. It is seen that the peaks of the orbit constant, C_b-distributions, fall within a range of $0.15 < C_b < 0.4$, which is consistent with the experimental results of Stover et al. [115]. The simulations have demonstrated that anisotropic rotational diffusion is required to describe fiber orientation in an anisotropic flow field where hydrodynamic interactions among fibers are dominant. The simple anisotropic weak diffusion model 'A.W.D.M.' is fitted with the LBM–EBF predicted $p(C_b)$ and interestingly, it was found that, although such a model representing weak rotational diffusion can describe the C_b-distribution very well, the model fails to describe the asymmetry in the ϕ-distribution across the xz-plane observed in the semidilute regime. The asymmetry in the ϕ-distribution can be attributed to the presence of a small but detectable number of mechanical contacts (non-hydrodynamic interactions) among fibers in the semidilute regime. From this

study, the need for a more sophisticated diffusion model to describe fiber orientation in the semidilute suspension has become eminent.

Koch [65] proposed a robust rotational diffusion model of a hydrodynamic interaction induced rotational diffusion process for fibers in a semidilute suspension flow. This model gives a full three dimensional spatial tensor ($\mathbf{C}$) representation of the rotational diffusion. The applicability of the Koch model has been largely unexplored in the previous literature. In order to use the Koch model to evaluate the rotational diffusion tensor, the LBM–EBF simulation data is used to calculate the 4th and 6th order orientation moments. Evaluation of this tensor shows that at a specific c_v and r_p the off-diagonal components of the diffusion tensor are $O(10^{-2})$ to $O(10^{-3})$ smaller than the largest diagonal component, in a simple shear flow. A scalar measure of rotational diffusion, C_I (standard Folgar–Tucker Constant extracted from $\mathbf{C}$) reveals that the rotational diffusion increases either with the decrease of the fiber-aspect ratio (keeping nL^3 constant) or with the increase of the volume concentration (keeping r_p constant) in the semidilute regime. This trend is explained by reasoning that the interactions among fibers become more frequent with either of these scenarios mentioned above, consequently increasing the deviations of fibers' orbits from the initial Jeffery's solution [59] and ultimately causing an increase in C_I.

These observations discussed above support an important conclusion: the range of C_I ($0.0038 \sim 0.0165$) reported by Folgar & Tucker [43] is overly diffusive. The true order of magnitude is $\mathcal{O}(10^{-4})$, as observed with the present LBM–EBF simulations and with experiments of Stover [113] as well. In this research the anisotropic diffusivity model (namely the Koch model) is implemented into the fiber orientation evolution equation. The limitations of using the Koch model in the evolution equation (general 'ARD' model, eqn. (58)) are exposed and an alternative spherical harmonics based approach [80] has been introduced.

The study of rheology of a sheared semidilute fiber suspension with the LBM–EBF simulation proves that even the maximum specific viscosity, $\mu_{sp}^{B,max}$, permissible within the framework of a hydrodynamic theory (Batchelor's theory) underpredicts the experimental result of Bibbo [17] in the semidilute to transition of semidilute to concentrated regimes. The LBM-EBF simulation helped to explain the reason behind this discrepancy. The direct computational measurement of rheological properties with the LBM–EBF simulation match the experimental relative viscosity, μ_{rel}, reported by Bibbo; since the simulation can account for the transmission of stress due to a small but finite amount of mechanical fiber–fiber interactions in the semidilute regime. These mechanical contacts increase the viscosity of the suspension. The first normal stress difference, N_1, is evaluated with the LBM–EBF simulation, and the results proved that Carter's [24] formula for predicting N_1 fails in the semidilute regime. But as volume concentration increases – Carter's formula becomes more accurate, so that the experimental and simulated first normal stress differences fall onto the same curve, whose slope is close to K (≈ 0.08).

As in previous studies using the LBM-EBF simulation [128, 126, 127], the bulk of the simulations presented here are performed in simple shear flows. However, this work has extended the LBM–EBF code to simulate complex flow conditions. A study of rotational diffusion of fibers in semidilute suspension flowing through a linearly contracting channel is performed. It is found that the rotational diffusion due to hydrodynamic interactions among fibers is the predominant term over strain rate in an asymptotically low Reynolds number flow and results in a decreasing trend of rotational Peclet number, Pe along the contraction centerline.

8.2 Recommendations for future Research

8.2.1 Experimental research

To complement the fiber–level simulations, numerous experimental research themes may be investigated to gain a better understanding of fiber orientations and interactions in the suspensions. These can include flow visualization, determining individual fiber properties, and various rheological studies, etc. § 3.2.6 described a limitation of the current contact model in the LBM–EBF simulation as its inability to imitate different kinds of contacts among fibers resembling the actual scenario. To address this problem, experimental study of fiber–fiber interactions should be pursued. This may include a visual investigation of two fibers in contact in order to determine the effects of surface structure and fiber interactions on the relative fiber motion. In Stokes flow, the force driving the fibers together is very small and it is likely that contact will only occur between asperities on the surfaces of the two fibers.

A direct indication of the magnitude of the adhesive force, F_a between two fibers can be obtained experimentally by observing the interaction of a fiber with a long strand of the same material [26]. The one end of the long starnd should be attached to a disk, connected to a servomotor and the assembly would have to be immersed in fluid flow cell. A single fiber can be introduced into the fluid for example using a thin rod or clamping device and can be maneuvered to bring it as close as possible to the long strand. The strand should then be translated toward the fiber at very low velocity. When contact is suspected to have occurred (can be monitored with a CCD camera), the velocity of the strand should be reversed and set to its minimum value. An established adhesive contact would drag the fiber along with the strand. By slowly increasing the velocity step by step, the minimum velocity, U_d for detachment can be determined. Since in Stokes flow, the inertia of the fiber and fluid is very small, the adhesive force between the fiber and strand balances the hydrodynamic drag exerted on the fiber and from that a measure of F_a can be determined. Chaouche & Koch

[26] used a similar technique and measured the adhesive forces between nylon fibers in different grades of silicone oil and also in mixtures of water/glycerol solutions. It has been seen that the adhesive force is very sensitive to the chemical nature of the solvent but is independent of fluid viscosity. The force is nearly independent of fiber length but increases with increasing fiber diameter. However, in their experiments, a point contact is created. In suspensions, fiber surfaces can be in shearing motion with each other. The experimental setup has to be designed to create such contacts. The nature of the adhesive force for these types of scenarios can help to improve the contact model in the simulation.

The adhesive force at the contact region between two fibers may be related to colloidal forces which depend upon the physical and chemical properties of the solvent and the surface of the fibers. Chaouche & Koch [26] proposed a dimensionless number, $\alpha = 2\pi\mu\dot{\gamma}d^2/\left[\ln(2r_p)F_a\right]$, where F_a is the adhesive force. The ratio of the viscous and contact torques defines α. The shear thinning behavior can be quantified by α – within the framework of breakage and formation of fiber flocs. For $\alpha > 1$, the suspension is Newtonian and for $\alpha < 1$, the suspension is shear-thinning. The experiments of Chaouche & Koch were conducted with the aim to understand fiber–fiber contacts and shear-thinning behavior of polymeric suspensions commonly used in composite processing industries. Similar analyses can be performed e.g. with bleached hardwood (birch) kraft pulp and bleached softwood (douglas fir) kraft pulp, which are common fiber types in pulp-paper industries.

Adopting a new approach for flow visualization can improve the quality of experimental measurements in semidilute to concentrated regime as well. The classical method for visualization of transparent fibers [43] and the index-of-refraction matching method [115] using a planar light source are inadequate for a cylindrical body. To overcome this problem and for the clear visualization of transparent polymeric fibers oriented in all directions in a dilute/concentrated suspension, Yasuda et al. [131]

proposed to use birefringence of a fiber. They visualized fibers in a concentrated suspension employing a combination of fibers without birefringence (CAP fibers similar to Stover et al.'s [115] experiments) as primary fibers and those with birefringence (vinylon) as tracers. Only the fibers with birefringence were visualized in a concentrated suspension between rotating at high speed crossed polarizers. This method produced improved image quality although it has certain limitations [131]. For future experiments, this visualization technique can be a very good option to consider.

8.2.2 Simulations

The current LBM–EBF simulation may be used to probe additional variables in the parameter space for *rigid* fiber suspension; studies might consider fibers of various cross sectional shapes, permanently deformed fibers, distributions of fiber shapes and lengths, and friction among fibers, to name a few. Multiple initial configurations could be included to gain better statistical data. Additionally, § 3.2.3 proposed improving the LBM–EBF method by including a proper body force term (representative of an unsteady and spatially varying surface body force such as the EBF) in mesoscale. This suggested improvement needs to be incorporated in the code in future.

A shortcoming of the present fiber–level simulations to simulate a realistic suspension for paper manufacturing is that these simulations still neglect fines, fillers and the fibrillation of the fiber surfaces. These are features of a markedly smaller length scale, and computational requirements would be huge to account for them directly. Yet, their effects on paper-forming are known to be non-negligible, and in some respects dominant. This remains a formidable problem for future research.

The study of the rotational diffusion of flexible fibers is consciously avoided in this work, since the rotational diffusion mechanism in rigid fiber suspensions is poorly understood as yet. In future, it is advisable to study Jeffery's orbital drift for a single flexible fiber, before trying to analyze the rotational diffusion of flexible fibers

in suspension. The concept of orbit constant is 'ill-defined' for flexible fibers – as commented by Skjetne et al. [110], since the geometry of a flexible fiber vary with time. Experiments of Arlov et al. [11] in a Newtonian shear flow show the trend of unstable Jeffery's orbit – where orbit constant, C will tend to drift (for the most part) either to 0 or to ∞, depending on the initial C value, with intermediate values also being observed. Although, Wu & Aidun [126, 127] studied flexible fiber suspension with LBM–EBF simulation, no analysis has been performed to verify or to explain the above mentioned phenomenon. So this could form the basis of a study of rotational diffusion for flexible fibers with the LBM–EBF simulation; but this is left for future exploration.

Some of the studies which have been carried out in this PhD work, although extremely interesting, have not provided many solid answers. In studying the rotational diffusion in linear contracting channel numerically, the unknown proportionality constant in the Koch model, i.e., β_1, in eqn. (61a) is taken to be a function of fiber concentration, relying on the experimental study of Krochak et al. [66]. But from a modeling standpoint, it is not helpful to find that β_1 has a concentration dependence in linear contraction; it makes modeling of rotational diffusion in such a geometry much more challenging, given that the representative rotational diffusion model by Koch already contains concentration dependency in the nL^3 part of eqn. (60). This suggests that the rotary diffusion coefficient does not scale with nL^3, but perhaps with some other combination of n, L, and d. This finding is unfortunate in a way that, it would be highly desirable from a modeling perspective to be able to determine a proportionality constant once for a particular flow, then be able to reliably predict the effect of varying other parameters without measuring a new proportionality constant. So at least for the diffusion coefficient investigated with the Koch model, the coefficient must be determined empirically for a given set of suspension parameters and a flow field. This observation is also true, for the standard Folgar–Tucker model.

In future, a valuable study can be conducted to determine the correct scaling for the rotary diffusion coefficient which can possibly eliminate this problem. Phan-Thien et al. [89] pursued to develop a numerical correlations between the scalar interaction coefficient C_I and the concentration parameter $c_v r_p$ (instead of using nL^3) in the semidilute regime for simple shear flow. For a headbox flow, a similar initiative may be undertaken to propose such a correlation. Unfortunately, such an attempt is frustrated by the computing demand, which right now can not be met through the shared memory computing system used in this research. The LBM–EBF code is suitable only to be run at a shared memory computer, and therefore, conducting a large number of numerical experiments to put a sufficient number of points on the parameter space, will only be feasible when the code is run on distributed memory machines.

8.2.3 Improvement of code performance

It is imperative to improve the efficiency and performance of the simulations by running at large distributed memory clusters, utilizing full parallelization based on the Message passing interface (MPI). But it should be noted that, recent high-performance computing (HPC) machines contain multicore chips, tied together into (multi-socket) shared memory nodes as the machine building block. As a result, it is also important to fully harness intra-node performance in order to leverage the enormous computational potential of emerging multicore-based supercomputers.

Although it is relatively easy to quantify the absolute and the relative performance, it can be very difficult to quantify how much further potential performance improvement is possible. In view of that, the 'roofline performance model' proposed by Williams et al. [124] is discussed here, which allows users to quantify how much performance is left on the table. Thus, with this model, not only can absolute performance be quantified, but also the success can be judged.

The roofline model is premised on the belief that the three fundamental components of performance are communications, computations and locality. The model relates processor performance to off-chip memory traffic. The rates associated with these two quantities are peak performance (Gflop/s) and peak bandwidth (Gb/s), respectively. Every kernel has a locality metric termed as *operational intensity*, which indicates floating-point operations per byte of DRAM traffic. The bytes transferred between the cache and the memory are of importance, rather than the traffic between processor and cache. Thus operational intensity (OI) suggests the DRAM bandwidth needed by a kernel (e.g. the LBM–EBF) on a particular computer. So the performance can be estimated as:

$$\text{Attainable Gflop/s} = \min \begin{cases} \text{Peak floating point performance (Gflop/s)} \\ \text{Peak mem. bandwidth (Gb/s)} \times \text{OI} \end{cases} \tag{73}$$

The roofline performance study has been carried out by running the LBM–EBF simulation with OpenMP directive in one socket of a single node of Teragrid NCSA-Abe cluster. Each node in NCSA-Abe cluster is built on Intel's microarchitecture building block (dual-socket×quad-core Intel Xeon E5345 Clovertown). Each core runs at at 2.33 GHz. The peak double-precision performance per socket is therefore, 37.28 GFlop/s. Each core includes a 32KB L1 cache, and each chip (two cores) has a shared 4MB L2 cache. The peak memory bandwidth for each socket is 5.9 Gb/s.

To construct a roofline for Intel Xeon E5345, a horizontal line can be drawn showing peak floating-point performance (37.28 GFlop/s) for a socket. Obviously, the actual floating-point performance of a floating-point kernel can be no higher than the horizontal line, since that is a hardware limit. A second line can be drawn that gives the maximum floating-point performance that the memory system of that one socket can support, for a given operational intensity. According to eqn. (73), these two lines intersect at the point of peak computational performance (37.28 GFlop/s), and peak memory bandwidth (5.9 Gb/s). Figure 40 shows the roofline for a single

socket of Intel Xeon E5345 Clovertown. A log–log scale is used for the plot. Note that, this roofline is kernel independent.

The performance measurement tool 'PerfSuite' is used in this work to find out the operational intensity (OI) of the LBM–EBF kernels. The event 'PAPI_L2_TCM' together with event 'PAPI_TOT_CYC' reported the total memory traffic (L2 cache misses) and the event 'PAPI_FP_OPS' reported the total flop/s performed by the kernel. Now if OI is visualized as a column that hits the roof, either it hits the flat part of the roof indicating the performance is compute bound or it hits the slanted part of the roof, which means performance is ultimately memory bound. In the top plot of figure 40, a red dotted column is drawn, which reveals the OI of the single phase LBM–EBF kernel to be bound by memory and the value of this OI is 0.263. The yellow circle on the column marks the actual achieved Gflop/s by the kernel. The attainable flop/s is the point where the column hits the roofline. So according to this result, approximately 15% performance gain is still possible. Note that, this OI corresponds to the case when hardware prefetching is disabled. When hardware prefetching is activated, the L2 cache miss reduces and hence the OI increases slightly as indicated by the solid blue column in the plot (slightly to the right of red dotted column), giving rise to the possibility of additional performance gain.

A similar analysis has been performed with the multiphase LBM–EBF kernel. The bottom plot in figure 40) demonstrates that result. The operational intensities for this kernel are higher than those of the single-phase kernel for corresponding hardware prefetching disabled or enabled scenarios respectively. It is found that, for multiphase LBM–EBF kernel, approximately 25% performance gain is still achievable. It should be noted that, Williams et al. [124] tested 16 combinations of different types of kernels (LB magneto-hydrodynamics, Stencil, 3D FFT and SpMV) and different computers with various optimization techniques and it was seen that the range of OI spanned from 0.25 to just 1.64, with a median of 0.60. So an OI of 0.838 (hardware

prefetching enabled) achieved by the multiphase LBM–EBF kernel can be considered to an encouraging performance.

The roofline gives an upper bound of performance, and if the program is performing well below its roofline, then multiple *ceilings* can be added. These *ceilings* can guide which optimization process to be performed. One can not break through the ceiling without performing the associated optimization. In future, to improve the performance of LBM–EBF simulation, it is advised to consider kernel optimizations such as *memory affinity*, *long unit-stride accesses*, *sofware prefetching*, *unroll and reorder loops* and *"SIMD-ize" the code*.

The ridge point of the roofline, where the diagonal and horizontal roofs meet, offers an insight into the overall performance of the computer which can also be exploited to select a particular machine suitable for a given kernel. The x-coordinate of the ridge point is the minimum operational intensity required to achieve maximum performance. If the ridge point is far to the left, then almost any kernel can potentially hit the maximum performance. So the ridge point suggests the level of difficulty for programmers to achieve peak performance and conversely, for a particular kernel, an appropriate core architecture can be sought for, from which peak performance can be extracted without the need for greater optimizations.

In Appendix C, the profiling results of both single-phase and multiphase LBM–EBF kernels are shown. It is found that, for the single-phase kernel, the maximum flop/s is accrued by the function *lb_iteration_3d()*. This function performs the LB collision and streaming operations. The next floating point operations intensive function is *feq_3d()*, which calculates the equilibrium distribution function.

For the multiphase kernel, the first three floating point operations intensive functions in decreasing order are *fem_node_velocity()*, *ff_node_force()* and *lb_iteration_3d()*

(specifically speaking, the loop inside *lb_iteration_3d()* that wraps collision and streaming operations and adds external boundary force term to the LB equation) respectively. The function *fem_node_velocity()* calculates the fluid velocity at a solid boundary node by interpolating the velocities of the surrounding fluid nodes using the discrete dirac delta function, eqn. (16). The function *ff_node_force()* calculates the external boundary force term $\boldsymbol{g}(\boldsymbol{x}^e, t)$ on a fluid node by interpolating the fluid–solid interaction force, $\boldsymbol{F}^{fsi}$ of the surrounding solid boundary nodes.

Now from profiling for memory usage (results not listed in Appendix C for brevity), it is found that for the single-phase kernel, the maximum Gb/s is accrued by the function *lb_iteration_3d()*; whereas for multiphase LBM–EBF kernels, the functions *ff_node_force()*, *fem_node_velocity()*, *lb_iteration_3d()* and *feq_3d()* cause the most DRAM memory traffic, although no particular order can be determined since the traffic depends upon the particular combination of domain size and the number of fibers simulated. So to improve the performance of the code, these critical functions should be optimized in the foremost.

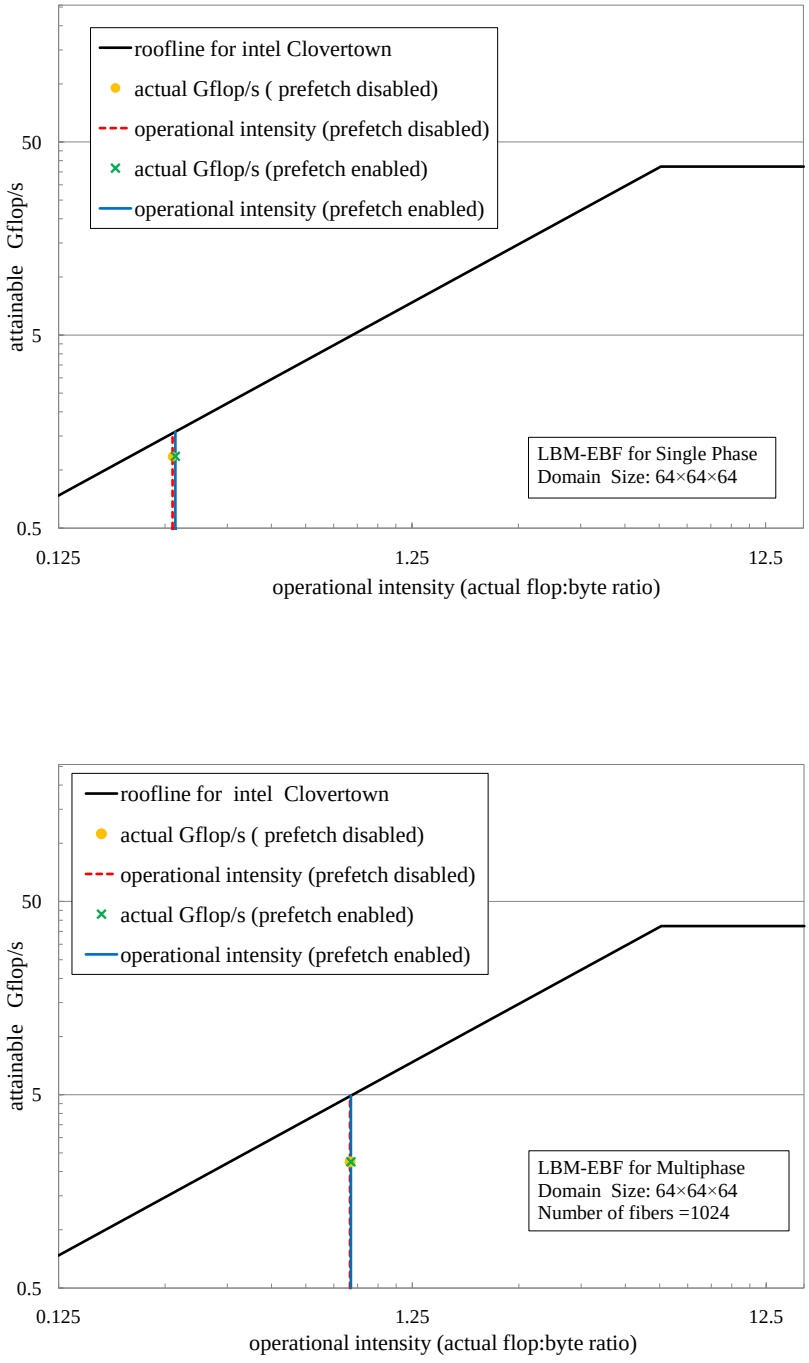

Figure 40: Actual LBM–EBF performance imposed over a roofline model for Intel Xeon E5345 Clovertown. (Top figure) Single phase performance when there is no fiber present. (Bottom figure) Multiphase performance with 1024 fibers. The prefetch refers to hardware prefetching.

APPENDIX A

PASSING DIFFUSION INFORMATION FROM 3D CARTESIAN TO 2D SURFACE SPHERICAL COORDINATE

Although diffusion is properly recognized as two-dimensional on the surface of a unit sphere, the orientation diffusivity tensor, $\mathbf{C}$, is a space tensor, expressed in global Cartesian spatial coordinates. Some method is needed to pass diffusion information between these two coordinate systems. For this purpose, $\mathbf{D}^r$ is defined as the projection of a three-dimensional space tensor, $\mathbf{C}$, onto the local surface coordinates of the unit sphere.

$$\mathbf{D}^r = \mathbf{t}^{\mathsf{T}} \cdot \mathbf{C} \cdot \mathbf{t} \tag{74}$$

where $\mathbf{t}$ is the projection tensor given by [10]:

$$\mathbf{t} = \begin{bmatrix} \cos\theta \sin\phi \;\; \hat{\mathbf{e}}_1\hat{\mathbf{e}}_\theta & -\cos\phi \;\; \hat{\mathbf{e}}_1\hat{\mathbf{e}}_\phi \\ \cos\theta \cos\phi \;\; \hat{\mathbf{e}}_2\hat{\mathbf{e}}_\theta & \sin\phi \;\; \hat{\mathbf{e}}_2\hat{\mathbf{e}}_\phi \\ -\sin\theta \;\; \hat{\mathbf{e}}_3\hat{\mathbf{e}}_\theta & 0 \;\; \hat{\mathbf{e}}_3\hat{\mathbf{e}}_\phi \end{bmatrix} \tag{75}$$

The tensor products are formed from the unit vectors of the spatial (1 is flow direction, x; 2 is gradient direction, y; 3 is vorticity direction, z; see figure 1) coordinate and surface coordinate (θ, ϕ) system. To keep the analysis compact, shorthand notations are introduced for the trigonometric functions of θ and ϕ:

$$M = \cos\theta \quad N = \sin\theta \quad C = \cos\theta \quad S = \sin\phi \tag{76}$$

Now with $\mathbf{t}$ given by eqn. (75) and $\mathbf{C}$ expanded component-by-component, eqn. (74) can be expressed as:

$$\mathbf{D}^r = \mathbf{t}^{\mathtt{T}} \cdot \begin{bmatrix} \mathsf{C}_{11}\,\hat{\mathbf{e}}_1\hat{\mathbf{e}}_1 & \mathsf{C}_{12}\,\hat{\mathbf{e}}_1\hat{\mathbf{e}}_2 & \mathsf{C}_{13}\,\hat{\mathbf{e}}_1\hat{\mathbf{e}}_3 \\ \mathsf{C}_{21}\,\hat{\mathbf{e}}_2\hat{\mathbf{e}}_1 & \mathsf{C}_{22}\,\hat{\mathbf{e}}_2\hat{\mathbf{e}}_2 & \mathsf{C}_{23}\,\hat{\mathbf{e}}_2\hat{\mathbf{e}}_3 \\ \mathsf{C}_{31}\,\hat{\mathbf{e}}_3\hat{\mathbf{e}}_1 & \mathsf{C}_{32}\,\hat{\mathbf{e}}_3\hat{\mathbf{e}}_2 & \mathsf{C}_{33}\,\hat{\mathbf{e}}_3\hat{\mathbf{e}}_3 \end{bmatrix} \cdot \mathbf{t}$$

$$= \mathbf{t}^{\mathtt{T}} \cdot \begin{bmatrix} (MS\mathsf{C}_{11} + MC\mathsf{C}_{12} - N\mathsf{C}_{13})\,\hat{\mathbf{e}}_1\hat{\mathbf{e}}_\theta & (-C\mathsf{C}_{11} + S\mathsf{C}_{12})\,\hat{\mathbf{e}}_1\hat{\mathbf{e}}_\phi \\ (MS\mathsf{C}_{21} + MC\mathsf{C}_{22} - N\mathsf{C}_{23})\,\hat{\mathbf{e}}_2\hat{\mathbf{e}}_\theta & (-C\mathsf{C}_{21} + S\mathsf{C}_{22})\,\hat{\mathbf{e}}_2\hat{\mathbf{e}}_\phi \\ (MS\mathsf{C}_{31} + MC\mathsf{C}_{32} - N\mathsf{C}_{33})\,\hat{\mathbf{e}}_3\hat{\mathbf{e}}_\theta & (-C\mathsf{C}_{31} + S\mathsf{C}_{32})\,\hat{\mathbf{e}}_3\hat{\mathbf{e}}_\phi \end{bmatrix}$$

$$= \begin{bmatrix} \begin{array}{c}(M^2S^2\mathsf{C}_{11} + M^2C^2\mathsf{C}_{22} \\ +N^2\mathsf{C}_{33} - 2MCN\mathsf{C}_{23}\end{array} & \begin{array}{c}(-MSC\mathsf{C}_{11} + MSC\mathsf{C}_{22} \\ -NS\mathsf{C}_{23} + NC\mathsf{C}_{31}\end{array} \\ -2MNS\mathsf{C}_{31} + 2M^2CS\mathsf{C}_{12})\,\hat{\mathbf{e}}_\theta\hat{\mathbf{e}}_\theta & +M(S^2 - C^2)\mathsf{C}_{12})\,\hat{\mathbf{e}}_\theta\hat{\mathbf{e}}_\phi \\ & \\ \begin{array}{c}(-MSC\mathsf{C}_{11} + MSC\mathsf{C}_{22} \\ -NS\mathsf{C}_{23} + NC\mathsf{C}_{31} \\ +M(S^2 - C^2)\mathsf{C}_{12})\,\hat{\mathbf{e}}_\phi\hat{\mathbf{e}}_\theta\end{array} & \begin{array}{c}(C^2\mathsf{C}_{11} + S^2\mathsf{C}_{22} \\ -2CS\mathsf{C}_{12})\,\hat{\mathbf{e}}_\phi\hat{\mathbf{e}}_\phi\end{array} \end{bmatrix} \tag{77}$$

In § 5.5.1, tables 2 – 4, the $\mathbf{C}$ was predicted. It is possible to project that $\mathbf{C}$ tensor into $\mathbf{D}^r$ by using eqn. (77) as derived here.

APPENDIX B

INTENSITY OF CONCENTRATION VARIATIONS

Lindström & Uesaka [72] proposed a measure for spatial correlation of fibers, defined by:

$$P_L = \frac{s_L^2\left(\tilde{n}L^3\right)}{nL^3} \tag{78}$$

Here, $s_L^2\left(\cdots\right)$ denotes the variance of a local quantity in many cubic volumes L^3 and $\tilde{n}$ is the local number concentration of fiber centroids,

$$\tilde{n} = \tilde{n}(\boldsymbol{x}) = \sum_j \delta\left(\boldsymbol{x} - \boldsymbol{c}_j\right) \tag{79}$$

where δ is the Dirac delta function, $\boldsymbol{c}_j$ is the centroid of fiber j, and the sum is taken over all fibers. Consequently, n is the average of $\tilde{n}$ in Ξ'. The measure P_L will be referred to as the intensity of concentration variations. Now from the property of a Poisson distribution, it is known that the variance of the distribution has the same value as the mean. Therefore, if the configuration is indeed random, we expect that $s^2(\tilde{n}L^3) = nL^3$. So with the definition of P_L, eqn. (78), $P_L = 1$ for randomly uniform fiber configurations in an infinite domain. At elevated concentration variations, $P_L > 1$, while $P_L < 1$ indicates that dispersive mechanisms are present. An analogy can be drawn between the definition of P_L and the formation number for two-dimensional fiber networks, which is defined as the ratio between the measured variance of local grammage and the variance expected for a randomly uniform network [35].

Now the steady-state intensity of concentration variations, $\bar{P}_L$, is plotted against nL^2d in figure 41. The $\bar{P}_L$ values from Lindström & Uesaka [72] correspond to a suspension of fibers where the fiber–fiber contacts are modeled to be frictionless (the friction coefficient is zero). In the LBM–EBF simulations, the contacts are always

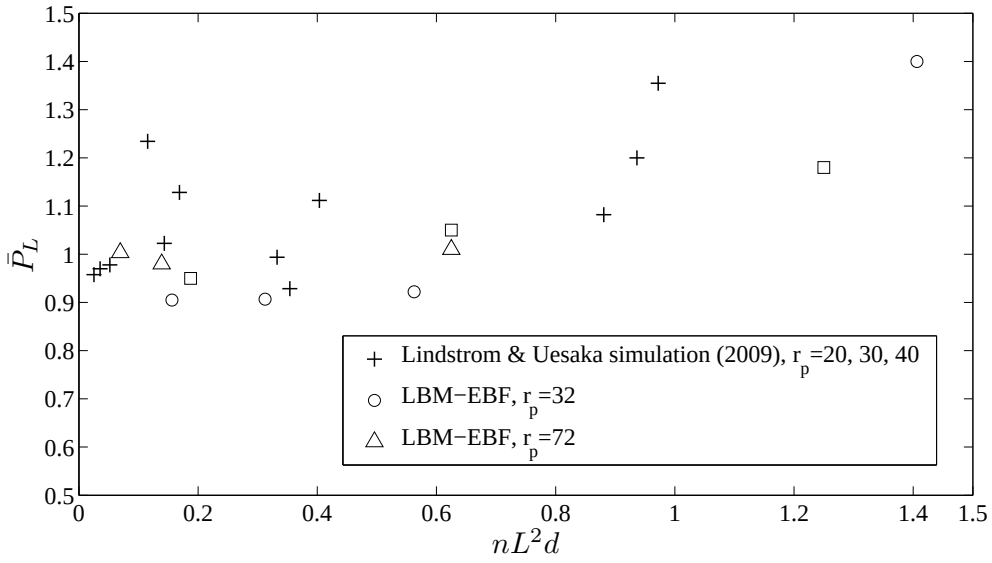

Figure 41: Average intensity of concentration variations, P_L, plotted as a function of nL^2d for different aspect-ratio fibers.

considered smooth, and the effect of friction was not studied. The observation from figure 41 is that for $nL^2d \lesssim 0.6$, the intensity of concentration variations, $\bar{P}_L \approx 1.0$. So a conclusion can be drawn that sheared suspensions of straight fibers maintain spatial homogeneity in most of the concentration range considered in this work.

APPENDIX C

PERFORMANCE PROFILING WITH PERFSUITE

Kernel: Single Phase LBM-EBF
Domain: 64x64x64 LBM unit
Summary for thread 0 (total of 4 threads have been used)

```
Version                     : 1.0
Generator                   : psprocess Java version 0.1

Execution Information
================================================================================
Collector                   : libpshwpc
Host                        : honest4.ncsa.uiuc.edu
Process ID                  : 27597
Thread                      : 0
User                        : gth823e
Command                     : ib3d

Profile Information
================================================================================
Class                       : PAPI
Version                     : 4.1.2.1
Event                       : PAPI_FP_OPS (Floating point operations)
Period                      : 1000000
Samples                     : 37019
Domain                      : user
Run Time (seconds)          : 230.03
Min Self %                  : (all)

Function Summary
--------------------------------------------------------------------------------
  Samples    Self %   Total %  Function

    21990    59.40%    59.40%  lbiteration_3d
    14611    39.47%    98.87%  feq_3d
      138     0.37%    99.24%  wall_3d_pbp
       86     0.23%    99.48%  inside_wall_read
        .
        .
        .
```

==========

Kernel: MultiPhase LBM-EBF

Domain: 64x64x64 LBM unit

No. of fibers=1024

Summary for thread 0 (total of 4 threads have been used)

```
Profile Information
================================================================================
Class                        : PAPI
Version                      : 4.1.2.1
Event                        : PAPI_FP_OPS (Floating point operations)
Period                       : 1000000
Samples                      : 183268
Domain                       : user
Run Time (seconds)           : 438.39
Min Self %                   : (all)

Function Summary
--------------------------------------------------------------------------------
  Samples    Self %   Total %  Function

    98321    53.65%    53.65%  fem_node_velocity
    46421    25.33%    78.98%  ff_node_force
    20755    11.32%    90.30%   L_lbiteration_3d_19__par_loop0_2.1451
    11233     6.13%    96.43%  feq_3d
     3471     1.89%    98.33%  inside_walls_pbp
     1978     1.08%    99.41%  interaction_3d
      227     0.12%    99.53%  pre_p_update
      198     0.11%    99.64%  inter_update_3d
      188     0.10%    99.74%  wall_3d_pbp
       99     0.05%    99.79%  inside_wall_read
       56     0.03%    99.82%  __libm_sse2_sincos
       53     0.03%    99.85%  _IO_flush_all_lockp
       49     0.03%    99.88%  __printf_fp
       37     0.02%    99.90%  L_mem_force_3d_169__par_loop3_2.467
        .
        .
        .
================================================================================
Formula to calculate Mflop/s from the above reports:
Mflop/s= (Samples x 1000000/run_time)x0.0000001
================================================================================

The .xml file used to generate the profile has the following content:

<?xml version="1.0" encoding="utf-8" ?>
 <ps_hwpc_profile class="PAPI">
    <ps_hwpc_event type="preset" name="PAPI_FP_OPS" threshold="1000000"/>
  </ps_hwpc_profile>
```

REFERENCES

[1] Advani, S. G. and Tucker III, C. L., "The use of tensors to describe and predict fiber orientation in short fiber composites," *Journal of Rheology*, vol. 31, no. 8, pp. 751 – 784, 1987.

[2] Advani, S. G. and Tucker III, C. L., "Closure approximations for three-dimensional structure tensors," *Journal of Rheology*, vol. 34, no. 3, pp. 367 – 386, 1990.

[3] Aidun, C. K. and Clausen, J. R., "Lattice-Boltzmann method for complex flows," *Annual Review of Fluid Mechanics*, vol. 42, no. 1, pp. 439 – 472, 2010.

[4] Aidun, C. K. and Lu, Y., "Lattice Boltzmann simulation of solid particles suspended in fluid," *Journal of Statistical Physics*, vol. 81, pp. 49 – 61, 1995.

[5] Aidun, C. K., Lu, Y., and Ding, E. J., "Direct analysis of particulate suspensions with inertia using the discrete Boltzmann equation," *Journal of Fluid Mechanics*, vol. 373, p. 287, 1998.

[6] Alder, B. J. and Wainwright, T. E., "Molecular dynamics by electronic computers," in *Transport Processes in Statistical Mechanics*, pp. 97 – 131, New York: Interscience, prigogin I ed., 1958.

[7] Altan, M. C., Advani, S. G., Güçeri, S. I., and Pipes, R. B., "On the description of the orientation state for fiber suspensions in homogeneous flows," *Journal of Rheology*, vol. 33, no. 7, pp. 1129 – 1155, 1989.

[8] Anczurowski, E. and Mason, S. G., "The kinetics of flowing dispersions: II. Equilibrium orientations of rods and discs (theoretical)," *Journal of Colloid and Interface Science*, vol. 23, no. 4, pp. 522 – 532, 1967.

[9] Anczurowski, E. and Mason, S. G., "The kinetics of flowing dispersions: III. Equilibrium orientations of rods and discs (experimental)," *Journal of Colloid and Interface Science*, vol. 23, no. 4, pp. 533 – 546, 1967.

[10] Aris, R., *Vectors, tensors, and the basic equations of fluid mechanics*. Prentice-Hall international series in the physical and chemical engineering sciences, Englewood Cliffs, N. J., 1962.

[11] Arlov, A. P., Forgacs, O. L., and Mason, S. G., "Particle motions in sheared suspensions IV. General behavior of wood pulp fibers," Svensk Papperstidn., vol. 61, no. 3, pp. 61 – 67, 1958.

[12] Batchelor, G. K., "The stress generated in a non-dilute suspension of elongated particles by pure straining motion," *Journal of Fluid Mechanics Digital Archive*, vol. 46, no. 04, pp. 813 – 829, 1971.

[13] Bay, R. S., *Fiber orientation in injection molded composites: A comparison of theory and experiment*. PhD thesis, University of Illinois Urbana-Champaign, 1991.

[14] Bay, R. S. and Tucker III, C. L., "Fiber orientation in simple injection moldings. part I: Theory and numerical methods," *Polymer Composites*, vol. 13, no. 04, pp. 317 – 331, 1992.

[15] Bay, R. S. and Tucker III, C. L., "Fiber orientation in simple injection moldings. part II: Experimental results," *Polymer Composites*, vol. 13, no. 04, pp. 332 – 341, 1992.

[16] Bhatnagar, P. L., Gross, E. P., and Krook, M., "A model for collision processes in gases. I. small amplitude processes in charged and neutral one-component systems," *Phys. Rev.*, vol. 94, pp. 511 – 525, May 1954.

[17] Bibbo, M. A., *Rheology of semi-concentrated fiber suspensions*. PhD thesis, Department of Chemical Engineering, Massachusetts Institute of Technology, 1987.

[18] Blakeney, W. R., "The viscosity of suspensions of straight, rigid rods," *Journal of Colloid and Interface Science*, vol. 22, pp. 324 – 330, 1966.

[19] Brady, J. F. and Bossis, G., "Stokesian dynamics," *Annual Review of Fluid Mechanics*, vol. 20, no. 1, pp. 111 – 157, 1988.

[20] Breedveld, V., *Shear-Induced Self-Diffusion in Concentrated Suspensions*. PhD thesis, University of Twente, Enschede, 2000.

[21] Bretherton, F. P., "The motion of rigid particles in a shear flow at low Reynolds number," *Journal of Fluid Mechanics*, vol. 14, pp. 284 – 304, 1962.

[22] Buick, J. M. and Greated, C. A., "Gravity in a lattice Boltzmann model," *Phys. Rev. E*, vol. 61, pp. 5307–5320, May 2000.

[23] Burgers, J. M., *In Second report on Viscosity and Plasticity*, ch. 3. *Kon. Ned. Akad. Wet. Verhand(Eerste Sectie)*, p. 113. No. 16, 1938.

[24] Carter, L. F., *A study of the rheology of suspensions of rod-shaped particles in a Navier-Stokes liquid*. PhD thesis, University of Michigan, 1967.

[25] Carter, L. and Goddard, J. D., "A rheological study of glass fibers in a newtonian fluid," Tech. Rep. N67-30073, NASA, May 1967.

[26] Chaouche, M. and Koch, D. L., "Rheology of non-brownian rigid fiber suspensions with adhesive contacts," *Journal of Rheology*, vol. 45, no. 2, pp. 369 – 382, 2001.

[27] Chen, S., Chen, H., Martnez, D., and Matthaeus, W., "Lattice boltzmann model for simulation of magnetohydrodynamics," *Phys. Rev. Lett.*, vol. 67, pp. 3776 – 3779, Dec 1991.

[28] Cheng, Y. and Li, J., "Introducing unsteady non-uniform source terms into the lattice boltzmann model," *International Journal for Numerical Methods in Fluids*, vol. 56, no. 6, pp. 629 – 641, 2008.

[29] Chung, D. H. and Kwon, T. H., "Fiber orientation in the processing of polymer composites," *Korea-Australia Rheology Journal*, vol. 14, pp. 175 – 188, 2002.

[30] Cintra Jr., J. S. and Tucker III, C. L., "Orthotropic closure approximations for flow-induced fiber orientation," *Journal of Rheology*, vol. 39, no. 6, pp. 1095 – 1122, 1995.

[31] Cox, R. G., "The motion of long slender bodies in a viscous fluid. part 2. shear flow," *Journal of Fluid Mechanics Digital Archive*, vol. 45, no. 04, pp. 625 – 657, 1971.

[32] Ding, E. J. and Aidun, C. K., "The dynamics and scaling law for particles suspended in shear flow with inertia," *Journal of Fluid Mechanics*, vol. 423, pp. 317 – 344, 2000.

[33] Ding, E. J. and Aidun, C. K., "Extension of the lattice-boltzmann method for direct simulation of suspended particles near contact," *Journal of Statistical Physics*, vol. 112, no. 3/4, pp. 685 – 708, 2003.

[34] Dinh, S. M. and Armstrong, R. C., "A rheological equation of state for semiconcentrated fiber suspensions," *Journal of Rheology*, vol. 28, no. 3, pp. 207 – 227, 1984.

[35] Dodson, C. T. J., "Fiber crowding, fiber contacts, and fiber flocculation," *Tappi Journal*, vol. 79, pp. 211 – 216, 1996.

[36] Doi, M. and Edwards, S. F., "Dynamics of rod-like macromolecules in concentrated solution. part 1," *J. Chem. Soc., Faraday Trans. 2*, vol. 74, pp. 560 – 570, 1978.

[37] Dupret, F. and Verleye, V., *Modelling the flow of fiber suspensions in narrow gaps*, pp. 1347 – 1398. in: Rheology Series, Elsevier, Amsterdam, 1999.

[38] Ericksen, J. L., "Anisotropic fluids," *Archive for Rational Mechanics and Analysis*, vol. 4, pp. 231 – 237, 1960.

[39] Evans, K. E. and Gibson, A. G., "Prediction of the maximum packing fraction achievable in randomly oriented short-fibre composites," *Composites Science and Technology*, vol. 25, no. 2, pp. 149 – 162, 1986.

[40] Fan, X.-J., Phan-Thien, N., and Zheng, R., "A direct simulation of fibre suspensions," *Journal of Non-Newtonian Fluid Mechanics*, vol. 74, no. 1-3, pp. 113 – 135, 1998.

[41] Feng, Z. and Michaelides, E., "The immersed boundary - lattice boltzmann method for solving fluid - particles interaction problems," *Journal of Computational Physics*, vol. 195, pp. 602 – 628, 2004.

[42] Flekkøy, E. G., "Lattice bhatnagar-gross-krook models for miscible fluids," *Phys. Rev. E*, vol. 47, pp. 4247 – 4257, Jun 1993.

[43] Folgar, F. and Tucker III, C. L., "Orientation Behavior of Fibers in Concentrated Suspensions," *Journal of Reinforced Plastics and Composites*, vol. 3, no. 2, pp. 98 – 119, 1984.

[44] Ginzbourg, I. and Adler, P. M., "Boundary flow condition analysis for the three-dimensional lattice boltzmann model," *J. Phys. II France*, vol. 4, pp. 191 – 214, February 1994.

[45] Goldstein, D., Handler, R., and Sirovich, L., "Modeling a no-slip flow boundary with an external force field," *Journal of Computational Physics*, vol. 105, no. 2, pp. 354 – 366, 1993.

[46] Goto, S., Nagazono, H., and Kato, H., "The flow behavior of fiber suspensions in newtonian fluids and polymer solutions," *Rheologica Acta*, vol. 25, pp. 119 – 129, 1986.

[47] Guo, Z., Zheng, C., and Shi, B., "Discrete lattice effects on the forcing term in the lattice boltzmann method," *Phys. Rev. E*, vol. 65, p. 046308, Apr 2002.

[48] Halliday, I., Hammond, L. A., Care, C. M., Good, K., and Stevens, A., "Lattice boltzmann equation hydrodynamics," *Phys. Rev. E*, vol. 64, p. 011208, Jun 2001.

[49] Hand, G. L., "A theory of dilute suspensions," *Archive for Rational Mechanics and Analysis*, vol. 7, pp. 81 – 86, 1961.

[50] He, X., Zou, Q., Luo, L.-S., and Dembo, M., "Analytic solutions of simple flows and analysis of nonslip boundary conditions for the lattice boltzmann bgk model," *Journal of Statistical Physics*, vol. 87, pp. 115–136, 1997. 10.1007/BF02181482.

[51] Hinch, E. J. and Leal, L. G., "The effect of brownian motion on the rheological properties of a suspension of non-spherical particles," *Journal of Fluid Mechanics Digital Archive*, vol. 52, no. 04, pp. 683 – 712, 1972.

[52] Hinch, E. J. and Leal, L. G., "Time-dependent shear flows of a suspension of particles with weak brownian rotations," *Journal of Fluid Mechanics Digital Archive*, vol. 57, no. 04, pp. 753 – 767, 1973.

[53] Hinch, E. J. and Leal, L. G., "Constitutive equations in suspension mechanics. part 2. approximate forms for a suspension of rigid particles affected by brownian rotations," *Journal of Fluid Mechanics Digital Archive*, vol. 76, no. 01, pp. 187 – 208, 1976.

[54] Hu, H. H., Joseph, D. D., and Crochet, M. J., "Direct simulation of fluid particle motions," *Theoretical and Computational Fluid Dynamics*, vol. 3, no. 5, pp. 285 – 306, 1992.

[55] Hyensjö, M., Dahlkild, A., Krochak, P., and Olson, J., "Shear influence on fibre orientation," *Nordic Pulp and Paper Research Journal*, vol. 22, pp. 376 – 382, 2007.

[56] Ivanov, Y. and van de Ven, T. G. M., "Damped oscillations in the viscosity of suspensions of rigid rods. II. bimodal and polydisperse suspensions," *Journal of Rheology*, vol. 26, pp. 231 – 244, 1982.

[57] Ivanov, Y., van de Ven, T. G. M., and Mason, S. G., "Damped oscillations in the viscosity of suspensions of rigid rods. I. monomodal suspensions," *Journal of Rheology*, vol. 26, pp. 213 – 230, 1982.

[58] Jack, D. A. and Smith, D. E., "An invariant based fitted closure of the sixth-order orientation tensor for modeling short-fiber suspensions," *Journal of Rheology*, vol. 49, no. 5, pp. 1091 – 1115, 2005.

[59] Jeffery, G. B., "The motion of ellipsoidal particles immersed in a viscous fluid," *Proceedings of the Royal Society of London. Series A, Containing Papers of a Mathematical and Physical Character*, vol. 102, no. 715, pp. 161 – 179, 1922.

[60] Joung, C. G., Phan-Thien, N., and Fan, X.-J., "Direct simulation of flexible fibers," *Journal of Non-Newtonian Fluid Mechanics*, vol. 99, no. 1, pp. 1 – 36, 2001.

[61] Keshtkar, M., Heuzey, M. C., and Carreau, P. J., "Rheological behavior of fiber-filled model suspensions: Effect of fiber flexibility," *Journal of Rheology*, vol. 53, no. 3, pp. 631 – 650, 2009.

[62] Kim, S. and Karrila, S. J., *Microhydrodynamics: Principles and Selected Applications*. Butterworth-Heinemann, Boston, 1991.

[63] Kitano, T. and Kataoka, T., "The rheology of suspensions of vinylon fibers in polymer liquids. I. suspensions in silicone oil," *Rheologica Acta*, vol. 20, no. 4, pp. 390 – 402, 1981.

[64] Koch, D. L., "On hydrodynamic diffusion and drift in sheared suspensions," *Physics of Fluids A: Fluid Dynamics*, vol. 1, no. 10, pp. 1742 – 1745, 1989.

[65] Koch, D. L., "A model for orientational diffusion in fiber suspensions," *Physics of Fluids*, vol. 7, no. 8, pp. 2086 – 2088, 1995.

[66] Krochak, P. J., Olson, J. A., and Martinez, D. M., "The orientation of semidilute rigid fiber suspensions in a linearly contracting channel," *Physics of Fluids*, vol. 20, no. 7, p. 073303, 2008.

[67] Ladd, A. J. C., "Numerical simulations of particulate suspensions via a discretized boltzmann equation. Part 1. Theoretical foundation," *Journal of Fluid Mechanics*, vol. 271, pp. 285 – 309, 1994.

[68] Ladd, A. J. C., "Numerical simulations of particulate suspensions via a discretized boltzmann equation. Part 2. Numerical results," *Journal of Fluid Mechanics*, vol. 271, pp. 311 – 339, 1994.

[69] Ladd, A. J. C. and Verberg, R., "Lattice-Boltzmann simulations of particle-fluid suspensions," *Journal of Statistical Physics*, vol. 104, pp. 1191 – 1251, 2001.

[70] Leal, L. G. and Hinch, E. J., "The effect of weak brownian rotations on particles in shear flow," *Journal of Fluid Mechanics Digital Archive*, vol. 46, no. 04, pp. 685 – 703, 1971.

[71] Lindström, S. B. and Uesaka, T., "Simulation of semidilute suspensions of non-brownian fibers in shear flow.," *Journal of Chemical Physics*, vol. 128, no. 2, pp. 024901–1 – 024901–14, 2008.

[72] Lindström, S. B. and Uesaka, T., "A numerical investigation of the rheology of sheared fiber suspensions," *Physics of Fluids*, vol. 21, no. 8, p. 083301, 2009.

[73] Lipscomb, G. G., *Analysis of suspension rheology in complex flows.* PhD thesis, University of California, Berkeley, 1987.

[74] Loewen, S. R., "Fibre orientation optimization," *Pulp and Paper Canada*, vol. 19, pp. 25 – 27, 1997.

[75] Luo, L.-S., "Unified theory of lattice boltzmann models for nonideal gases," *Phys. Rev. Lett.*, vol. 81, pp. 1618 – 1621, Aug 1998.

[76] Mackaplow, M. B. and Shaqfeh, E. S. G., "A numerical study of the rheological properties of suspensions of rigid, non-brownian fibres," *Journal of Fluid Mechanics Digital Archive*, vol. 329, no. -1, pp. 155 – 186, 1996.

[77] MacMeccan, R. M., Clausen, J. R., Neitzel, G. P., and Aidun, C. K., "Simulating deformable particle suspensions using a coupled lattice-Boltzmann and finite-element method," *Journal of Fluid Mechanics*, vol. 618, pp. 13 – 39, 2009.

[78] Martys, N. S., Shan, X., and Chen, H., "Evaluation of the external force term in the discrete boltzmann equation," *Phys. Rev. E*, vol. 58, pp. 6855 – 6857, Nov 1998.

[79] Mewis, J. and Metzner, A. B., "The rheological properties of suspensions of fibres in newtonian fluids subjected to extensional deformations," *Journal of Fluid Mechanics*, vol. 62, no. 03, pp. 593 – 600, 1974.

[80] Montgomery-Smith, S., Jack, D. A., and Smith, D. E., "A systematic approach to obtaining numerical solutions of Jeffery's type equations using spherical harmonics," *Composites Part A: Applied Science and Manufacturing*, vol. 41, no. 7, pp. 827 – 835, 2010.

[81] Moré, J. J., *Numerical Analysis*, ch. The Levenberg-Marquardt Algorithm: Implementation and Theory, pp. 105 – 116. No. 630 in Lecture Notes in Mathematics, Springer Verlag, 1977.

[82] Nawab, M. A. and Mason, S. G., "Viscosity of dilute suspensions of thread-like particles," *The Journal of Physical Chemistry*, vol. 62, no. 10, pp. 1248 – 1253, 1958.

[83] Okagawa, A., Cox, R. G., and Mason, S. G., "The kinetics of flowing dispersions. VI. transient orientation and rheological phenomena of rods and discs in shear flow," *Journal of Colloid and Interface Science*, vol. 45, no. 2, pp. 303 – 329, 1973.

[84] Olson, J. A., Frigaard, I., Chan, C., and Hämäläinen, J. P., "Modeling a turbulent fibre suspension flowing in a planar contraction: The one-dimensional headbox," *International Journal of Multiphase Flow*, vol. 30, no. 1, pp. 51 – 66, 2004.

[85] Parsheh, M., Brown, M. L., and Aidun, C. K., "On the orientation of stiff fibres suspended in turbulent flow in a planar contraction," *Journal of Fluid Mechanics*, vol. 545, p. 245 269, 2005.

[86] Peskin, C. S., "Numerical analysis of blood flow in the heart," *Journal of computational physics*, vol. 25, pp. 220 – 252, 1977.

[87] Peskin, C. S., "The immersed boundary method," *Acta Numerica*, vol. 11, pp. 479 – 517, 2002.

[88] Petrich, M. P., Koch, D. L., and Cohen, C., "An experimental determination of the stress-microstructure relationship in semi-concentrated fiber suspensions," *Journal of Non-Newtonian Fluid Mechanics*, vol. 95, no. 2-3, pp. 101 – 133, 2000.

[89] Phan-Thien, N., Fan, X.-J., Tanner, R. I., and Zheng, R., "Folgar-Tucker constant for a fibre suspension in a newtonian fluid," *Journal of Non-Newtonian Fluid Mechanics*, vol. 103, no. 2-3, pp. 251 – 260, 2002.

[90] Phan-Thien, N. and Kim, S., *Microstructure in elastic media: Principles and Computational Methods*. Oxford University Press, New York, 1994.

[91] Phelps, J. H., *Processing microstructure models for short- and long-fiber thermoplastic composites*. PhD thesis, Mechanical Engineering, University of Illinois at Urbana-Champaign, 2009.

[92] Phelps, J. H. and Tucker III, C. L., "An anisotropic rotary diffusion model for fiber orientation in short- and long-fiber thermoplastics," *Journal of Non-Newtonian Fluid Mechanics*, vol. 156, no. 3, pp. 165 – 176, 2009.

[93] Premnath, K. N., Pattison, M. J., and Banerjee, S., "Steady state convergence acceleration of the generalized lattice boltzmann equation with forcing term through preconditioning," *Journal of Computational Physics*, vol. 228, no. 3, pp. 746 – 769, 2009.

[94] Qi, D., "Lattice-Boltzmann simulations of particles in non-zero-Reynolds-number flows," *Journal of Fluid Mechanics*, vol. 385, pp. 41 – 62, 1999.

[95] Qian, Y. H., d'Humieres, D., and Lallemand, P., "Lattice BGK models for Navier-Stokes equations," *Europhysics Letters*, vol. 17, no. 6, pp. 479 – 484, 1992.

[96] Rahnama, M., Koch, D. L., Iso, Y., and Cohen, C., "Hydrodynamic, translational diffusion in fiber suspensions subject to simple shear flow," *Physics of Fluids A: Fluid Dynamics*, vol. 5, no. 4, pp. 849 – 862, 1993.

[97] Rahnama, M., Koch, D. L., and Shaqfeh, E. S. G., "The effect of hydrodynamic interactions on the orientation distribution in a fiber suspension subject to simple shear flow," *Physics of Fluids*, vol. 7, no. 3, pp. 487 – 506, 1995.

[98] Ranganathan, S. and Advani, S. G., "Fiber–fiber interactions in homogeneous flows of nondilute suspensions," *Journal of Rheology*, vol. 35, no. 8, pp. 1499 – 1522, 1991.

[99] Ross, R. F. and Klingenberg, D. J., "Dynamic simulation of flexible fibers composed of linked rigid bodies," *Journal of Chemical Physics*, vol. 6, no. 7, pp. 2949 – 2960, 1997.

[100] Salahuddin, A., Wu, J., and Aidun, C. K., "Analyses of rotational diffusion of rigid fibers and orientation effect on rheology of flexible fibers in shear flow with direct numerical simulation," in *ICMF-2010: Proceedings of the International Conference on Multiphase Flow*, (Tampa, FL), 2010.

[101] Sbragaglia, M., Benzi, R., Biferale, L., Chen, H., Shan, X., and Succi, S., "Lattice boltzmann method with self-consistent thermo-hydrodynamic equilibria," *Journal of Fluid Mechanics*, vol. 628, pp. 299 – 309, 2009.

[102] Sepehr, M., Carreau, P. J., Moan, M., and Ausias, G., "Rheological properties of short fiber model suspensions," *Journal of Rheology*, vol. 48, no. 5, pp. 1023 – 1048, 2004.

[103] Shan, X. and Chen, H., "Lattice boltzmann model for simulating flows with multiple phases and components," *Phys. Rev. E*, vol. 47, pp. 1815 – 1819, Mar 1993.

[104] Shaqfeh, E. S. G. and Fredrickson, G. H., "The hydrodynamic stress in a suspension of rods," *Physics of Fluids A: Fluid Dynamics*, vol. 2, no. 1, pp. 7–24, 1990.

[105] Shaqfeh, E. S. G. and Koch, D. L., "The effect of hydrodynamic interactions on the orientation of axisymmetric particles flowing through a fixed bed of spheres or fibers," *Physics of Fluids*, vol. 31, no. 4, pp. 728 – 744, 1988.

[106] Shaqfeh, E. S. G. and Koch, D. L., "Orientational dispersion of fibers in extensional flows," *Physics of Fluids A: Fluid Dynamics*, vol. 2, no. 7, pp. 1077 – 1094, 1990.

[107] Sierou, A. and Brady, J. F., "Accelerated stokesian dynamics simulations," *Journal of Fluid Mechanics*, vol. 448, no. -1, pp. 115 – 146, 2001.

[108] Sierou, A. and Brady, J. F., "Shear-induced self-diffusion in non-colloidal suspensions," *Journal of Fluid Mechanics*, vol. 506, no. -1, pp. 285 – 314, 2004.

[109] Silva, G. and Semiao, V., "A study on the inclusion of body forces in the lattice Boltzmann BGK equation to recover steady-state hydrodynamics," *Physica A: Statistical Mechanics and its Applications*, vol. 390, no. 6, pp. 1085 – 1095, 2011.

[110] Skjetne, P., Ross, R. F., and Klingenberg, D. J., "Simulation of single fiber dynamics," *Journal of Chemical Physics*, vol. 107, no. 6, pp. 2108 – 2121, 1997.

[111] Smook, G., *Handbook for pulp and paper technologists*. Angus Wilde Publications, Vancouver, 1992.

[112] Stickel, J. J. and Powell, R. L., "Fluid mechanics and rheology of dense suspensions," *Annual Review of Fluid Mechanics*, vol. 37, no. 1, pp. 129 – 149, 2005.

[113] Stover, C. A., *The dynamics of fibers suspended in shear flow*. PhD thesis, School of Chemical Engineering, Cornell University, 1991.

[114] Stover, C. A. and Cohen, C., "The motion of rodlike particles in the pressure-driven flow between two flat plates," *Rheologica Acta*, vol. 29, pp. 192 – 203, 1990. 10.1007/BF01331355.

[115] Stover, C. A., Koch, D. L., and Cohen, C., "Observations of fibre orientation in simple shear flow of semi-dilute suspensions," *Journal of Fluid Mechanics Digital Archive*, vol. 238, pp. 277 – 296, 1992.

[116] Succi, S., *The Lattice Boltzmann equation for fluid dynamics and Beyond*. Oxford University Press, New York, 2001.

[117] Sundararajakumar, R. R. and Koch, D. L., "Structure and properties of sheared fiber suspensions with mechanical contacts," *Journal of Non-Newtonian Fluid Mechanics*, vol. 73, no. 3, pp. 205 – 239, 1997.

[118] Swift, M. R., Orlandini, E., Osborn, W. R., and Yeomans, J. M., "Lattice boltzmann simulations of liquid-gas and binary fluid systems," *Phys. Rev. E*, vol. 54, pp. 5041 – 5052, Nov 1996.

[119] Switzer III, L. H. and Klingenberg, D. J., "Rheology of sheared flexible fiber suspensions via fiber-level simulations," *Journal of Rheology*, vol. 47, no. 3, pp. 759 – 778, 2003.

[120] Thomasset, J., Carreau, P. J., Sanschagrin, B., and Ausias, G., "Rheological properties of long glass fiber filled polypropylene," *Journal of Non-Newtonian Fluid Mechanics*, vol. 125, no. 1, pp. 25 – 34, 2005.

[121] Tucker III, C. L. and Advani, S. G., *Processing of Short-fiber systems*, vol. 10 of *Composite Materials Series*. Elsevier, Amsterdam, 1994.

[122] Ullmar, M., *On fibre alignment mechanisms in a headbox nozzle*. Licentiate thesis, Royal Institute of Technology (KTH), Stockholm, Sweden, 1998.

[123] Ullmar, M. and Norman, B., "Observation of fibre orientation in a headbox nozzle at low consistency," in *TAPPI Proceedings, Engineering and Papermaking Conference*, p. 685, 1997.

[124] Williams, S., Watterman, A., and Patterson., D., "Roofline: An insightful visual performance model for floating-point programs and multicore architectures," *Communications of the ACM*, April 2009.

[125] Wolffe, G., Oleszkiewicz, J., Cherba, D., and Qi, D., "Parallelizing solid particles in lattice boltzmann fluid dynamics," in *International Conference on Parallel and Distributed Processing Techniques and Applications*, (Las Vegas), 2002.

[126] Wu, J. and Aidun, C. K., "A method for direct simulation of flexible fiber suspensions using lattice-Boltzmann equation with external boundary force," *International Journal of Multiphase Flow*, vol. 36, pp. 202 – 209, 2010.

[127] WU, J. and AIDUN, C. K., "A numerical study of the effect of fibre stiffness on the rheology of sheared flexible fibre suspensions," *Journal of Fluid Mechanics*, vol. 662, pp. 123 – 133, 2010.

[128] Wu, J. and Aidun, C. K., "Simulating 3D deformable particle suspensions using lattice Boltzmann method with discrete external boundary force," *International Journal for Numerical Methods in Fluids*, vol. 62, pp. 765 – 783, 2010.

[129] Yamamoto, S. and Matsuoka, T., "A method for dynamic simulation of rigid and flexible fibers in a flow field," *Journal of Chemical Physics*, vol. 98, pp. 644 – 650, 1993.

[130] Yamane, Y., Kaneda, Y., and Dio, M., "Numerical simulation of semi-dilute suspensions of rodlike particles in shear flow," *Journal of Non-Newtonian Fluid Mechanics*, vol. 54, pp. 405 – 421, 1994.

[131] Yasuda, K., Mori, N., and Nakamura, K., "A new visualization technique for short fibers in a slit flow of fiber suspensions," *International Journal of Engineering Science*, vol. 40, no. 9, pp. 1037 – 1052, 2002.

[132] Yudistiawan, W. P., Ansumali, S., and Karlin, I. V., "Hydrodynamics beyond Navier-Stokes: The slip flow model," *Phys. Rev. E*, vol. 78, p. 016705, Jul 2008.

[133] Zhang, X., "Fiber orientation in headbox," Master's thesis, University of British Columbia Vancouver, Canada, 2001.

[134] Zhou, J. G., "Axisymmetric lattice boltzmann method," *Phys. Rev. E*, vol. 78, p. 036701, Sep 2008.

[135] Zirnsak, M., Hur, D., and Boger, D., "Normal stresses in fibre suspensions," *Journal of Non-Newtonian Fluid Mechanics*, vol. 54, pp. 153 – 193, 1994.

[136] Zuzovsky, M., Priel, Z., and Mason, S. G., "Memory impairment in flowing suspensions. III. brownian rotation of spheroids," *Journal of Colloid and Interface Science*, vol. 75, no. 1, pp. 230 – 239, 1980.

VITA

ASIF SALAHUDDIN

A native of Bangladesh, Asif Salahuddin was born on August 24th 1978, in providence of Rajshahi, well known for the river Padma – that flows through it – originating as the river Ganges from the Himalayas. He attended Bangladesh University of Engineering and Technology (BUET) and was awarded the B.Sc (Mechanical Engineering) degree in April 2002. As a senior year student at BUET, Asif was introduced to ways of research in computational simulations in engineering by Dr. S. Reaz Ahmed, his B.Sc thesis supervisor. In less than a year after his graduation, Asif landed in USA, and a Greyhound bus dropped him beside a Palmetto tree in South Carolina, Columbia. At USC, Columbia, Asif conducted research in computational nuclear thermal hydraulics (in a project for Westinghouse Electric Co.) under the supervision of Prof. Jamil Khan, and received his MS degree in mechanical engineering in August 2005. In one afternoon after graduation, a yellow jacket buzzing near his window, presaged Asif's good luck – as shortly afterwards he found himself been awarded a PSE fellowship to pursue a PhD degree at Georgia Institute of Technology. There he worked in Prof. Cyrus Aidun's lattice–Boltzmann research group, conducting research in fiber–level simulation to analyze fluid flow with suspension. From 2007–2009, Asif served as the president of the Graduate Student Chapter of TAPPI (Tech. Assoc. Pulp and Paper Ind.) at Georgia Tech. In August 2011, he completed the PhD degree – only to start collecting pebbles once again from the sea shore.